Correlative live and fixed cell superresolution microscopy

DISSERTATION ZUR ERLANGUNG DES
NATURWISSENSCHAFTLICHEN DOKTORGRADES DER
JULIUS-MAXIMILIANS-UNIVERSITÄT WÜRZBURG

vorgelegt von

Andreas Kurz

geboren in Würzburg

Würzburg, Oktober 2019

Eingereicht am: ....

Mitglieder der Promotionskommission:

Vorsitzender: ....

Gutachter: Prof. Dr. Markus Sauer

Gutachter: Prof. Dr. Roy Gross

Gutachter: PD Dr. Sören Doose

Tag des Promotionskolloquiums: ....

Doktorurkunde ausgehändigt am: ....

Abstract

Over the last decade life sciences have made an enormous leap forward. The development of complex analytical instruments, in particular in fluorescence microscopy, has played a decisive role in this. Scientist can now rely on a wide range of imaging techniques that offer different advantages in terms of optical resolution, recording speed or living cell compatibility. With the help of these modern microscopy techniques, multi-protein complexes can be resolved, membrane receptors can be counted, cellular pathways analysed or the internalisation of receptors can be tracked. However, there is currently no universal technique for comprehensive experiment execution that includes dynamic process capture and super resolution imaging on the same target object. In this work, I built a microscope that combines two complementary imaging techniques and enables correlative experiments in living and fixed cells. With an image scanning based laser spot confocal microscope, fast dynamics in several colors with low photodamage of the cells can be recorded. This novel system also has an improved resolution of 170 nm and was thoroughly characterized in this work. The complementary technique is based on single molecule localization microscopy, which can achieve a structural resolution down to 20-30 nm. Furthermore I implemented a microfluidic pump that allows direct interaction with the sample placed on the microscope. Numerous processes such as living cell staining, living cell fixation, immunostaining and buffer exchange can be observed and performed directly on the same cell. Thus, dynamic processes of a cell can be frozen and the structures of interest can be stained and analysed with high-resolution microscopy. Furthermore, I have equipped the detection path of the single molecule technique with an adaptive optical element. With the help of a deformable mirror, imaging functions can be shaped and information on the 3D position of the individual molecules can be extracted.

Zusammenfassung

Im letzten Jahrzehnt hat der Bereich der Lebenswissenschaften einen enormen Sprung nach vorne gemacht. Maßgeblich dafür waren die Entwicklung von komplexen Analysegeräten insbesondere in der Fluoreszenz Mikroskopie. Die Anwender können nun auf eine Vielzahl von Bildgebungstechniken zurückgreifen die unterschiedliche Vorzüge hinsichtlich optischer Auflösung, Aufnahmegeschwindigkeit oder Lebend Zell Kompatibilität bieten. Mithilfe dieser modernen Mikroskopietechniken lassen sich beispielsweise Multiproteinkomplexe auflösen, Membranrezeptoren zählen, zelluläre Signalwege analysieren oder die Internalisierung von Rezeptoren verfolgen. Für eine umfassende Experimentdurchführung, die Erfassung dynamischer Prozesse sowie superhochauflösende Bildgebung an ein und demselben Zielobjekt beinhalten, gibt es derzeit keine einheitliche Technik. In dieser Arbeit habe ich ein Mikroskop aufgebaut, das zwei komplementäre Bildgebungstechniken vereint und korrelative Experimente von lebend zu fixierten Zellen ermöglicht. Mit einem Image Scanning basierten Konfokal Mikroskop können schnelle Dynamiken in mehreren Farben mit geringer Photoschädigung der Zellen aufgenommen werden. Dieses neuartige System weist zudem eine Auflösungsverbesserung von 170 nm auf und wurde im Rahmen der Arbeit ausführlich charakterisiert. Die komplementäre Technik basiert auf der Einzel-Molekül Lokalisations Mikroskopie, mit der sich eine strukturelle Auflösung von bis zu 20 nm erreichen lässt. Desweiteren habe ich eine Mikrofluidpumpe implementiert, die eine direkte Interaktion mit der auf dem Mikroskop platzierten Probe erlaubt. Zahlreiche Prozesse wie Lebend-Zell Färbung, Lebend-Zell Fixierung, Immuno-Färbung und Puffertausch können damit direkt an der gleichen Zelle beobachtet und durchgeführt werden. So können dynamische Prozesse einer Zelle sozusagen eingefroren werden und die Strukturen von Interesse gefärbt und mit höchstauflösender Mikroskopie analysiert werden. Desweiteren habe ich den Detektionspfad der Einzel-Molekül Technik mit einem adaptiven optischen Element ausgestattet. Mithilfe eines deformierbaren Spiegels lässt sich so Abbildungsfunktion formen und Information zur 3D Position der einzelnen Moleküle gewinnen.

Table of contents

Chapter 1

Theory

In order to understand the special features of the microscope setup established within the scope of this work, a comprehensive knowledge of fluorescence, optics and microscopy techniques is required. The following chapters therefore deal with the phenomenon of fluorescence as well as detection with optical elements. The basics of image formation by geometric derivation as well as an introduction to wave and Fourier optics are discussed. With this knowledge the application in various microscopy techniques as well as three dimensional decoding of single molecules will be illustrated.

Although nowadays numerous outstanding literature exist dealing with the topics of fundamentals in fluorescence I want to add a brief introduction to cover all aspects required for this thesis. The most comprehensive literature in this field might be *Principles of fluorescence spectroscopy* by Joseph Lakowicz [Lak06].

1.1 Fluorescence

In our daily life the phenomenon called *fluorescence* is quite unnoticeable. We are used to light generated by electricity or in some rare cases by chemical reactions. Fluorescence itself is a light induced emission. A fluorescent probe is undergoing at minimum a two-step process resulting in the emission of light as shown in figure 1.1. The fluorescent probe is in its non-fluorescent ground state S_0. In the first step the photon energy E_v of the illumination is absorbed by the probe populating the first excited energy level S_1 or higher. The minimal required energy is the energy difference between these two energy levels $\Delta E = S_1 - S_0$. The radiative emission originates only from the transition of the first excited state S_1 to the ground state S_0 or vibrational energy levels energetically located above and is defined as *fluorescence*.

The broadening of excitation and emission spectra originates from the additional transitions including vibrational states and is illustrated in figure 1.2.

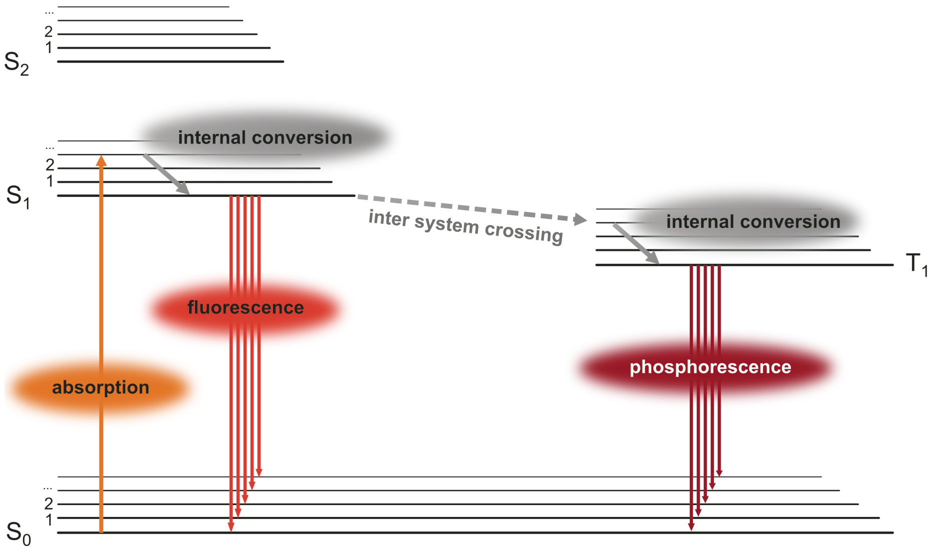

Fig. 1.1 Jablonksy diagram depicting energy levels and transitions relevant for light emitting processes. Energy levels with antiparallel spins are termed singlet state S with sublevels. Absorption occurs from ground state S_0 to excited state S_1 or higher, fluorescence occurs by relaxation from S_1 to ground state and higher vibrational energy levels. Intersystem crossing populates triplet states with parallel spin orientation. Relaxation from T_1 to ground state is termed phosphorescence. Non-radiative relaxation is termed internal conversion.

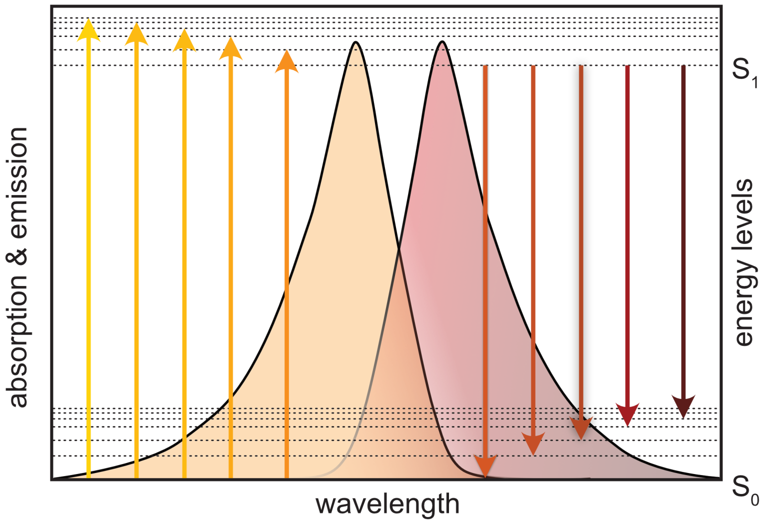

Fig. 1.2 Stokes-Shift of absorption to emission spectrum caused by transitions between ground state energy levels and multiple vibrational energy levels.

The lifetime of the excited S_1 state lies in the range of several nanoseconds for synthetic fluorophores and fluorescent proteins. Populated vibrational energy levels undergo a non radiative relaxation to the first excited state S_1, termed *internal conversion* in the schematic. The energy of the emitted photon is lower than the excited photon, causing a (red-)shift of the emitted wavelength. This effect is known as *Stokes-shift* and ultimately enables the separation of excitation and emission with coated filters and proper spectral transmission and reflection properties.

Furthermore a non-radiative intersystem crossing from excited S_1 state to first triplet state T_1 can occur including a spin conversion. The quantum mechanically unlikely transition from the populated triplet state T_1 to the ground state S_0 is radiative and termed *phosphorescence*. The low likelihood of this process explains triplet lifetimes several orders of magnitude higher than in the fluorescent transition [Lak06].

1.2 Fluorescence and Microscopy

The implementation of fluorescence as a specific and quantifiable marker has contributed significantly to the development of fluorescence microscopy with the development of synthetic fluorophores and the discovery of the green fluorescent protein (GFP) by Roger Tsien. By genetic manipulation specific positions in cellular structures could be marked and mapped. The spectral extension of the fluorescent proteins, as well as the development of synthetic dyes which were bound by means of antibodies to their target structure opened unprecedented possibilities for the life sciences. The development of technical components such as cameras, lasers and optics contributed significantly to the fact that microscopy has become an irreplaceable tool of today's biological research. In the following sections, the necessary optical basics will be explained and important relations will be illustrated. These elementary concepts are the foundation for a comprehensive understanding of the beauty of microscopy.

1.3 Image formation

Even in ancient times, simple aids made of glass or crystal fragments were used to collect and depict light. The first systematic approaches for a biconvex collecting lens came from Persia in the 7th century BC and the refractive law known today as Snellius' Law can also be found in the reconstructed treatise [Ros90]. Almost 2000 years later, the converging lens is still the most basic component of any optical system. Geometric optics can be used to derive the basic laws of lenses by simple geometric calculations of ray angles and lengths.

Geometric optics can be used for this purpose, since the objects under consideration are much larger than the wavelengths in the visible range of the spectrum.
First the derivation of the lens maker equation will be demonstrated starting with a single surface sphere to introduce the theory of first order and then add a second surface to form a standard biconvex lens. The lens maker equation will follow as well as Snell's law.

1.3.1 Basic Optics

Fermat's Principle

A light ray traveling through two media with different refractive indices is deviated from its original direction of travel as depicted in figure 1.3.

> "The actual path traveled by light in going from one point to another is that which, under the given conditions, requires the least time." [FH03]

The time from point A (t_0) to B (t_1) is covered in travel time T with the speed of light . The refractive index

$$n = \frac{c}{v} \tag{1.1}$$

describes the ratio of speed of light being faster than light in a medium with given refractive index n .
The optical path length OPL from point A to B can be expressed via the relation

$$OPL = cT = \int_A^B n(s)ds \tag{1.2}$$

and the minimal optical path length can be found using the derivative

$$\delta OPL = \delta \int_A^B n(s)ds = 0. \tag{1.3}$$

The optical wavelength can therefore be estimated as an extreme between point A an B, by multiplication of the physical length with the refractive index [MMS08].

$$OPL = \overline{AO} \cdot n_1 + \overline{OB} \cdot n_2. \tag{1.4}$$

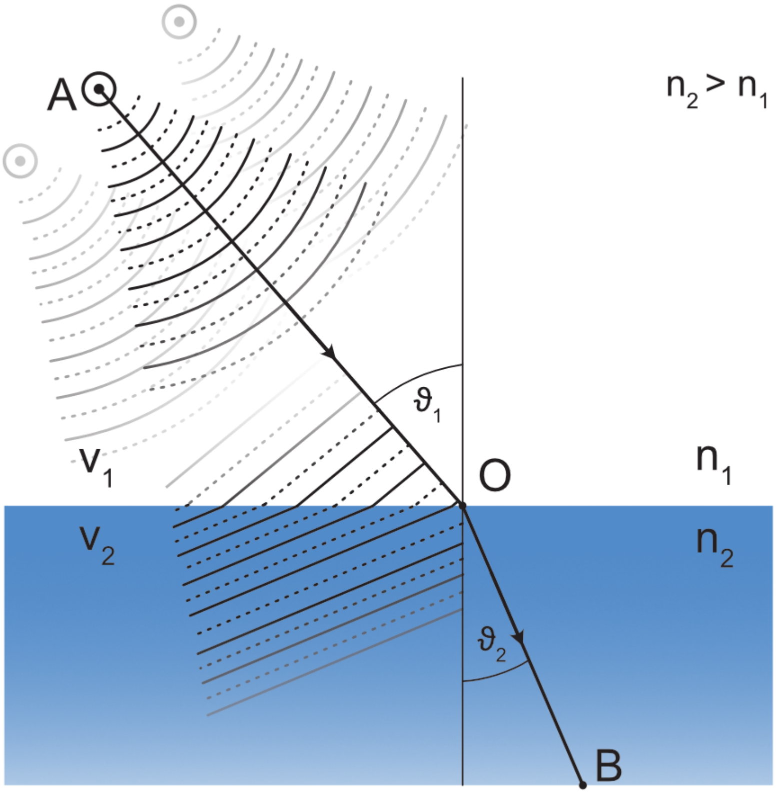

Fig. 1.3 The three basic optic principles: 1) Huygens principle: spherical waves from point sources like in A form in sum a wavefront with distinct propagation direction. 2) Fermat's principle: light traveling from point A to B will take the path of least time 3) Snell's law: Deviation of a light ray traveling through media with different refractive indices (n_1, n_2) correlates with the ratios of velocities v, refractive indices n and $\sin\vartheta$ to the incident normal of both media.

Snell's Law

The amount of refraction from a ray traveling through two media with different but isotropic refractive index is a logical conclusion of *Fermat's* principle of least time [FH03].

Snell's Law states that the amount of refracted to incident ray described in the deviation of angle θ to the normal of the incident surface corresponds to the refractive indices of the media such as

$$n_1 \cdot \sin\theta_1 = n_2 \cdot \sin\theta_2. \tag{1.5}$$

With increasing incident angle the refracted ray deviates as well. Reaching a specific angle no *refracted* ray is visible but a total *reflected* ray appears. According to (1.5) the equation changes to

$$n_1 \cdot sin\theta_1 = n_2 \cdot \sin 90^\circ \tag{1.6}$$

and the critical angle for entering total reflection θ_{crit} is calculated as

$$\theta_{crit} = \arcsin \frac{n_2}{n_1}. \tag{1.7}$$

Lensmaker Equation

For optical imaging every ray originating from a given point-object should converge in a corresponding image point. This can be achieved with refraction at curved surface like in aspherical or spherical lenses. The most prominent equation for lense design can be derived by simple geometrical optics consideration and Snell's Law.

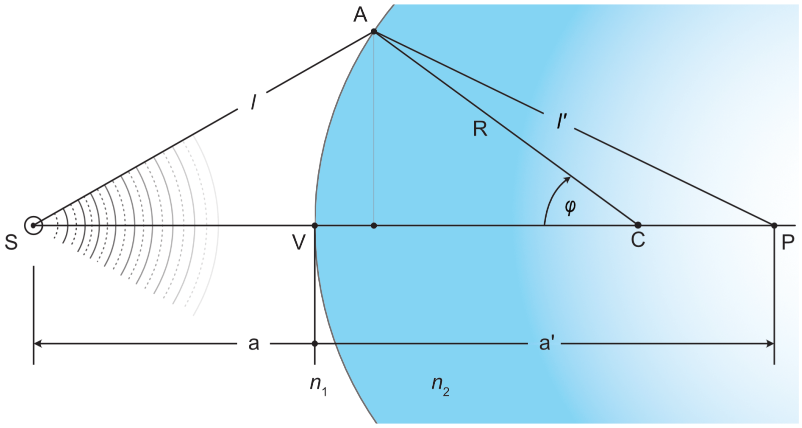

Fig. 1.4 Ray propagation at a curved surface. Point source S emits a spherical wave, entering at distance l and point A the lens with refractive index n_2 is refracted to point P at distance l'. The lens has a centre C with curvature radius R and a vertex at V. Refractive index condition is $n_2 > n_1$. Adapted from [HM17].

As a starting point a ray originating from point source S in medium with refractive index n_1 is refracted at point A by a spherical surface with refractive index n_2 and center C. The deviation occurs according to $n_2 > n_1$ towards the surface normal in point A. The ray crosses the optical axis at point P inside the sphere. The optical path length can now be estimated by the physical path length multiplied with the refractive index according to the *Fermat principle* described above 1.4

$$OPL = n_1 l + n_2 l'. \tag{1.8}$$

With trigonometrical considerations (detailed be found in *Optics* by Eugene Hecht [Hec99]) the physical lengths l and l' can be expressed in dependency of the radius R, distance of S and P to the vertex V of the sphere with a resulting expression for the optical path length

$$\begin{aligned} OPL = n_1 \left[R^2 + (a+R)^2 - 2R(a+R)\cos\varphi\right]^{1/2} \\ + n_2 \left[R^2 + (a'-R)^2 - 2R(a'-R)\cos\varphi\right]^{1/2}. \end{aligned} \tag{1.9}$$

As the equation 1.3 according to Fermat's principle has to be fullfilled and the radius R being constant, the derivative by the angle φ

$$\delta OPL \, d\varphi = 0 \tag{1.10}$$

can be written as

$$\frac{n_1 R(a+R)\sin\varphi}{2l} - \frac{n_2 R(a'-R)\sin\varphi}{2l'} = 0 \tag{1.11}$$

Rearrangement simplifies the equation to the form

$$\frac{n_1}{l} + \frac{n_2}{l'} = \frac{1}{R}\left(\frac{n_2 a'}{l'} - \frac{n_1 a}{l}\right). \tag{1.12}$$

A small angle approximation by keeping only the first order of the Taylor series of the trigonometric functions

$$\begin{aligned} \sin\varphi &= \boldsymbol{\varphi} - \frac{\varphi^3}{3} + \frac{\varphi^5}{5} - \frac{\varphi^7}{7} + ... \\ \cos\varphi &= \mathbf{1} - \frac{\varphi^2}{2} + \frac{\varphi^4}{4} - \frac{\varphi^6}{6} + ... \end{aligned} \tag{1.13}$$

can now be introduced, implying that the deviation of the ray from the optical axis is sufficiently small to assume the approximations of $l \approx a$ and $l' \approx a'$ (see figure 1.4). This approximation is known as *paraxial approximation* in optics and is connected to the *theory of first order* in mathematics. The equation 1.12 is resulting therefore in the final form of

$$\frac{n_1}{a} + \frac{n_2}{a'} = \frac{n_2 - n_1}{R}. \tag{1.14}$$

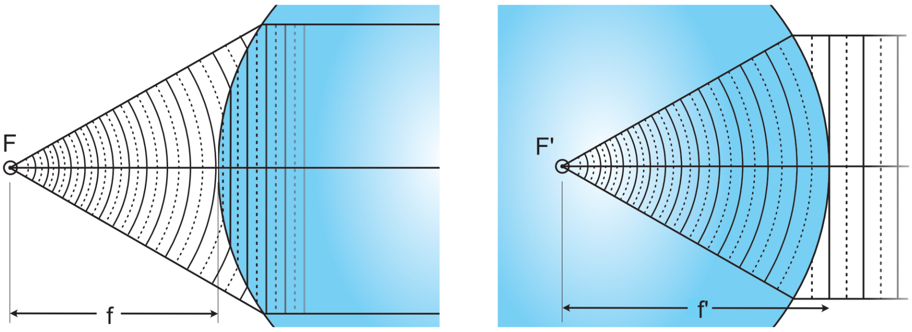

Fig. 1.5 Ray formation by spherical surface. **Left**. A spherical wave emanting from point F at distance of the focal length f is converted to a plane wave inside the lens. **Right**. A spherical wave emitting inside the lens at point F located a focal length f apart from the vertex is turned into a plane wave outside the lens. Adapted from [HM17].

The Gaussian optics, which has been undisputed for almost 200 years, gives this formula immense significance and is an important starting point for further derivations. The two most fundamental optical beam formations by lenses are the generation of a parallel beam bundle from a spherical wave and the focusing of a parallel beam bundle into a point as schematically shown in Figure 1.5. Both beam formations described can be derived by examining the limit values of the distances (a and a') of the respective focal points (S,P) to the vertex V of the sphere as depicted in figure 1.4. The limit values and resulting form of equation 1.14 are therefore

$$\begin{aligned} \lim_{a'\to\infty} \quad & f = \frac{n_1}{n_2 - n_1} R \\ \lim_{a\to\infty} \quad & f' = \frac{n_2}{n_2 - n_1} R. \end{aligned} \tag{1.15}$$

These equations define already the focal lengths of object side (f) and image side (f'). Extending the considerations by combining both in figure 1.5 outlined curvatures a simple biconvex lens is formed. The mathematical and geometrical considerations may be followed in detail in [Hec99]. The reward of this examination is the famous *lens-maker equation*, which is valid for thin lenses (n_l) surrounded by air ($n_{air} \approx 1$) with two individual curvature radii R_1 and R_2:

$$\frac{1}{f} = (n_l - 1)\left[\frac{1}{R_1} - \frac{1}{R_2}\right] \tag{1.16}$$

as well as the *gaussian lens formula* or *thin lense equation*

$$f = \frac{1}{a} + \frac{1}{a'}. \tag{1.17}$$

1.3.2 Image Formation and Limitations

With the preceding chapter image formation can be illustrated and calculated. At first the reproduction scale or magnification is calculated as the ratio

$$M = \frac{a'}{a} = \frac{y'}{y} \tag{1.18}$$

depending on the object distance a and the image formation distance a’.

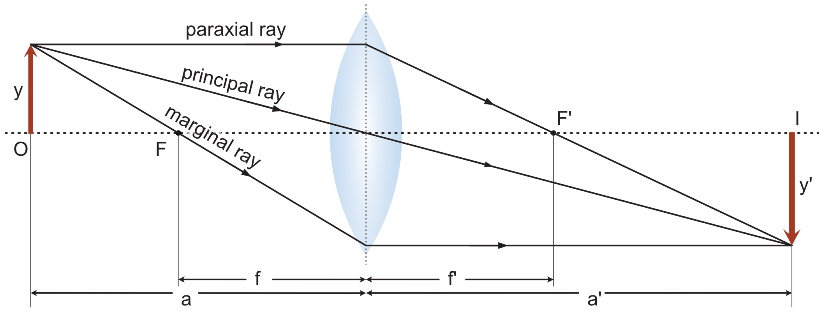

Fig. 1.6 Object O is imaged via a biconvex lens with focal lengths f and f’, respectively focal points F and F’ to an inverted and magnified image I. The magnification can be calculated by the object and image height y and y’. Object distance is denoted as a, image distance as a’ regarding to the main plane of the lens. The three essential rays - *paraxial, principle and marginal ray* - for image construction are drawn as solid lines.

In figure 1.6 the object O (red arrow) is located outside the front focal distance f and the image can be captured at position I. The construction of the image formation underlies mainly 3 basic rays, of which at least 2 are required:

principal ray - ray originating from edge of the object passing through center of the lens

marginal ray - ray originating from edge of the object running through the focal spot F, refracted after passing the lens and proceeding parallel to the optical axis

paraxial ray - ray emanating at the edge of the object and travelling parallel to the optical axis, refracted after passing the lens through back focal spot F’

The intersection point of the rays is the image point to the corresponding object point and the starting point of the rays. The image is real, inverted and by the ratio M magnified, as the condition 3 according to 1.1 is fulfilled.

Table 1.1 Image conditions of thin collecting lenses ($f' > 0$) for object distance, image distance and properties concerning image orientation and size [HM17]

object distance a	image distance a'	properties
$2f' < -a < \infty$	$f' < a' < 2f'$	real, inverted, reduced
$-a = 2f'$	$a' = 2f'$	real, inverted, equal
$f' < -a < 2f'$	$2f' < a' < \infty$	real, inverted, magnified
$-a = f'$	$a' = \infty$	no finite image
$0 < -a < f'$	$a' < 0$	virtual, upright, magnified
$a = 0$	$a' = 0$	virtual, upright, equal

1.3.3 Abberations

The previous design of the optical beams was based on the simplification of Gaussian optics or paraxial optics. Only the first order of the Taylor development in 1.13 was used. The consideration of the third order was developed by the mathematicians Seidel and Petzval in 1950s and is often referred to as the third order error theory [Sei57]. This name derives from the fact that aberrations caused by spherical surfaces can be described by this third order term. The 5 basic imaging errors are here:

- Spherical aberration
- Coma
- Astigmatism
- Petzval Field curvature
- Distortion

In figure 1.7 all mentioned aberrations in comparison to a perfect lens are illustrated.

The *spherical aberration* occurs for rays far from the optical axis entering the lens. The peripheral rays are not focussed anymore in the same plane as the principal ray. A clear focal point can no longer be defined, rather the focal point is axially smeared which leads to a blurring of the image. This deviation is sometimes called spherical longitudinal aberration. The abberation can be largely corrected by a combination of concave and convex lenses. With numerical calculations of ray tracing certain bi-apsheric lenses eliminate nowadays almost entirely the spherical aberration. [GACR18]. Single molecule sensitive microscopy techniques benefit from clearly confined intensity distributions, therefore the reduction of spherical aberration is inevitable.

The image error *coma* occurs at high angles of incidence to the optical axis. A spot-like object is imaged asymmetrically in the image plane smeared, this so-called caustic reminds of a comet tail, which also gives the image its name. Due to the high incident angle coma is often accompanied by a spherical aberration. With the use of aplanate lenses both effects can be minimized.
Astigmatism occurs with increasing distance of an object to the optical axis, because the outgoing rays in relation to the optical axis no longer have rotational symmetry. The beam is divided and the meridional plane including the main beam and the perpendicular sagittal plane including the main beam are considered separately (see figure 1.7). The beams of the meridional plane are focused at a different point than those of the sagittal plane. The focused beam of rays takes on an elliptical shape which is first parallel to the sagittal plane and evolves parallel to the meridional plane with increasing distance to the lens. In between, there is a point with a minimum diameter which has a circular shape. The effect of rotationally symmetric lenses is very small with suitable lens curvature and appropriate positioning of the aperture diaphragm. Astigmatism is amplified by non-rotationally symmetric lenses, such as a cylindrical lens. This has a curved lens surface along only one of the two planes, the light is refracted only one-dimensionally, so to speak.
In case of occurring field curvature (often named Petzval field curvature after Joseph Petzval) the spherical surface of the lens will lead to a focused image correlating to the curvature of the surface. At increasing radial distance from the optical axis, objects will be in focus earlier than in the center. Therefore planar objects might not be imaged sharp over the entire field of view.
Distortions are aberrations that make originally parallel lines appear to be bend. Depending on the curvature of bending they are named either barrel or pincushion. The position of apertures is decisive for the type and strength of distortion [HM17].

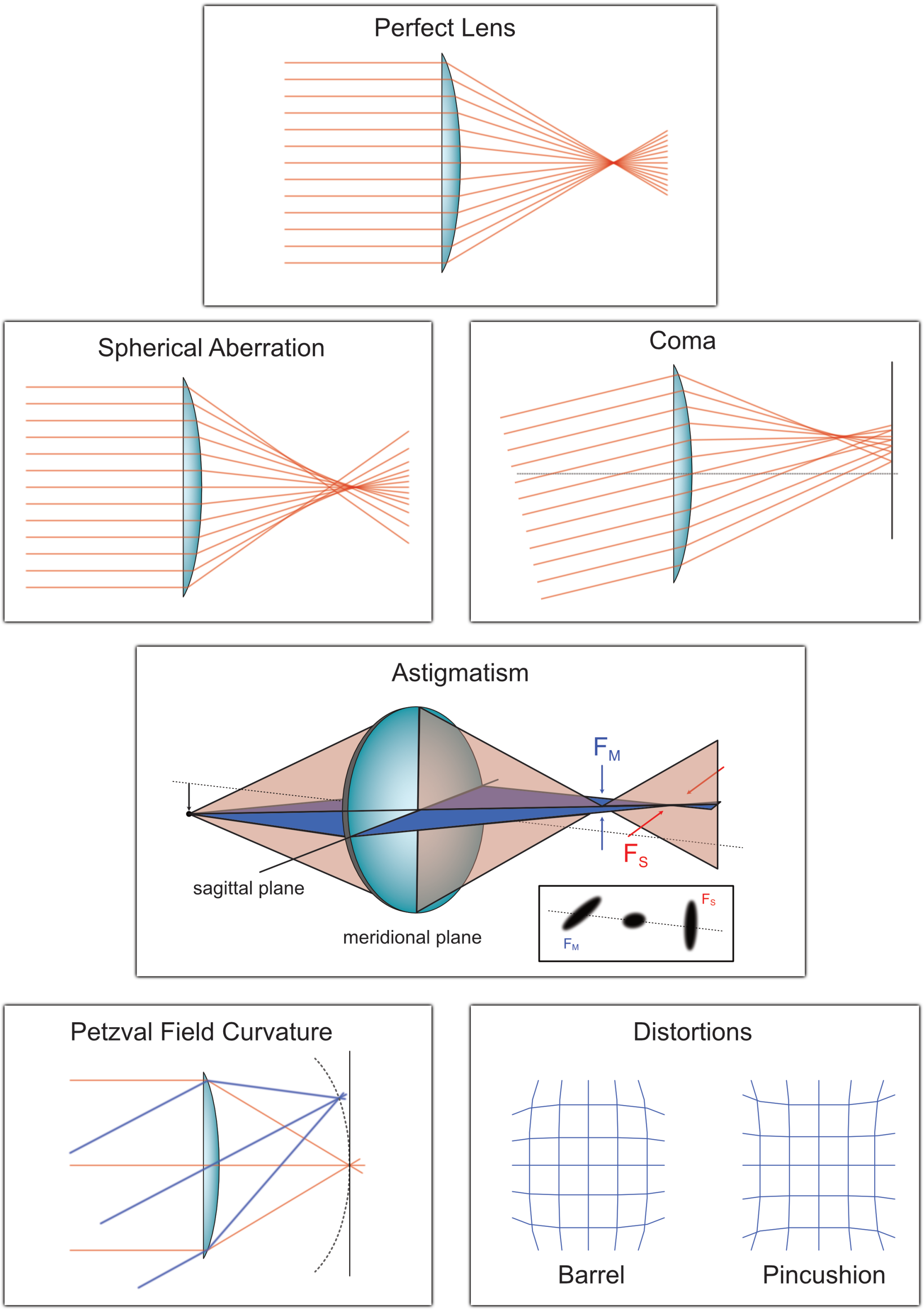

Perfect Lens

Spherical Aberration

Coma

Astigmatism

Petzval Field Curvature

Distortions

Fig. 1.7 Optical aberrations according to Seidel. Aberration free perfect lens followed by spherical aberration, coma, astigmatism with focal point of meridional (F_M) and sagittal (F_S) rays. The inlet shows deformation of a point object at the given focal points and in between. Petzval field curvature and distortions with barrel and pincushion deformation at the bottom.

Chromatic Abberation

The previous abberations all have their origin in the geometric properties of lenses. In addition, there is chromatic aberration, which is caused by the dispersion of light. Dispersion means that the refraction of an incident beam depends on the frequency of the light. In other words, the phase velocity of a wave is a function of frequency. This phenomenon is clearly visible for white light (spectrally wide light) which is fanned out by dispersion into the spectral components.

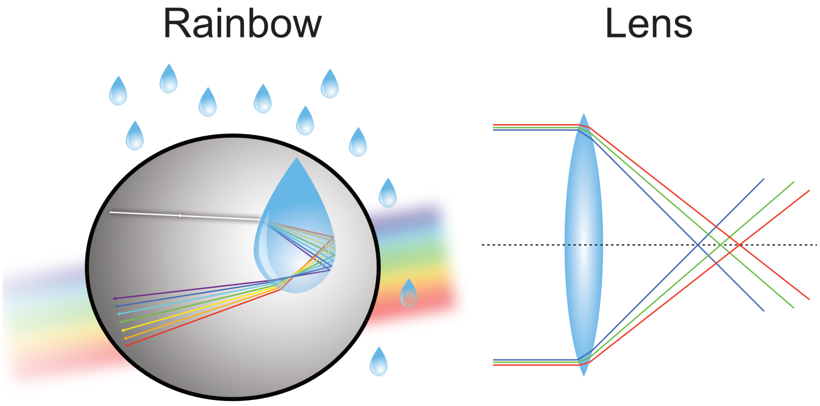

Fig. 1.8 Dispersion of light. Formation of a secondary rainbow due to dispersion of white sunlight and multiple reflection inside the raindroplets. Chromatic aberration of a single lens occurring due to dispersion of incident light, resulting in displaced focal planes depending on the wavelength.

The most vivid example is the rainbow, where the sunlight experiences dispersion in the individual raindrops and is projected back to the observer as a rainbow by multiple reflections. The angle of incidence of the sun into the drops determines the sequence of the spectral band (red-violet, or violet-red). In the figure a so called secondary rainbow with the sequence violet to red is illustrated. The phenomenon of dispersion also occurs in a simple converging lens and is usually referred to as chromatic aberration. The induced error is the wavelength dependence of the focal plane which is generated by the dispersion. By selecting a suitable lens material with appropriate refractive indices and lens shape, lens combinations can be produced that largely compensate for this effect. In the case of achromatic lenses, for example, two focal planes of different wavelengths already lie on top of each other; in the case of apochromatic lenses, three of the observed spectrum lie on top of each other.

Apertures and Telecentricity

In the previous illustrations, the construction beams used were not exposed to any obstacles. In reality, however, there are intentional or natural limitations called aperture or pupil. These are openings in the beam path that partially block beams. The following distinctions are made here:

> **stops** - a stop is basically an adjustable iris that allows to determine the amount of light entering the detection system and is mostly termed *aperture*. In photography the f-stop is defined as *focal length/aperture diameter* and not only enables controlling the amount of light but also the depth of field, as the opening angle of the ray cone connected to the aperture diameter controls the focal depth at the image side.
>
> **pupils** can be seen as images of aperture stops. For microscopy objectives with very short object distances the front lens diameter as well as the exit lens diameter influence the parameter of numerical aperture. Only light traveling in the cones defined by the entrance and exit pupils will be forwarded to the detection system.
>
> *entrance pupils* are defined as the imaged aperture stop when observing from the object plane
>
> *exit pupils* are defined as the image of an aperture spot when observing from the image plane

For object points far away from the optical axis, the beam cone becomes narrower, resulting in vignetting at the edges of the image. Often an effective aperture is shown in schematic drawings, which can be located in the middle of the lens system.
The position of the aperture is decisive for the further path of the ray. This also determines the direction of the principal ray with respect to the optical axis. In the case of a so-called telecentric system, this is parallel in different sections of the imaging system. Figure 1.9 sketches both an object and an image-side telecentric system. Simplified only one lens is shown and an aperture either in front or behind the lens is inserted. If the aperture is in front of the lens, i.e. infinite on the image side, the principal rays on the object side are parallel to the optical axis. The system is called telecentric on the image side. In the case of the object side telecentric system it is exactly the other way round. Telecentric systems allow an orthographic projection, i.e. the magnification by the system does not depend on the position of the object [Edm19]. In the case of a microscope an object side telecentricity is therefore required. Additionally the design of double telecentric systems is possible and would be desirable, nevertheless microscope design is based on object side telecentricity.

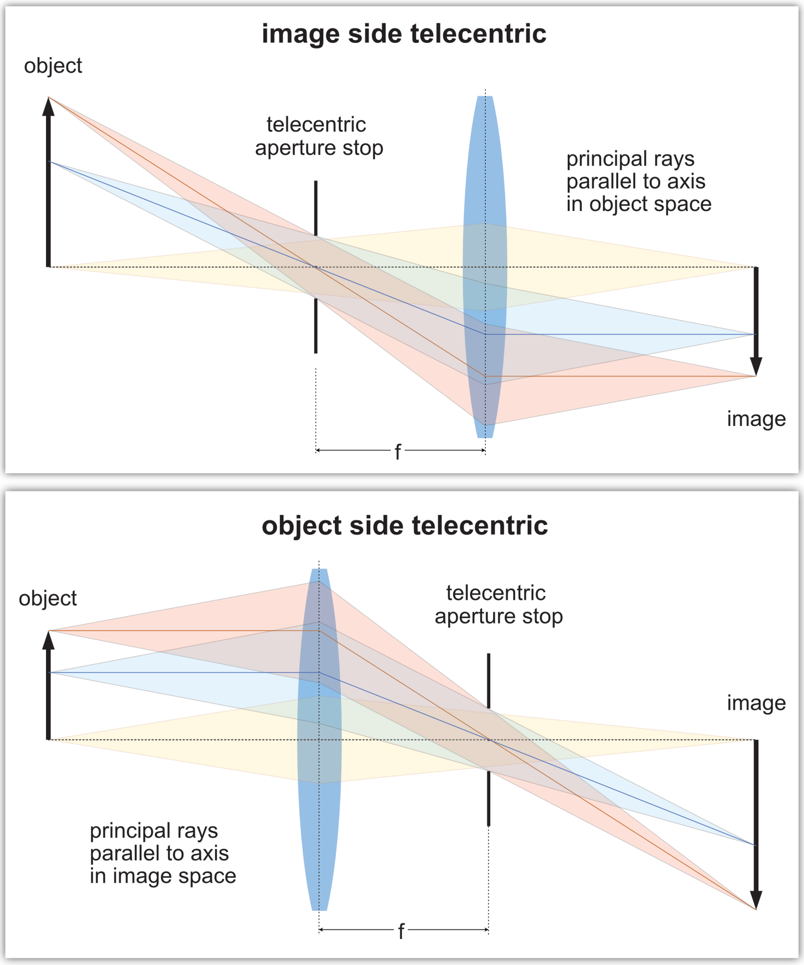

Fig. 1.9 Telecentric design with single lens. The position of the aperture stop decides on which side the principal ray remains parallel to the optical axis. One distinguishes between image side and object side telecentricity.

1.3.4 Image Formation Microscope

Finally the image formation in a microscope can be derived. With former sections the rays can be easily constructed as visualized in schematic 1.10. Rays emanating from a given object are collected by an objective with an opening angle α. The ray bundles are traveling parallel in the infinity space and are imaged by the tube lens onto the conjugated image plane. The resulting image is inverted and real. The marginal ray in red is limited by an effective aperture (not shown) to a distance d from the optical axis. The figure would suggest that the system is telecentric on both sides. To do this, the objective and tube lens would have to be at a distance of the sum of the two focal lengths. The beam construction is ideally represented here. As later experiments have shown, however, the given system must be telecentrically constructed on the object side. At a distance of the objective focal length f_{back} the so called back focal plane is located. In the infinity space optical elements can be inserted, as the parallel ray is most unlikely deviated with proper aligned optics.

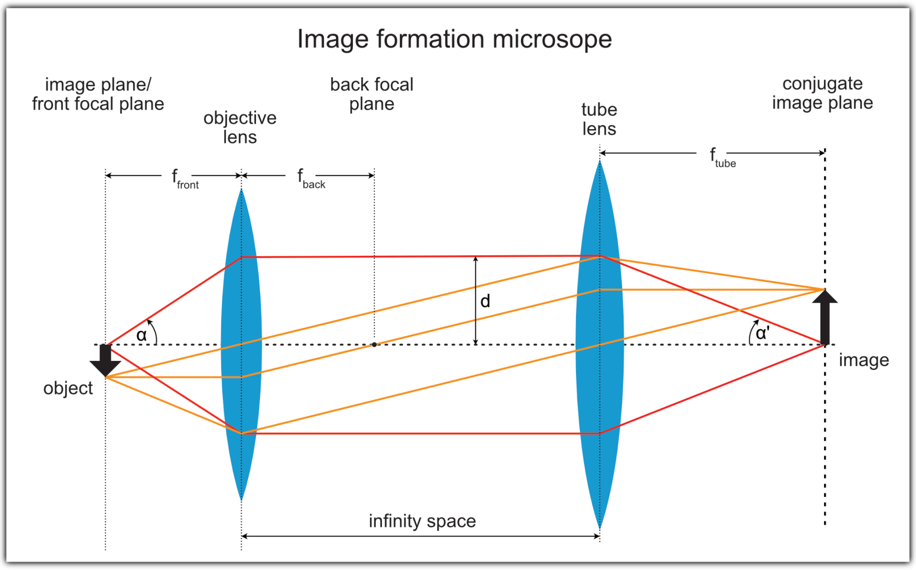

Fig. 1.10 Image formation by an infinity-corrected microscope consisting of an objective and a tube lense. The object is located in the focal plane of the object f_{front}, emanating rays are travelling parallel in the infinity space and are imaged via the tube lens in the conjugated image plane at a distance of f_{tube}. The distance d is the length from optical axis to the paraxial ray.

The magnification M of the final image is determined as the ratio of the focal lengths of the used lens systems

$$M = \frac{f_{tube}}{f_{objective}} \tag{1.19}$$

It is common that the tube lens is variable and allows the user to add an additional post magnification (often 1.5 or 2 fold). The magnification in section 1.3.2 introduced can be extended using the *sine condition* by Ernst Abbe [Abb81]

$$M = \frac{\sin\alpha}{\sin\alpha'} = const \tag{1.20}$$

The equation states a proportionality of opening angles in object and image space. With infinite object distance and parallel ray propagation, $\sin\alpha$ is replaced by the distance d of the paraxial rays to the optical axis and the *sine condition* changes to

$$M = \frac{d}{\sin\alpha'} = f' = const \tag{1.21}$$

So far only geometrical optic has been used to derive image formation. In the following section the wave nature of light should be introduced as well as Fourier Optics, as knowledge of the mathematics behind will extend the further understanding of imaging techniques and their underlying principles.

1.4 Wave and Fourier Optics

The basic wave equation in form of a partial differential equation of second order has the form

$$\nabla^2 u - \frac{1}{c^2}\frac{\partial u^2}{\partial t^2} = 0 \tag{1.22}$$

where the real argument function u is a function of position and time $u(\mathbf{r},t)$ with $r = (x,y,z)$. The differential operations are performed by the Laplacian operator ∇^2 and the partial differentials ∂ . Functions $u(\mathbf{r},t)$ fulfilling this expression 1.22 can be considered as waves, in our case optical waves [ST13]. Wave functions have harmonic time dependencies like a monochromatic wave

$$u(\mathbf{r},t) = A(\mathbf{r})\sin(2\pi kt + \phi(\mathbf{r})) \tag{1.23}$$

with an amplitude $A(\mathbf{r})$, the wavenumber $k = 2\pi/\lambda$ and the phase $\phi(\mathbf{r})$. It is far more convenient to work with these functions as complex wave functions $U(\mathbf{r},t)$ like

$$U(\mathbf{r},t) = A(\mathbf{r}) \cdot exp[i\phi(\mathbf{r})] \cdot exp[ikt] \tag{1.24}$$

and their complex amplitude

$$U_0(\mathbf{r}) = A(\mathbf{r}) \cdot exp[i\phi(\mathbf{r})]. \tag{1.25}$$

By substitution of the complex wave function in equation 1.22 the famous Helmholtz equation is obtained

$$\left(\nabla^2 + k^2\right) U(\mathbf{r}) = 0. \tag{1.26}$$

The spherical wave is one of the solutions of the Helmholtz equation and can be written as

$$U(\mathbf{r}) = \frac{A}{r} exp(-ikr) \tag{1.27}$$

with r as the distance to the origin.

A point source may be generating a spherical wave with λ. At a distance $\vec{r}$ the disturbance can be observed by the complex amplitude transmission function T with constant c

$$U(\vec{r}) = c \int T(r) e^{ik\vec{r}} dr \tag{1.28}$$

or in coordinates with angular dependencies (α_x, α_y) related to the optical axis

$$U(\alpha_x, \alpha_y) = c \int_{-\infty}^{\infty} \int_{-\infty}^{\infty} T(x,y) e^{i\frac{2\pi}{\lambda}(x \sin\alpha_x + y \sin\alpha_y)} dxdy. \tag{1.29}$$

This is the mathematical formulation of the Huygens principle of a wavelet formation [Kub13].

If the point source is located in the focal plane of the objective lens (focal length f), the following expressions are valid according to the *sine condition* in equation 1.21:

$$\begin{aligned} \sin\alpha_x &= \frac{-p}{f} \\ \sin\alpha_y &= \frac{-q}{f}. \end{aligned} \tag{1.30}$$

The signs were used according to the derivation in Kubitschek [Kub13]. The diffraction pattern can therefore be written as

$$U(p,q) = c \int_{-\infty}^{\infty} \int_{-\infty}^{\infty} T(x,y) e^{-i\frac{2\pi}{\lambda f}(px+qy)} dxdy \tag{1.31}$$

and represents a Fourier transform pair [Rah11] in the form of

$$g(y) = \int_{-\infty}^{\infty} f(x) e^{-2\pi ixy} dy = \mathscr{F}(f(x)). \tag{1.32}$$

By choosing the constant c as $1/2\pi$ and identification of the Fourier frequencies

$$\begin{aligned} \omega_x &= \frac{2\pi p}{\lambda f} = -\frac{2\pi}{\lambda} \sin\alpha_x \\ \omega_y &= \frac{2\pi q}{\lambda f} = -\frac{2\pi}{\lambda} \sin\alpha_y \end{aligned} \tag{1.33}$$

the function $U(\omega_x, \omega_y)$ is representing the Fourier transform $\mathscr{F}$ of the amplitude transmission function T

$$U(\omega_x, \omega_y) = \frac{1}{2\pi} \int_{-\infty}^{\infty} T(x,y) e^{-i(\omega_x + \omega_y y)} dxdy = \mathscr{F}(T(x,y)). \tag{1.34}$$

The Fourier spectrum can therefore directly be obtained by applying the Fourier transform on the transmission function. The linear dependency of the Fourier frequencies and their correlated locations p,q in the back focal plane allows the conclusion of an undistorted transformation of the real space to the Fourier space [vB71]. The diffraction pattern in the back focal plane in the form of a Fourier spectrum can be retrieved by an inverse Fourier transform $\mathscr{F}^{-1}$

$$\mathscr{F}^{-1}\left\{U(\omega_x,\omega_y)\right\} = \frac{1}{2\pi}\int_{-\infty}^{\infty} U(\omega_x,\omega_y)e^{i(\omega_x x-\omega_y y)}d\omega_x d\omega_y = T(x,y) \tag{1.35}$$

using an additional lens (for example the tube lens) and imaged in real space. The assumption for this undistorted back transformation are ideal lenses, which do not alter either the phase nor the amplitude of the Fourier frequencies in the back focal plane. Any modification of the frequencies $M(\omega_x,\omega_y)$ can be introduced by a simple multiplication and the retrieved transmission function T will be changed to T' as

$$\mathscr{F}^{-1}\left\{U'(\omega_x,\omega_y)\right\} = \mathscr{F}^{-1}\left\{U(\omega_x,\omega_y)M(\omega_x,\omega_y)\right\} = T'(x',y'). \tag{1.36}$$

The derivation of these expressions are essential for further understanding of important optical properties as the transmitted frequencies and therefore optical resolution as well as the diffraction pattern itself.

1.4.1 Diffraction limit

The optical path is in every optical system limited in space. The aperture introduced earlier are boundaries for rays and block light from exiting towards the detector. The effective aperture close to the back focal plan located at the mounting end of the objective is a circular aperture which is limiting the transmission of frequencies.

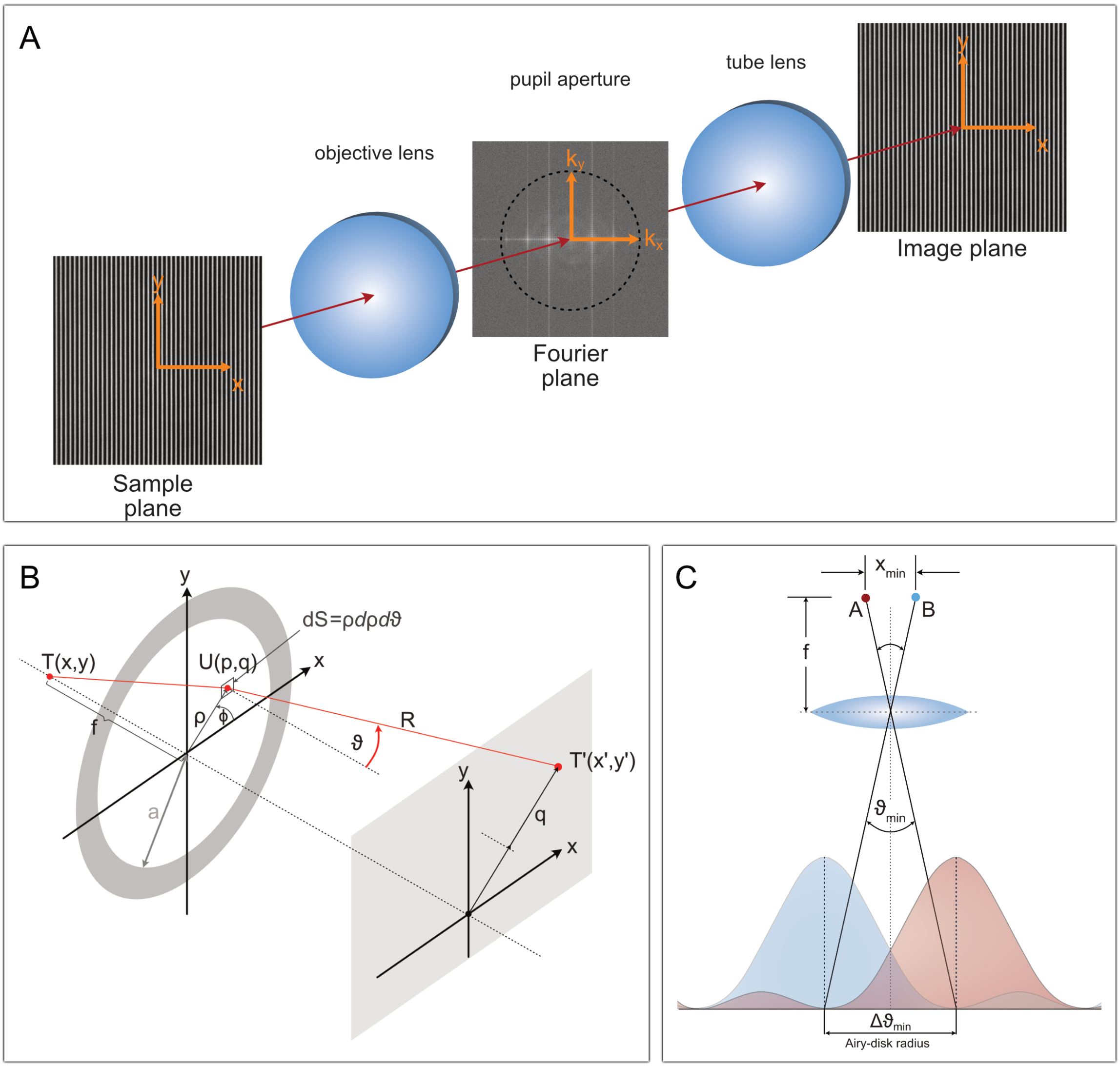

Fig. 1.11 Results of transformation to Fourier Space and back. **A**. Grid represented in real space (Sample plane), transformed by objective lens into Fourier space (Fourier Plane) and back to real space (image plane) by tube lens. **B**. Schematic of interference of spherical wave originating from T with circular aperture (gray ring) with diameter a. The far field pattern is observed at point T', at distance R and angle θ from the point U located in the aperture plane. **C**. Airy pattern of two point emitter A and B satisfying the Rayleigh resolution criterion. The point sources are in the focal plane x_{min} apart, the maxima in the image plane are one Airy radius $\Delta\theta_{min}$ apart. *B* adapted from [Wol13].

Mathematically this circular aperture A_{circ} radius a can be seen as a modification of the Fourier spectrum and expression 1.36 can be rewritten as

$$\mathscr{F}^{-1}\left\{U'(\omega_x,\omega_y)\right\} = \mathscr{F}^{-1}\left\{U(\omega_x,\omega_y)A_{circ}(x,y)\right\} = T'(x',y') \qquad (1.37)$$

The circular aperture can be expressed by a $circ(r)$ function

$$circ(r) = \begin{cases} 1 & r \leq 1 \\ 0 & r > 1 \end{cases} \tag{1.38}$$

In general fourier transforms applied on 2D circular symmetric functions will have the form

$$\mathscr{F}(\rho\phi) = \int_0^{2\pi} \int_0^{\infty} f(r) J_0(k\rho r) dS \tag{1.39}$$

which is known as Fourier-Bessel transform. The expression J_0 is the zero order Bessel function [AS13] and can be written as

$$\begin{aligned} discrete \qquad & J_0(r) = \sum_{k=0}^{\infty} (-1)^k \frac{\left(\frac{1}{4}r^2\right)^k}{(k!)^2} \\ continuous \qquad & J_0(r) = \frac{1}{\pi} \int_0^{\pi} e^{ir\cos\theta} d\theta. \end{aligned} \tag{1.40}$$

Using the convolution theorem [Bra00]

$$\mathscr{F}(f * g) = \mathscr{F}(f)\mathscr{F}(g) \tag{1.41}$$

the factors of equation 1.37 can be evaluated individually.
With the definition of the circ function (1.38) and the radius a the diffraction integral yields

$$T'(p,q) = 2\pi C \int_{\rho=0}^{a} J_0(k\rho q/R) \rho d\rho = 2\pi C \, \frac{a \cdot J_1(kaq/R)}{kaq/R} \tag{1.42}$$

by using the recurrence relation [WW12] to gain first order Bessel function J_1.
The intensity I as the squared amplitude function can be written as

$$I = \left|T'\right|^2 = T_0 \left[\frac{2J_1(kaq/R)}{kaq/R}\right]^2. \tag{1.43}$$

The essential outcome of this derivation is gained by looking back to equation 1.37, as the transmission function is modulated with the Bessel function induced by the circular aperture. A plane wave passing through an optical system with a circular aperture will be imaged in the far field with an intensity distribution I. Insertion of a tube lens projects the diffraction pattern to its focal plane. The *Fraunhofer* diffraction is valid only in the far field, the near field conditions are met by the *Fresnel* diffraction. The interested reader will find further explanation in *Progress in Optics* by Born&Wolf [Wol13].

In figure 1.11 C the sideview of the intensity distribution of a diffraction pattern is shown. These pattern is termed *Airy disk* after George Airy [Geo35] and is expressed as the *Airy function* containing modified Bessel functions of the first order [Wat96]. The imaged *Airy pattern* is a direct measure of how compact a point source can be focused by a given optical system. This imaging function that characterizes any optical system is called *Point-Spread-Function* (PSF).

The width of the PSF is defining how general intensity patterns are resolved. A first definition for resolution can be derived from former equations. The position of the intensity minima and the width of the intensity maxima are decisive for this. For this purpose, the zeros of the Bessel function can be used. The zeros can be found in tabular form in the literature (e.g. [KKN11]), in the following the first three zeros are listed exemplarily for the argument of the bessel function J_1:

$$\frac{kaq}{R} = \begin{cases} 3.8317 \\ 7.0156 \\ 10.1735 \end{cases} \tag{1.44}$$

The argument of the Bessel function can be expressed with the wave number $k = 2\pi/\lambda$ and the diameter $D = 2a$. If the diffraction pattern is mapped onto the surface with a lens of focal length f, $R \approx f$ is a valid approximation.
The first minimum of the Airy Disk occurs therefore at a radius

$$q_{min_0} = 1.22\,\frac{f\lambda}{2a}. \tag{1.45}$$

With this expression also the resolution criterion according to Rayleigh [Ray96] can be derived directly. Two point emitters A and B as shown in figure 1.11 can be resolved when the main maximum of one Airy function is superimposed with the first secondary maximum of the other Airy function, corresponding to the radius of the first minimum q_{min_0}. By means of the relation $sin\theta = q/R$ and the small angle approximation $\theta \approx q/R$ the minimal distance x_{min} of the point emitters A and B in figure can be specified as

$$x_{min} = 1.22\frac{\lambda}{D} = 0.61\frac{\lambda}{a} \tag{1.46}$$

and can be transformed into the final form of the Rayleigh criterion including the opening angle α of the objective and the refractive index n of the immersion oil

$$x_{min} = \frac{0.61\lambda}{n \sin\alpha}. \tag{1.47}$$

The minimal resolvable distance of a given optical system depends therefore on the numerical aperture $NA = n \sin\alpha$ and the used wavelength λ. This equation is valid for the lateral resolution only. The interference of the waves do not only form an intensity distribution in the primary image plane, but also in the space before and behind. The axial intensity distribution can be derived accordingly (shown in Born and Wolf [Wol13]) and the Rayleigh criterion with superposition of first maximum and minimum yields a minimal resolvable distance in z-direction

$$z_{min} = \frac{2\lambda n}{NA^2}. \tag{1.48}$$

In the plane with the most compact diffraction pattern, the main maximum of the diffraction pattern of a single emitter accumulates about 84% of the total intensity. In defocused planes this intensity is distributed to the minor maxima accordingly. This redistribution is used, for example, for the 3D decoding of single molecule microscopy, since a radial aperture can be used to relate the intensity distribution to the main maximum with the axial position. The technique of *temporal, radial-aperture-based intensity estimation* (TRABI) was developed at the Chair of Biotechnology and Biophysics by Christian Franke [FSv16] and allows to decode the 3D position of single molecules by evaluation of intensity contained in each emission pattern.

1.4.2 Optical Transfer Function - OTF

In the previous section the point spread function was introduced, an intrinsic function of every optical system, which maps every point object as an airy pattern into image space. In other words, the PSF filters out fine details from the original object, corresponding to high frequencies in Fourier space. The resolution limit as calculated in equation 1.47 corresponds to a cut off frequency that can be transmitted with the system in use. The limiting parameter is (besides the wavelength) the numerical aperture and thus the collection cone. The PSF is an imaging function of the entire optical system in real space. By means of a Fourier transformation of the PSF

$$OTF(k_x, x_z) = \mathscr{F}\left\{PSF(x,z)\right\} \tag{1.49}$$

the so-called *Optical Transfer Function* (OTF) is obtained. The OTF thus describes the transmission range of the frequencies present in the object. The transfer power of frequencies (usually indicated in line pairs/mm or cycles/mm) decreases with increasing frequencies and reaches for a diffraction limited system a cut-off frequency ω_{lim}, which correlates directly with the resolution limit.

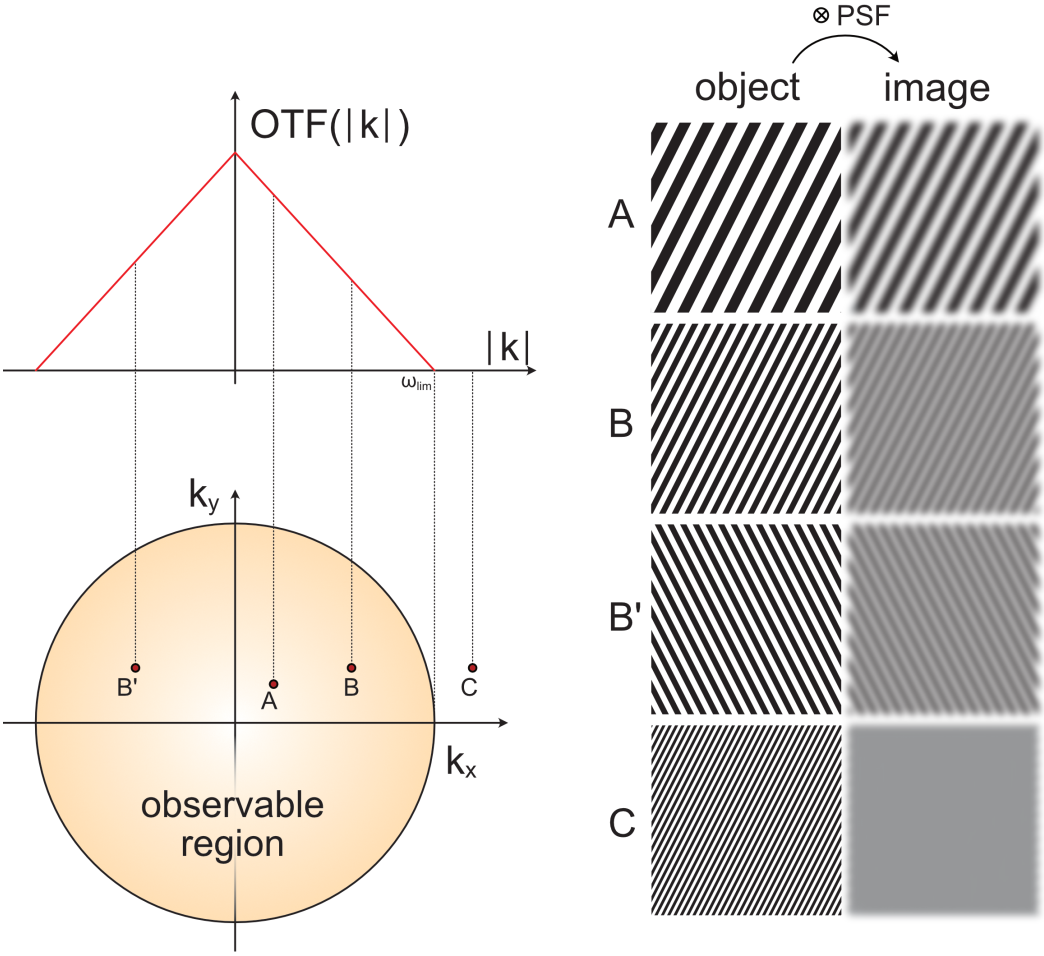

Fig. 1.12 Relationship of object space and fourier space with Optical Transfer Function (OTF). Objects (A-C) with different decreasing frequencies and rotation (B') are convolved with the PSF resulting in a blurred image. The corresponding frequencies with their wave vectors (k_x, k_y) can be transferred to the Fourier space (bottom left). The observable wave vectors are restricted by the corresponding limit frequency ω_{lim}. The OTF is the measure of transmittable wave vectors or frequencies.

The figure 1.12 shows the relationships between OTF, Fourier space and imaging function. Objects with different, decreasing frequencies are represented blurred by the convolution with the PSF. The associated frequencies can be found at the corresponding points in the Fourier space. The optical system contains only frequencies in the marked circle whose radius is determined by the maximum transmittable limit frequency ω_{min}. The transmission power (OTF) of the system of frequencies into the Fourier space therefore decreases steadily up to the cut-off frequency.

1.4.3 Phase Modulation

We have seen so far that the far field amplitude distribution epxressed in equation 1.28 describes the representation of the magnitude of frequencies contained in the transmitted image. The phase of the transmission function T is hidden in the constant c, a mathematical complete expression of far field distribution $U(x,y)$ would be

$$U(u,v) = A(x,y) \cdot \int T(x,y) dx dy \tag{1.50}$$

with the phase factor $A(x,y)$. The far field distribution can be written as

$$U = A \cdot \mathscr{F}(T(x,y)) \tag{1.51}$$

with a separated phase function A. The separation of magnitude and phase should be emphasized, as it is of utmost importance for image formation. Phase and amplitude can not be individually used for image formation, but can be individually modified. A phase modulation in the fourier space does not change the magnitude and vice versa, but it will change the final image obtained by an inverse Fourier transform of the fourier space.

In 1934 Fritz Zernike formulated so-called circular surface polynomials based on calculations of aberrations on mirror surfaces [von34]. The phase modulation by means of a phase ring, located in the back focal plane of a transmitted light microscope, and the associated invention of the phase contrast microscope brought Zernike the Nobel Prize in 1953 [Stu13]. The initial polynoms are defined on the unit circle, therefore the polar coordinate system is used for further description. Originally, a wavefront $W(\rho, \theta)$ is described by a series of polynomials, which in turn are orthonormal to the unit circle, i.e. the circular aperture:

$$W(\rho, \phi) = \sum_{n,m} c_n^m Z_n^m(\rho, \phi) \tag{1.52}$$

The Zernike polynome itself is defined as

$$Z_n^m(\rho, \phi) = R_n^m(\rho) \cdot \begin{cases} \sin(m\phi) & for\, m < 0 \\ \cos(m\phi) & for\, m > 0 \\ 1 & for\, m = 0 \end{cases} \tag{1.53}$$

with index n as radial, index m as azimuthal contribution.
The Zernike polynomials are termed orthonormal [BW54] if the following condition is valid

$$\frac{1}{\pi}\int_0^1\int_0^{2\pi} Z_n^m(\rho,\phi)Z_{n'}^{m'}(\rho,\phi)\rho d\rho d\phi = \delta_{nn'}\delta_{mm'} \tag{1.54}$$

with the *Kronecker-Delta* relation

$$\delta_{ij} = \begin{cases} 1 & for\, i = j \\ 0 & for\, i \neq j. \end{cases} \tag{1.55}$$

The radial function $R_n^m(\rho)$ is split into odd and even values of $n-m$

$$R_n^m(\rho) = \begin{cases} \sum\limits_{l=0}^{(n-m)/2} \frac{(-1)^l(n-l)!}{l!\left[\frac{1}{2}(n+m)-l\right]!\left[\frac{1}{2}(n-m)-l\right]!}\rho^{n-2l} & for\ (n-m)\ even \\ 0 & for\ (n-m)\ odd \end{cases} \tag{1.56}$$

The first radial polynoms with non zeros values can be found in literature like [Wol13]

$$\begin{aligned} R_0^0(\rho) &= 1 \\ R_1^1(\rho) &= \rho \\ R_2^0(\rho) &= 2\rho^2 - 1 \\ R_2^2(\rho) &= \rho^2 \\ R_1^3(\rho) &= 3\rho^3 - 2\rho \\ &\dots \end{aligned} \tag{1.57}$$

Combining the radial polynoms with expression 1.53 the Zernike polynoms can be calculated as shown in table 1.2. For the indices m and n the corresponding Zernike coefficient is listed in polar coordinates together with the interpretation in the image space [MM13]. Additionally the Noll coefficient is listed as it is used by convention in most optical devices [Nol76]. The beauty of the Zernike coefficients and their effect on the phase due to a circular aperture in the fourier space is the direct relation to all the fundamental aberrations. The effect of the Zernike coefficient is listed in the interpretation column.

Table 1.2 Zernike coefficients with corresponding radial function R and their interpretation. Indices for radial degree n, azimuthal degree m and the corresponding *Noll* index are listed.

Z_n^m	Radial degree n	Azimuthal degree m	Noll index j	R(n,m)	Interpretation
Z_0^0	0	0	1	1	Piston
Z_1^{-1}	1	-1	3	$\rho\cos\phi$	Y-Tilt
Z_1^1	1	+1	2	$\rho\sin\phi$	X-Tilt
Z_2^{-2}	2	-2	5	$\rho^2\cos 2\phi$	Astigmatism
Z_2^0	2	0	4	$2\rho^2-1$	Defocus
Z_2^2	2	+2	6	$\rho^2\sin 2\phi$	Astigmatism 45°
Z_3^{-3}	3	-3	9	$\rho^3\cos 3\phi$	X-Trefoil
Z_3^{-1}	3	-1	7	$(3\rho^3-2\rho)\cos\phi$	Y-Coma
Z_3^1	3	+1	8	$(3\rho^3-2\rho)\sin\phi$	X-Coma
Z_3^3	3	+3	10	$\rho^3\sin 3\phi$	X-Trefoil
Z_4^{-4}	4	-4	15	$\rho^4\cos 4\phi$	Quadrafoil 45°
Z_4^{-2}	4	-2	13	$(4\rho^4-3\rho^2)\cos 2\phi$	Astigmatism (2nd) 45°
Z_4^0	4	0	11	$6\rho^4-6\rho^2+1$	spheric. Aberration
Z_4^2	4	+2	12	$(4\rho^4-3\rho^2)\sin 2\phi$	Astigmatism (2nd)
Z_4^4	4	+4	14	$\rho^4\sin 4\phi$	Quadrafoil

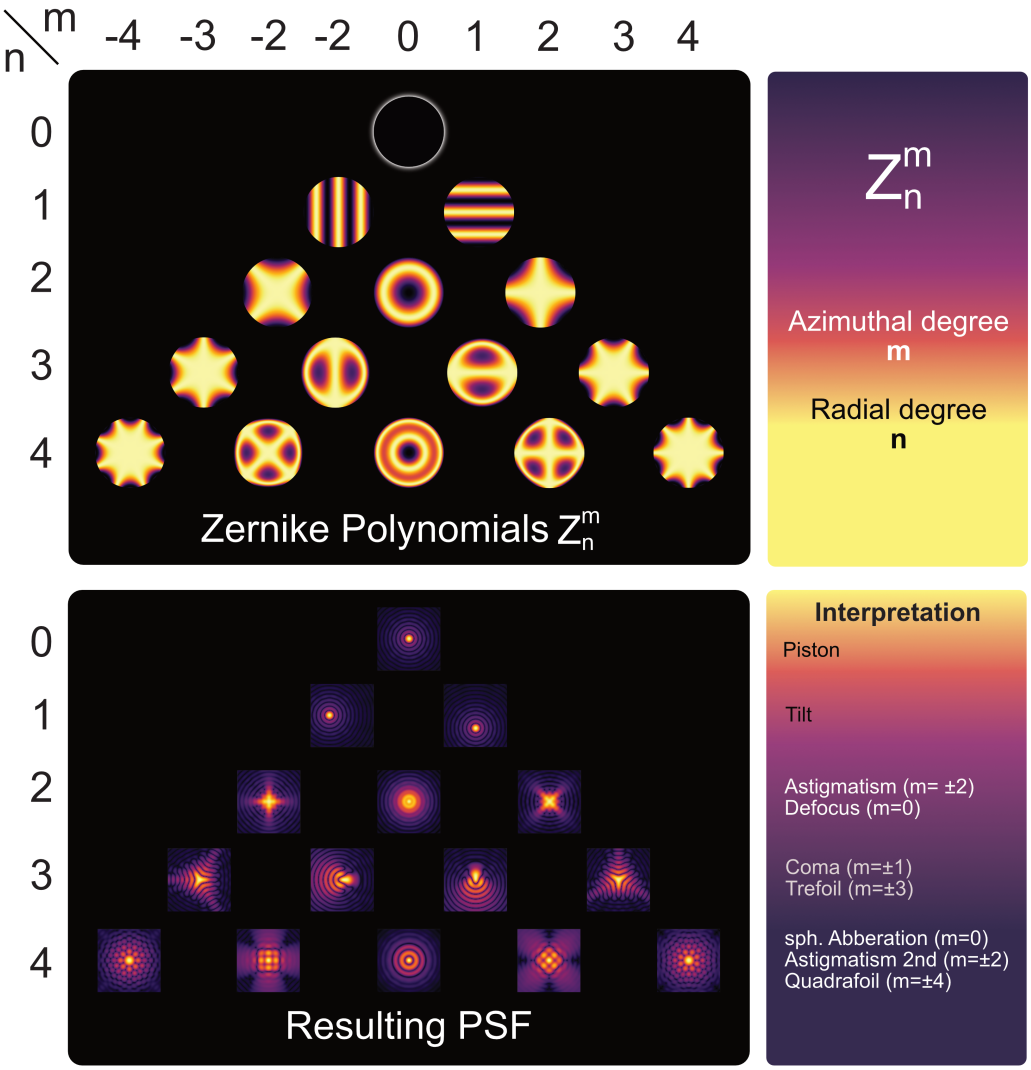

Fig. 1.13 The first 15 Zernike Polynomials Z_n^m on a uniform circle and their corresponding Point-Spread-Function created with Mathematica Script from James C. Wyant [Jam13]. The interpretation of the effect on resulting PSFs is listed in the bottom right box, related to each line.

1.5 Imaging techniques

In recent decades microscopy has undergone an incredible development. Actually, microscopy had physical limitations due to the existing diffraction limit. Already with the invention of the confocal microscope in 1961 by Marvin Minsky [Mar61], it was possible to break the resolution limit. The further development of the confocal laser scanning microscope (CLSM) into an image scanning system by Sheppard in 1988 [She88] went largely unnoticed. Almost 20 years later, this system was rediscovered by Müller&Enderlein [ME10] and has since become one of the established imaging techniques in research. In 1994, the foundation was laid for another spot scanning technique, which is also one of the super-resolution microscopy techniques. The STED technology (stimulated emission depletion) is associated with Hell&Wichmann [HW94], the first of which was awarded the Nobel Prize in 2014 [The14a]. Several names are associated with the use of structured illumination microscopy (SIM) and the associated resolution gain of a factor of 2, e.g. Lukosz&Marchand with theoretical considerations in 1963 [LM63]. However, the implementation of today's SIM remains the legacy of Matts Gustafsson [Gus00][GSC$^+$08].

In addition to conventional techniques based on optical modulations, the discovery of photoactivatable fluorescent proteins by Eric Betzig in 2006 opened the chapter of stochastic super-resolution microscopy by single molecule localization. In addition to photo-activated localisation microscopy (PALM)[BPS$^+$06], other techniques such as stochastical optical reconstruction microscopy (STORM) [RBZ06], *d*STORM [HvS$^+$08], [vS14] and points accumulation for imaging in nanoscale topography (PAINT) [SH06][JSS$^+$10] were developed using synthetic dyes.

Even though it does not count as a superresolution technique, the light sheet microscopy developed by Eric Betzig has left an unbelievable influence in the world of microscopy. With deconvolution, adaptive optics, and complex beam shaping, this technique is the measure of all things for volumetric imaging [CLW$^+$14], [LUM$^+$18]. Betzig was also awarded the Nobel Prize (Chemistry) in 2014 for his contribution in the field of fluorescence super resolution microscopy. Furthermore, light sheet microscopy with almost isotropic resolution offers the best imaging technique for expansion microscopy (ExM) [GAU$^+$19]. Expansion microscopy was developed by Edward Boyden as an alternative strategy to achieve higher structural resolution [CTB15]. It physically enlarges the sample by embedding and swelling it with a gel, bypassing the optical resolution limit. Combined with the above imaging techniques, ExM offers unprecedented possibilities for fluorescent microscopy analysis.

In the following section the spot scanning techniques CSLM and ISM as well as the single molecule technique *d*STORM will be explained in detail, as these techniques are relevant for this thesis.

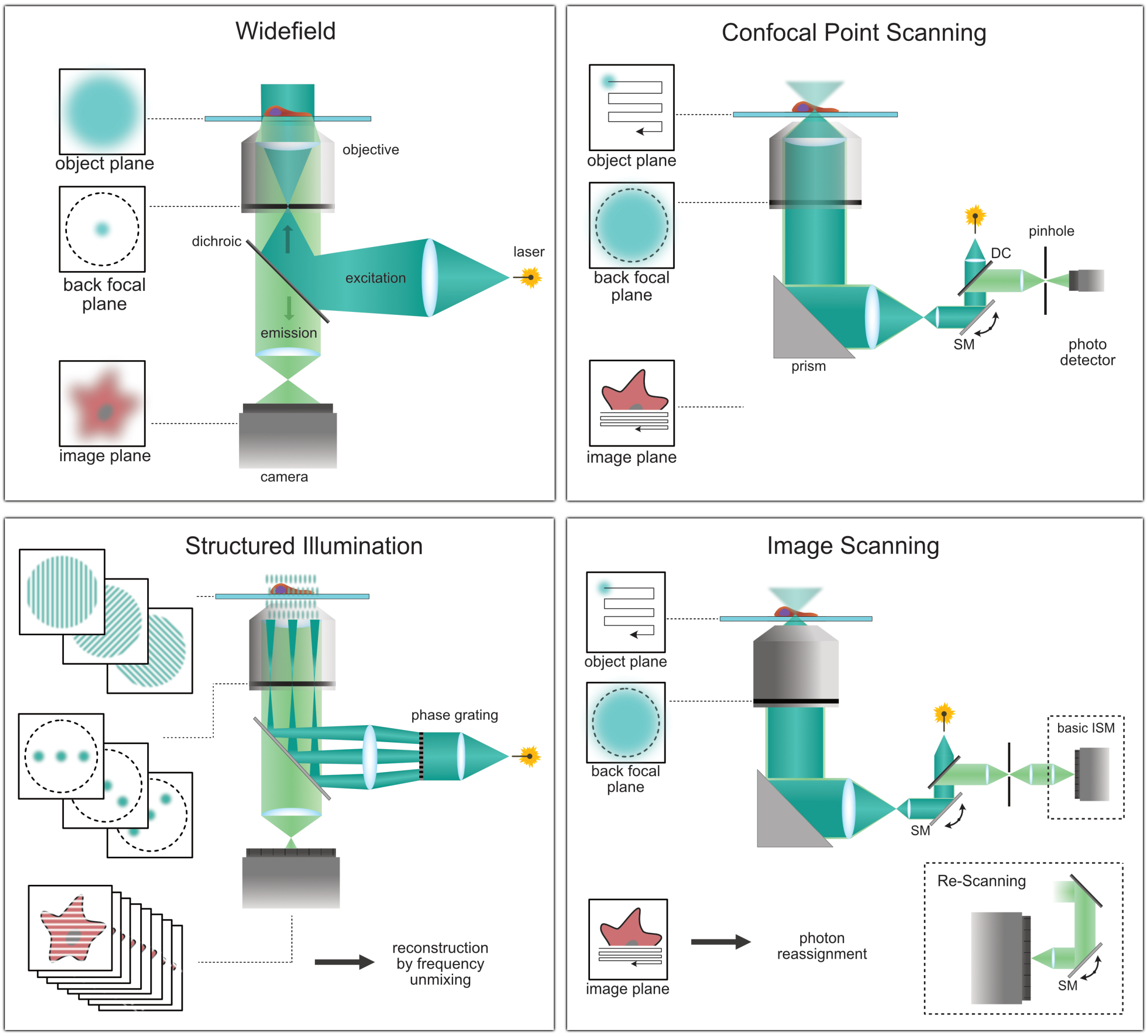

Fig. 1.14 Fluorescence Microscopy techniques with excitation and emission paths. Illumination properties are indicated in backfocal plane and object plane as well as resulting image and required computational steps. **Widefield** illumination results from focusing the excitation beam onto the back focal plane, this focused spot correlates to a homogeneous illumination in the object plane. **Confocal Point Scanning** microscopy is achieved by a filled back focal plane resulting in an excitation spot in the object plane. This spot is scanned across the sample and the emission light collected by a point detector. The pinhole is located in the conjugated object plane. **Structured Illumination** microscopy (SIM) is realized by creating excitation patterns with a phase grating. Interference of the object with rotating excitation patterns can be used for reconstruction. **Image Scanning** microscopy is based on confocal point scanning with a pixel array as detector. The required photon reassignment can be done computationally in basic ISM or opto-mechanical in case of the Re-Scanning path with a second scanning mirror (SM). Adapted from *Super-resolution microscopy demystified* [SFH+19].

An overview of the most common imaging techniques is shown in figure 1.14. The excitation and emission light paths for wide field, confocal point scanning, structured illumination and image scanning microscopy are illustrated here. In wide field microscopy, the excitation beam is focused into the back focal plane, which in turn results in a parallel beam through the front focal plane and thus in a homogeneous illumination of the object plane. The emission light is separated from the excitation light by a dichroic filter and detected by a camera. The illumination is homogeneous in the central region, but has an overall Gaussian profile. With optical elements, this Gaussian profile can be smoothed to a Tophat profile, for example. In single molecule microscopy, the excitation power correlates directly with the photoswitching of the dyes (1.5.3), therefore the area to be measured should be chosen carefully.

In the case of a point excitation system, the excitation beam is coupled in parallel through the backfocal plane via a scanning mirror, resulting in focusing in an excitation spot. The focusing depends on the numerical aperture of the objective. However, not only the volume of the spot is excited but also the areas in the cone above and below. The spot can now be scanned uni or bidirectionally over the sample by means of the scan mirror, the emission light is descanned again by the scanner and separated by a dichroic mirror. A pinhole placed in a plane conjugated to the sample plane now blocks emission from planes above and below the scanned focal plane. This creates a sectioning of the signal. The emission light is detected by a point detector (e.g. PMT) and written into an image. Almost all microscopy manufacturers have CLSM systems in their portfolio, like SP line from Leica[Lei], LSM series - Zeiss [Zei19a], A1 - Nikon[Nik19].

To create a structured illumination, light is directed onto a phase plate or grating (transmissive or reflective). The periodic pattern is represented in the back focal plane (Fourier plane) according to the frequency. The superposition in the object plane then generates a grid pattern as excitation. The superposition of the object frequencies with the excitation pattern results in moire patterns that are captured by a camera. With excitation profiles, different in rotation and phase an image with 2 times better resolution in all dimensions can be reconstructed by frequency unmixing. However, the reconstruction is time-consuming and prone to artifacts. A perfectly adjusted system and a trained user are therefore advisable. Commercially available systems are e.g. the Elyra from Zeiss [Zei19c], and the N-SIM fom Nikon [Nik18].

An image scanning system is generally defined as a spot scanning system that has a pixel array (e.g. a camera) as its detector. This means that the entire airy pattern is distributed over different pixels, with each pixel acting as a pinhole-point-detector. For this purpose the detector is operated in integrating mode. The photon reassignment as described in the publication OPRA [RSWH13] can be carried out computationally as post-processing like in Enderlein's "Image Scanning Microscope" [ME10]. An elegant solution for instantaneous photon reassignment can be realized optomechanically by using a second scanning mirror to introduce a global magnification by a factor of 2 through a corresponding amplitude ratio. This version is commercially available as Rescan Confocal Microscope as an add-on from Confocal.nl [Con19] and is based on the publication [DBB+13] by de Luca. The image scanning principle increases the resolution in this case, the integration of the additional pinhole retains the sectioning of the standard confocal system. Another commercial variant of the ISM is the Airyscan from Zeiss [Kla01][Zei19b], which has an array of PMTs as detector to image an Airy disk [Huf15]. The lateral resolution improvement of the ISM systems is about 1.4 times (170 nm), in combination with deconvolution the improvement can be increased to 1.7 times or higher.

1.5.1 Widefield vs Spot scanning microscopy

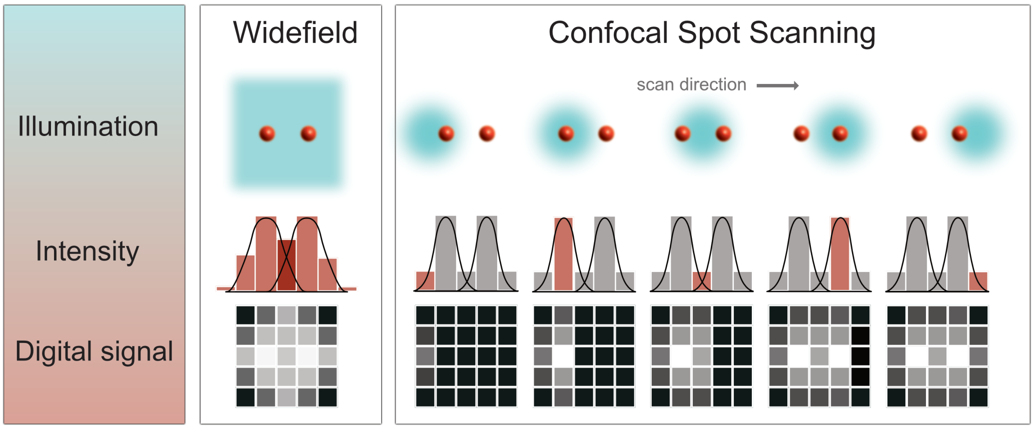

Fig. 1.15 A comparison between widefield illumination and spot scanning illumination microscopy. A target consisting of two spots (red) is imaged by widefield illumination and spot scanning illumination (cyan areas). The intensity distribution acquired by both illumination modes is displayed in pixelated manner for the PSF side view and the digitally converted view. Adapted from [VCS+18].

As explained in the previous section, the simplest fluorescence microscopy technique uses wide-field illumination. Compared to a spot scanning system, there is a big difference in image formation, which will be explained in the following. Figure 1.15 shows the image generation of two fluorescent point sources (red) for the aforementioned techniques. Line by line, the illumination modality (**illumination**), the induced emission distribution of the sample (**intensity**) and the digitally recorded signal (**digital signal**) are schematically displayed [VCS$^+$18].

The *wide field illumination* produces a homogeneous excitation of both point sources. Both point sources emit simultaneously and the emission intensities overlap. The signals that are already superimposed are digitized at the detector.

In the second case of a *spot scanning system*, a smallest possible spot is scanned over the sample as illumination. The excitation spot gradually overlaps with the spot centres. The emission distribution depends on the degree of superposition of excitation and point source as shown schematically in the case of the linear sweep over the two point emitters for the intensity distribution. The intensity is collected sequentially by point detectors and then written virtually into an image. This has the consequence that the contrast is much higher and therefore the resolution can be improved significantly. For the special case of a confocal system, blocking of the out-of-focus signal as well as the limitation due to the pinhole size increases mentioned parameters. A standard confocal microscope can be counted as a super resolution technique, as closing down the detection pinhole narrows the resulting point spread function. The major drawback is the decreasing signal with decreasing pinhole diameter, which limits the resolution improvement.

1.5.2 Image Scanning Microscopy - ISM

If one replaces the point detector of a laser scanning system with an array detector (for example a camera), the system is called an image scanning system. The signal of an object is therefore not collected by a single pixel but distributed over several adjacent pixels. Each individual pixel acts as a combination of pinhole and point detector, which is referred to as micropinhole [MMH15]. The camera integrates the intensities striking each individual pixel during the scanning process. Imagine a static excitation spot, which overlaps centrally with a point emitter. The resulting distribution of the fluorescence intensity is a convolution of excitation PSF and detection PSF. The detection PSF in this case is equivalent to a standard widefield detection. We consider the excitation PSF to be static at position x_0 and therefore take it as a reference. The detection PSF is determined by the micropinholes (pixel). In the simplest case, excitation and detection PSF are on the same axis. However, due to the parallax effect, a different viewing angle is obtained for different positions of both PSFs as shown in Figure 1.16. The effective PSF and thus the most probable detection position is located between excitation and detection PSF at a distance of $a/2$. The detected photons can therefore be traced back to the position of the effective PSF, this process is called pixel reassignment.

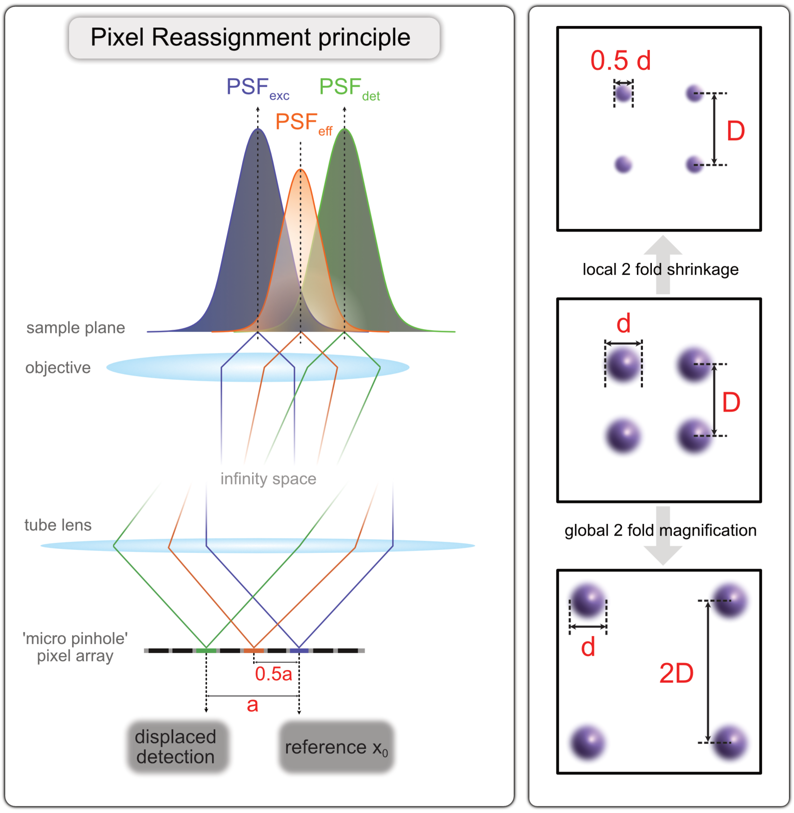

Fig. 1.16 Principle of Pixel Reassignment for Image Scanning Microscopy. **Left**. Detection schematic using a pixel array with 'micro pinholes'.The detected PSF$_{det}$ is displaced from the excitation PSF$_{exc}$ by a distance *a* in respect to the observed pixel (green). The effective PSF$_{eff}$ resulting by convolution of the former ones is located inbetween (orange pixel), shifted by a/2. **Right**. Pixel reassignment strategies with the initial detected image in the middle panel. 4 spots with diameter *d* are arranged at a distance *D* for each. **top**. The displacement of the effective PSF can be reversed by a local shrinkage of a factor 2, affecting only the diameter of the spot. **bottom**. The same results can be achieved by global magnification of 2 altering only the distance *D* while remaining the diameter. *left panel* adapted from [RSWH13], *right panel* adapted from [CWS16].

The process can easily formulated in a mathematical formulation following [GE19]. The PSF can be simplified by a gaussian approximation and the intensity of the excitation I_{exc} expressed as

$$I_{exc}(x_0) \propto exp\left(-\frac{x^2}{2\sigma_{exc}^2}\right) \tag{1.58}$$

together with the intensity of the detection I_det at a displacement a

$$I_{exc}(x_0 - a) \propto exp\left(-\frac{(x-a)^2}{2\sigma_{det}^2}\right). \tag{1.59}$$

The widths of both PSFs are correlating to the standard deviation σ and are therefore proportional to the wavelengths

$$\sigma_{exc} \propto \lambda_{exc} \quad and \quad \sigma_{det} \propto \lambda_{det}. \tag{1.60}$$

The reason why excitation and detection wavelengths are treated separately is simply the occurring Stokes-shift. The effective PSF follows by a convolution of the two gaussians, resulting again in a gaussian function

$$PSF_{eff}(x-m) \propto exp\left(-\frac{(x-m)^2}{2\sigma_{eff}^2}\right) \tag{1.61}$$

with a reduced width σ_{eff}

$$\sigma_{eff} = \left[\frac{1}{\sigma_{exc}^2} + \frac{1}{\sigma_{det}^2}\right]^{-1/2} = \sigma_{det}^2\left[1+\left(\frac{\lambda_{det}}{\lambda_{exc}}\right)^2\right]^{-1/2}. \tag{1.62}$$

For the center position m of the resulting PSF the expression

$$m = a\cdot\frac{\sigma_{exc}^2}{\sigma_{exc}^2+\sigma_{det}^2} = a\left[1+\left(\frac{\lambda_{det}}{\lambda_{exc}}\right)^2\right]^{-1} \tag{1.63}$$

can be derived. If one neglects the Stokes shift occurring between excitation and emission with the assumption of $\lambda_{exc} \approx \lambda_{det}$ two fundamental relations are obtained in relation to image scanning microscopy:

The effective PSF of the ISM in equation 1.62 has a reduced width ($\sigma_{eff} \rightarrow \sigma_{ISM}$) in comparison to the standard widefield detection width σ_{det} by a factor of $\sqrt{2}$

$$\sigma_{ISM} = \frac{\sigma_{det}}{\sqrt{2}}. \tag{1.64}$$

The center position in equation 1.63 of the resulting PSF is located at position

$$m = \frac{a}{2}. \tag{1.65}$$

There are two possibilities to carry out the redistribution of the photons given the position m of the effective PSF. The starting position can be seen in the middle figure of the right panel in figure 1.16. The 4 shown spots have a diameter d and are positioned at a distance of D. In the upper figure, the pixel reassignment is achieved by a local shrinkage with a factor of $m = 1/2$. The distance D is not altered, but the spot size shrinked to $d/2$. In the lower figure, the pixel reassignment is realized by a global magnification by a factor of $m = 2$, remaining the spot size but increasing the distance to $2D$. Both methods achieve the same resulting super resolved image with increased contrast and highly improved signal-to-noise ratio. The underlying mathematical operations (division - shrinkage, magnification - multiplication) can be implemented either computationally, or as in case of the RCM system optomechanically. As already depicted in the inlet of the Image Scanning modality in schematic 1.14, the magnification can be achieved by introducing a second scanner. Synchronized movement with the first scanner but doubled amplitude of the Re-scanner adds a magnification factor of 2 and enables an instant photon reassignment with no further post processing required.

1.5.3 Single molecule localisation microscopy - *d*STORM

In case of a conventional widefield illumination and detection system, the PSF of point emitter will be diffraction limited as we have seen in section 1.4.1 and figure 1.11. Emission patterns will start overlapping when being moved together until the Rayleigh criterion is surpassed and the individual point sources can not be distinguished anymore. This fact seemed physically insurmountable for a long time. The ingenious idea was to solve the lateral resolution limit in a temporal dimension. In the case of two overlapping non-resolvable PSFs, a temporal separation of both PSFs would mean that at time point t_1 emitter 1 would be bright and emitter 2 dark, at time point t_2 vice versa. The PSFs, which are now well separated in time, can be approximated with a 2-dimensional Gauss function using complex algorithms and the center of latter can be determined with high accuracy. Provided that individual PSFs must be easily separable, this process can also be applied to large ensembles of emitters. The mentioned switching on and off of the emitters can be achieved for example by exposing the used fluorophores to a suitable chemical environment ([HvS+08]).

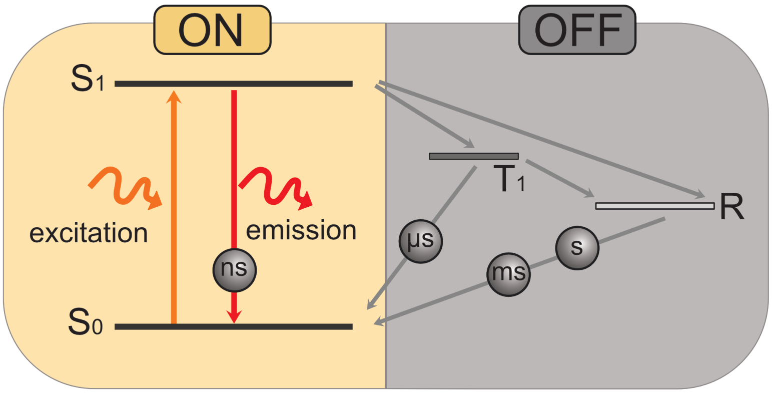

Fig. 1.17 Jablonksy diagram for photoswitching of fluorophores. The excited singlet state S_1 including emission is termed ON state, the lifetime is in the range of nanoseconds. The intersystem crossing to triplet state T_1 and further reduction to reduced form R by chemical buffer induced redox reactions are connected to relaxation times ranging up to seconds. This state is therefore termed OFF state, as fluorescence is efficiently suppressed.

As shown in figure 1.17, two different states of the fluorophores can be induced. In the so-called ON state, the fluorophore relaxes to the ground state within a few nanoseconds after excitation, emitting a photon. With a very low probability, a few times per 1000 excitation cycles, an inter-system crossing occurs, with a transition to the triplet state. In an appropriate chemical environment, this triplet state can be further reduced and, for example, a stable radical anion (R) of the fluorophore can be produced with thiol-containing buffers [vLK$^+$11a]. These states can remain stable for seconds to minutes before relaxation into the ground state occurs. In this state no fluorescence occurs, therefore it is called OFF state. Through high power illumination densities in the range of several $kW cm^{-2}$, corresponding to a high number of excitation cycles, a subset of fluorophores can now be brought into the OFF state. The stochastically occurring photo-switching can now be recorded over several minutes to hours and the position for all individually separable emitters can be localized and projected into a super high-resolution image. The acronym *d*STORM is now self explaining with *d*irect **S**tochastical **O**ptical **R**econstruction **M**icroscopy. The explicit term *direct* refers to inducing the photoswitching without any additional dye partner as is used in STORM [RBZ06].

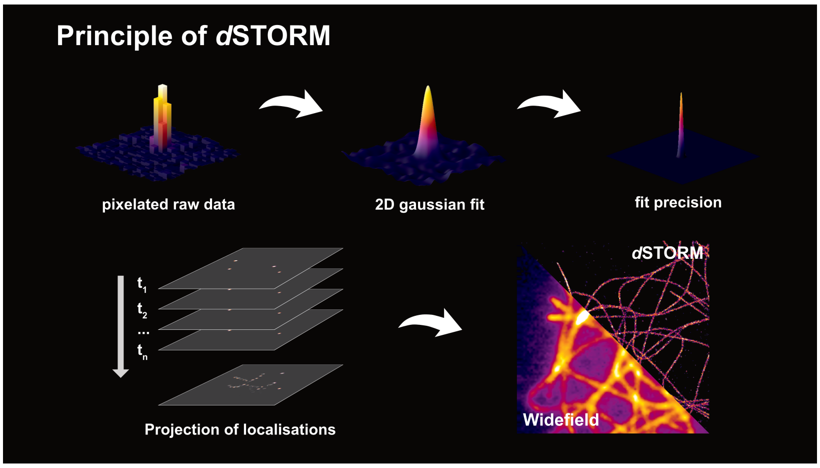

Fig. 1.18 Schematic of obtaining super resolved images by *d*STORM. **Top**. The pixelated raw data represents an emission pattern from a single emitter to which a 2-dimensional Gaussian function is fitted. The center position is retrieved with nanometer precision. **Bottom**. Acquisition of several thousand frames are processed, estimated localisation centers projected into one final image and the super resolved image is obtained. In comparison to a conventional widefield image the resolution is increased by almost one order of magnitude down to 20 nm.

Schematically the process of image reconstruction in *d*STORM is shown in figure 1.18, starting with a digital intensity signal (pixelated raw data) to which a 2-dimensional Gaussian function is fitted. The center coordinate of the gaussian fits are stored for an acquisition of several thousand frames. These coordinates are finally written into one single super resolved image in comparison to a conventional widefield frame. The precision σ_{loc} of the estimated localisation depends strongly on the brightness of the emitter (the emitted photons N_{phot}) and is corrupted by uncertainties induced due to noise types and background

$$\sigma_{loc} \propto \sqrt{shot\ noise + pixelation\ noise + background}. \tag{1.66}$$

Shot noise is induced due to the poisson distribution of the photon flux, the finite pixel size a adds uncertainty to the location. Background due to autofluorescence and camera noise (readout, dark current) is added with an amount of b per pixel [VCS+18]. The mathematical expression has been described by Mortensen [MCSF10] and the preliminary work of Thompson [TLW02]:

$$\sigma_{loc} = \sqrt{\left(\frac{\sigma_{PSF}^2}{N_{phot}}\right) + \left(\frac{a^2/12}{N_{phot}}\right) + \left(\frac{8\pi\sigma_{PSF}^4 b^2}{a^2 N_{phot}^2}\right)} \tag{1.67}$$

and is often simplified to the relation

$$\sigma_{loc} \approx \frac{\sigma_{PSF}}{\sqrt{N_{phot}}}. \tag{1.68}$$

Emission of high photon numbers therefore lower the uncertainty of the estimated emitter position and increase the localisation precision. The remaining contributions of equation 1.67 are considerably small. The Nyquist-Shannon criterion is fulfilled by suitable pixelsize a for sampling the PSF [Sha98]. With modern camera technology the noise contribution is reduced to incredible low values [And19][Ham19]. With a well aligned system, optimal imaging conditions and the brightest photo-switchable dye (Alexa Fluor 647) localisation precisions of 5 nm can be achieved.

1.6 Adaptive optics

The reader might have experienced adaptive optic elements already in daily life. As an example the car manufacturer BMW offers an *adaptive headlight* package, which tilts the headlights and therefore illumination area according to the steering speed and angle to better illuminate turns in the direction of travel [BMW18]. The use of the term *adaptive optics* may be misleading in this aspect. The origin of adaptive optics can be attributed to astronomy and the need for the development can be easily experienced by a look at the starry sky.

1.6.1 Twinkling Star

When observing a single star for longer period of time, the impression of twinkling may arise [Ell52]. This phenomenon is visualized in the schematic 1.19, where the starlight travels through several different layers in the atmosphere and the refracted light beams are imaged at different positions as shown in a highly magnified view. The deviation of the light is caused by atmospheric turbulences, namely fluctuations of air density which results in varying and therefore inhomogeneous refractive indices. These changes are commonly induced by temperature gradients, when different air volumes are mixed [SGDK07].

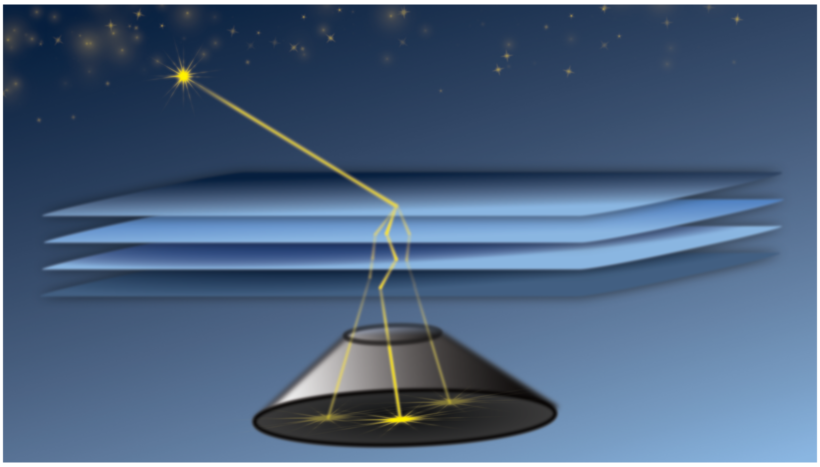

Fig. 1.19 Fluctuating density irregularities in the atmosphere layers cause beam deviation and impression of a twinkling star, visualized as magnified view in black cone. Inspired by tweet from user James O'Donoghue.

A viewer outside the atmosphere like the *Hubble space telescope* (fleight height 547 km [Gar15]) would not observe the described effect due to the lack of atmosphere.

1.6.2 Adaptive optics and microscopy

In the past sections numerous aberrations have been introduced which can be caused by optical elements. With careful adjustment and selection of corrected components, these aberrations can be reduced to a minimum. However, it may happen that the biological sample cancels out all efforts. For example, mismatching refractive index or dense tissue can induce strong scattering, absorption and aberration of light and leads to a strong degradation of image quality. With the help of flexible corrective optics - adaptive optics - these aberrations can largely be corrected and eliminated. In figure 1.20 this procedure is schematized. An ideal optical microscope system would turn a plane wavefront into a spherical wavefront (red lines). Scattering due to sample cause a distorted spherical wavefront, which can be restored by application of suitable optic devices.

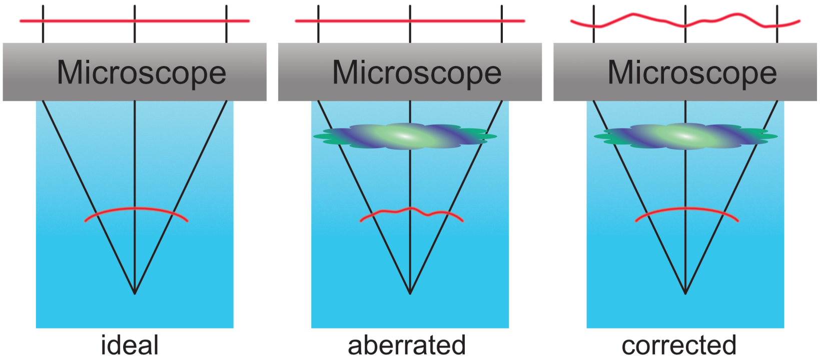

Fig. 1.20 Schematic for correction of induced aberrations. In the ideal case a planar wavefront (red top) would be imaged by the microscope as a spherical wavefront (red curve). Aberrations induced by the sample deform the spherical wave shape. With an adaptive optics device the ideal wavefront shape can be restored. Adapted from [Boo14].

This was impressively demonstrated, for example, with imaging inside living zebra fish embryos and other targets [LUM+18], [WMS+14]. The correction of the aberrations can be done by measuring the degraded wavefront with a Shack Hartman wavefront sensor. This is located in a feedback loop with a deformable mirror and allows the adjustment of the wavefront back to almost ideal flat shape.

1.6.3 Encoding the axial position

Nonetheless, aberrations can be induced in a targeted manner with the help of which valuable information can be obtained from the images. In the case of single molecule localization from chapter 1.5.3 , the 3D position can be obtained from the shape of the PSF. The easiest way to achieve this is to generate a controlled astigmatism. As shown in figure 1.7, the elliptical deformation of the imaging function correlates with an axial position. If one records the intensity distribution of an emitter in axial direction with a small step size and fits a Gaussian function with free parameters to these intensity distributions, the Z-position can be assigned on the basis of the varying FWHM. This calibration curve can be interpolated by C-spline or Gauss fits [PWH+14],[LMH+18]. The mentioned astigmatism can be generated by a cylindrical lens near a conjugated image plane or by wavefront deformation using a phase mask or deformable mirror. A phase mask or a spatial light modulator (SLM) can be used for complex PSF shapes like corkscrew [LLBM11], saddle-point [SSBM14], tetrapod , double-helix [BLB+13] or airy beam [JVZ14] based shapes. Using a stationary phase mask requires knowledge about calculation and etching and limits the flexibility in application. The use of an SLM on the other hand limits the photon budget as only one polarization state will be reflected. With an adaptive optic device like a deformable mirror great flexibility and fully reflection of the detected signal comes along. So additional corrections of sample-induced aberrations is possible almost on the fly and therefore this device is much more suitable for samples with variable refractive indices such as tissue as was demonstrated in [MCHB$^+$18].

Chapter 2

Material and Methods

The following chapter lists all materials and methods used to generate any data shown. The chapter is split into two parts, beginning with materials and followed by methods.

2.1 Materials

2.1.1 Inverted research high-end microscope Nikon TiE

The microscope body is an inverted Nikon Eclipse Ti (abbreviated as TiE) version 1. It has two side ports on the left and right side and a backport for adding detection or illumination pathways. The microscope is equipped with a fully adjustable transmission light arm located above the stage. Two tube lenses are inserted in the body and can be mechanically switched. The post magnification factors are 1x and 1.5x. A motorized XY-stage is installed with adjustable sample carrier holders and interchangeable inlets.

Objective turret

The objective turret is motorized and allows to switch objectives via software. All available objectives are listed in table 2.1. All immersion media objectives have a correction collar to adapt to the used coverslip thickness or allow correction to optimise the point-spread-function.

Filter turret

All filters inside the filter turret are mounted in high quality cubes, allowing slight alignment of the angular positions of inserted filters. The angle of the dichroics is painfully crucial as it determines the optical axis and therefore the position of the illumination area of given laser wavelength on the camera chip. All inserted filters are listed in table 2.2.

Table 2.1 Objectives used with all optical properties. All objectives are produced by Nikon.

type	magnification	numerical aperture	immersion medium	refractive index
CFI Plan Achromat	10	0.25	air	1
SR Plan APO IR	63	1.27	water	1.33
APO TIRF	100	1.49	immersion oil	1.52
SR HP Plan APO	100	1.35	silicon oil	1.4

Table 2.2 Filters installed in the filter turret of the TiE microscope.

description	ID	producer
dichroics		
zt405/488/561/640rpc flat	F73-410 T3	Chroma
zt 647 rdcxxr-xt	F43-649 SG	Chroma
zt 785 RDC	F48-785	Chroma
emission/rejection band filter		
ZET405/488/561/640	F57-405	Chroma
546SP	F37-548	Semrock

Perfect-Focus-System

An active focus stabilisation system termed *Perfect-Focus-System* (PFS) is implemented working with light in the infrared at 870 nm. This system actively moves the objective to counteract axial drift and maintain set focus position.

2.1.2 Rescanning Confocal Microscope imaging path

RCM unit

The Rescanning Confocal Microscopy (RCM) unit by the company *confocal.nl* from the Netherlands is a commercially available upgrade system to an existing inverted microscope body. The system is set up like a normal confocal microscope with a galvo scanner and a pinhole. Instead of placing a detector in the image plane after the pinhole, the detection path is extended and rescanned by a synchronized second galvo scanner. The image is written on an image array detector. The unit is attached to the microscope side-port with a C-mount adapter as well as the camera to the unit. Three supporting feet allow the levelling of the unit

Table 2.3 Pinhole size in Airy Units (AU) depending on objective magnification and numerical aperture (NA) @ 520 nm excitation wavelength. Data from manual provided by Confocal.nl.

magnification/NA	Pinhole size AU
100x/1.45	1.5
100x/1.25	1.3
60x/1.25	2.1

and aligning for correct positioning of the scanned beam. The fiber coupled laser is attached to an FC-APC connector at the rear of the housing. There the National Instrument Data Acquisition Card (NIDAQ) card is plugged in, the individual signal paths are internally split, looped through and made accessible at an external plug in board. Five connectors for analog and digital signal transmission are accessible, four of each are for triggering the laser lines. The remaining two are for camera triggering, here the digital pin is used. The connector type is SMD.

The physical diameter of the pinhole is $50\mu m$ according to the manual of the device. The manual also lists the pinhole expressed in airy units (AU) depending on magnification and numerical aperture at a given wavelength. The values are listed in table 2.3 only showing the closest match with objectives used in our case (see table 2.1).

Laser system

Laser excitation source for the RCM unit is a multi line laser-system *Skyra*™ (Cobolt). Specifications of the laser is listed in table 2.4 with laserline, nominal output power, maximal output-power at fiber end as well as coupling efficiency. The laser module was bought as a prototype. The maximal output power was determined by analog voltage to prevent over heating the laser module. Output power after fiber coupling was measured at the end of the fiber and resulting coupling efficiency calculated.

Table 2.4 Specifications of multi line laser system *Skyra™*. *Set maximal output power* determined by analog voltage.

wavelength [nm]	nominal output power [mW]	set maximal output power [mW]	output power fiber end [mW]	coupling efficiency [%]
405	50	48.5	10	21
488	50	49	17	35
561	50	46	29.8	65
640	50	46	17	37

Table 2.5 Devices and parts in RCM imaging parts with description, product numbers and supplier.

RCM		
RCM unit	AA0001	confocal.nl
dichroic 408/488/561/640		
emission bands 421-480/502/552/574-624/656-800		
laser		
Skyra fibercoupled	90420	Cobolt
ML-561/638/488/405, 50+50+50+50mW		
camera		
Zyla 4.2P USB	Zyla-4.2P-USB	Andor
optomechanic parts		
dual position slider	ELL6K	Thorlabs
absorptive neutral density ND1	NE10A-A	Thorlabs

2.1.3 Single molecule detection path

Lasers

The lasers used are listed in table 2.6. All lasers are aligned onto the optical axis of the TIRF/HILO illumination system using adjustable mirror-LaserMUX pairs.

Table 2.6 Installed laser lines with manufacturer and output power for widefield illumination.

wavelength [nm]	type	supplier	output power [mW]
405	iBeamSmart 405-S-LP	Toptica	100
488	iBeamSmart 488-S-HP	Toptica	200
532	gem 532	Laserquantum	500
640	iBeamSmart 640-S-HP	Toptica	200
785	iBeamSmart 785-S	Toptica	125

Excitation path

To achieve various illumination types depending on the imaging modality a flexible beam expanding system capable of switching between EPI-HILO-TIRF illumination modes has been custom designed. The beam expander allows to flip in various lenses in order to increase the illuminated area and therefore the power density required for *d*STORM imaging modalities. The excitation beam is couppled into the backport of the microscope, all optomechanic parts used are listed in table 2.7.

Table 2.7 Optomechanical parts and filters in excitation path.

lenses		
Achromat VIS ∅50mm f=120mm	G322303000	Quioptic
Achromat ∅1/2", f=25mm	AC127-019-A-ML	Thorlabs
Achromat Doublet ∅=8mm, f=10mm	AC080-010-A-ML	Thorlabs
mirrors and filters		
Broadband dielectric mirrors ∅2"/1"	BB2-E01/2	Thorlabs
Clean-up 405/10 MaxDiode	F94-405	Semrock
Clean-up ZET 488/10	F49-488	Chroma
Clean-up ZET 532/10	F49-532	Chroma
Clean-up 644/12 H	F49-644	Chroma
Clean-up 785/10 MaxDiode	F94-782	Semrock
LaserMux 375-405R	F38-M01	Semrock
LaserMux 503nm edge	LM01-503-25	X Semrock
LaserMux 514-543R	F38-M04	Semrock
Polarizing Beamsplitter Cube	CCM1-PBS251	Thorlabs
Round Variable ND filter	NDC-100C-4	Thorlabs
mechanical parts		
Kinematic Mirror Mount 60mm	KCB2/M	Thorlabs
Flip mounts	FM90/M	Thorlabs
Rail system	S 40-400-LL	Owis
XY Adjusting Mounts	OH 40-D25-FGS-XY	Owis
XY Adjusting Mounts	OH 65-D56-FGS-XY	Owis

Deformable mirror

In order to actively modify the PSF a deformable mirror DMP40 (Thorlabs) has been placed in the fourier plane of the relay system. The relay system has an additional magnification factor of 2. Due to limited space the detection beam was reflected by a full mirror onto the deformable mirror directly after the first lens (see figure B.1 B, Appendix B). In table 2.8 relevant technical specifications of the deformable mirror are listed. All parts used for setting up the detection path are listed in table 2.9.

Table 2.8 Installed deformable mirror DMP40 (Thorlabs) with relevant technical specifications.

description	specification
Actuators	40
Coating	protected silver
Average reflectance	> 97.5% (450nm-2µm)
Segment voltage range	0 to +200V

Table 2.9 Optomechanical parts and filters and camera used in the single molecule detection path.

lenses		
Achromatic Doublet ⌀2" f=150mm	AC508-150-A	Thorlabs
Achromatic Doublet ⌀2" f=200mm	AC508-200-A	Thorlabs
Achromatic Doublet ⌀2" f=400mm	AC508-400-A	Thorlabs
mirrors		
Deformable Mirror	DMP40/M-P01	Thorlabs
Dielectric Broadband Mirror	BB2-E02	Thorlabs
mechanical parts		
XY Translator 60mm	CXY2	Thorlabs
Removable Filter Holder	LCFH1/M	Thorlabs
filters		
647 LP Edge Basic	F76-649	Semrock
525/50 ET	F47-525	Chroma
700/75 ET	F47-700	Chroma
ZET785-NF	F40-786	Chroma
camera		
sCMOS SONA 4.2B-11	SONA 4B-V11	Andor/AcalBF

2.2 Methods

In this section, all buffers used are listed first, followed by the methods and protocols used.

2.2.1 Buffers

Table 2.10 Buffers, dyes and antibodies used for sample preparation

	buffer components & reagents	
cytoskeleton buffer (CB)	10mM MES pH 6.1, 150mM NaCl, 5mM EGTA, 5mM glucose, 5mM $MgCl_2$	
fixation actin skeleton	4% FA in PBS, 0.1% Triton X-100	
fixation tubulin		
prefixation&permeabilisation	0.3% GA, 0.25% Triton X-100 in CB	
fixation	2% GA in CB	
jetPRIME®transfection reagent	114-01	Polyplus
	switching buffer	
reducing agent	100mM MEA (β-mercaptoethylamine), pH 7.4	
oxygen scavenger	4% glucose, 4U/ml glucose oxidase, 80U/ml catalase	
	antibodies	
α-tubulin, host rabbit	PA5-19489	ThermoFisher
F(ab')2 goat-anti-rabbit IgG (H+L) Alexa Fluor™ 647	A21246	ThermoFisher
	dyes & stainings	
TetraSpeck™ Microspheres, 0.1µm fluorescent blue/green/orange/dark red	T7279	ThermoFisher
Fluoresbrite® YG Microspheres 0.1µm	17150-10	Polysciences, Inc.
CellMask™ Green Plasma Membrane Stain	C37608	ThermoFisher
MitoTracker™ Green	M7514	ThermoFisher
Alexa Fluor™ 647 Phalloidin	A22287	ThermoFisher
Alexa Fluor™ 488 Phalloidin	A12379	ThermoFisher
ATTO 565 Phalloidin	AD 564-81	ATTO-TEC
DyLight™ 650 Phalloidin	21838	ThermoFisher
SeTau-647-NHS	K9-4149	SETA BioMedicals
Hoechst 33342	H1399	ThermoFisher
	plasmids	
EB3-tdTomato	50708	Addgene

2.2.2 Fixation and staining

Depending on the structure to be stained, the fixation of the cells was performed according to established protocols such as given in [vLK^{+}11b] or [The14b].

Actin skeleton

For optimal preservation of the actin fine structure, cells were incubated with prewarmed formaldehyde (4% in cytoskeleton buffer) for 10 minutes at 37°C. The staining solution containing the phalloidin dye compound (in 1% BSA) should be kept ready. After the incubation period of the fixation has expired, the sample is once rinsed with 1x PBS and then the staining solution is added. With dilutions of the phalloidin stock concentration (6.6 µM) of 1:100, measurements can be performed after 1 h incubation. For lower dilutions an incubation at 4°C over night is recommended. Staining should take place immediately after fixation, as the fine meshwork is degraded in a short time and is stabilized by the phalloidin. [SRHA99].

Microtubule filaments

Staining of tubulin filaments has been optimized in several publications [vLK^{+}11b], [WB15] and [JFL19]. To reduce unspecific staining of cytosolic tubulin a two step fixation procedure is recommended. For this purpose, cells are permeabilized for 1-2 minutes with a prewarmed buffer (37°C) and simultaneously pre-fixed. This buffer contains 0.3% glutaraldehyde and 0.25% Triton X-100 (in CB). The buffer is then exchanged for preheated (37°C) 2% glutaraldehyde (in CB) and incubated for 10 minutes. The last two steps are performed at 37 °C as best as possible. The fixation procedure is stopped by 100mM glycine (in PBS) step for 5 minutes. Cells are washed at least 3 times 5 minutes with PBS. Background reduction can be improved by a reducing step with incubation of 0.1% (w/v) sodium borohydrate ($NaBH_4$) for 7 minutes. Cells are washed again at least 3 times 5 minutes with PBS. Blocking of epitopes inducing unspecific labeling is carried out by 30 minutes incubation with 5% BSA (bovine serum albumin). Primary antibody can be added at concentrations of 10µg/ml (in 5% BSA) for 60 minutes at room temperature. Removal of unspecifically bound primary antibody can be achieved by rinsing the sample several times with 0.05% Tween20 (in PBS) solution. This step should be followed by washing with normal PBS for 3 times 5 minutes. Secondary antibody is added at concentrations of 10µg/ml in 5% BSA for at least 60 minutes at room temperature. Washing steps with tween solution and PBS are applied as described above. In order to maintain the labeling of both antibodies a post fixation step with 4% formaldehyde (in PBS) for 10 minutes can be performed. Sample is washed several times with PBS and can be imaged or prepared with 0.02% sodium azide (NaN_3) for long term storage.

Transient Transfection

Transfection is carried out with the transfection reagent JetPrime (Polypus). All steps were carried out according to the recommendation of the manufacturer. DNA amount per sample chamber was set to 500 ng of the chosen plasmid. Medium has been changed after 8-10 h with fresh cell growth medium.

Bead Samples

TetraSpecks were diluted in PBS in a ratio of 1:1000 and pipetted into the wells. Over time, the beads settle on the bottom of the sample chamber. If the density is sufficient, the medium is carefully exchanged for pure PBS with 0.1% sodium azide. To avoid complete evaporation of the medium over time, the sample chamber can be sealed airtight with Parafilm® (VWR).

Polyscience YG beads are diluted in distilled water at 1:1000 or higher. Droplets are pipetted onto cleaned coverslips and stored until water was entirely evaporated. Moviol droplets were added onto microscope slides and prepared bead coverslips flipped and dropped carefully on top of the moviol droplets. After several hours of drying slides are ready for imaging.

2.3 Software

Different software for device control and analysis have been used in this thesis. For commercial software all licences are owned by the department of Biotechnology&Biophysics. The following list in alphabetical order contains all used software including version numbers.

NIS Elements (Nikon) 5.11.01 build 1367

Cobolt Monitor (cobolt) 6.0.7.0 Control software for Cobolt multiline laser Skyra

Thorlabs Deformable Mirror (Thorlabs) - control software for setting mirror patterns, version 2.4

TopControl (Toptica) V1.026 - Control software for iBeamSmart laser modules

Topas iBeam Smart (Toptica) -Control software for iBeamSmart laser modules

Matlab (MathWorks) R2018a - software for numerical calculations

description

FIJI (open source) - image processing software

ThunderSTORM ImageJ plugin for single molecule localisation analysis [OKB$^+$14]

SMAP Single molecule analysis software developed by Jonas Ries [LMH$^+$18]

rapidSTORM single molecule analysis software developed by Steve Wolter [WLH$^+$12]

ZOLA 3D software package for 3D localization analysis, ImageJ plugin with GPU processing [ALRZ18]

Origin Pro 2017 (Originlab) - statistic analysis software

Imaris 8.4 (Bitplane) - 3/4D Image visualization and analysis software

LLS-tools Script collection for data conversion and processing by Felix Wäldchen

Python3 (open source) for analyis including Surepy package written by Sören Doose

Affinity Designer (Affinity Serif) - Vector design software used for figures and schematics

Citavi 6 (Swiss Academic Software) - database and library catalog software

Labview 2017 (National Instruments) - development environment

TeXstudio 2.12.16 LaTeX editor

GraphPad PRISM (GraphPad Software) - statistic software

2.4 Hardware configuration

Imaging and analysis has been performed with hardware listed in 2.11.

Table 2.11 Hardware used for imaging and analysis.

CPU	Intel(R) Core(TM) i7-8700K @
GPU	NVIDIA GeForce RTX 2080 Ti
RAM	4x 16GB Corsair Vengeance DDR4
SSD I	EVO 960 500GB
SSD II	EVO 860 1TB
HDD	WD Blue 4TB
NIDAQ	PCI-6733

Chapter 3

Results and Discussion

The aim of this thesis was to build an imaging system that allows to observe dynamic processes in a cell as well as to obtain highest structural information. Since no commercially available device meets all requirements, several imaging techniques were combined to cover the experimental requirements. The unique strength of this system is based on the comprehensive analysis of a process such as the dynamics of expression of a fluorescent protein and its spatial localization in a nanoscopic environment.

3.1 The microscope setup

The original idea for this PhD project was to set up an image scanning based microscopy system in the first place. During the time of exploring required parts and devices for an image scanning system the Rescan Confocal Microscopy (RCM) unit from *confocal.nl* was announced on the microscopy market. Being highly affordable and offering enhanced technical specifications the choice was made to use the commercially available system. The RCM was integrated to an inverted high end microscope from Nikon. Furthermore an excitation and detection path for single molecule localisation was set up and upgraded with an adaptive optics device later on. A microfluidic pump system has been installed to interact with the sample on the microscope stage. In the following sections, the individual techniques are characterized with regard to resolution, influence of photo damage and sensitivity. In addition, basic experiments of the microfluidic pump are described. This preliminary work is essential for the realisation of a final experiment, which includes live cell imaging, live fixation and staining as well as a super-resolved single molecule localisation microscopy on one and the same structure of a cell.

3.2 Rescan Confocal Microscope unit - RCM

The RCM based on the image scanning principle described in 1.5.2 combines the advantages of a conventional confocal, with improved resolution and highly sensitive detection. As an add-on for existing microscope systems, adaptation for seamless integration and operation is necessary. The excitation parameters are characterised as well as resolution enhancement and wavelength dependency. Furthermore a comparison between conventional confocal scanning mode as well as rescanning mode was carried out and evaluated.

3.2.1 Integration of external laser system

The multiline laser system Skyara (Cobolt) has been chosen as excitation source for the RCM.

Fiber Connector

When coupling the Skyra with the provided fiber to the RCM unit, various problems were identified. The axial view of the PSF of a 100nm tetraspeck (acquired @488nm) in figure 3.1 has a double intensity accumulation shaped like an hour glass. The origin of the phenomenon lies in the collimation of the excitation laser.
In a well aligned system the excitation focus of the fiber and the detection focus of the pinhole are brought to coincidence. In case of a misaligned system both focus spots are displaced in axial direction. The displacement is represented by the intensity distribution not accumulated in a single spot as to be expected by a single fluorescent bead. The mentioned misalignment could be caused easily by a non collimated excitation laser.
The system has been tested before with a laser (LuxX®488, fiber coupled single mode) kindly provided by Omikron. The same fiber type with FC-APC connector has been attached as with the Skyra. The fiber connector APC - short for *angled physical contact* - is designed for minimizing the back reflection into the fiber and laser diode by an inclined contact surface. These fiber connector type is widely used and produced in two variants:

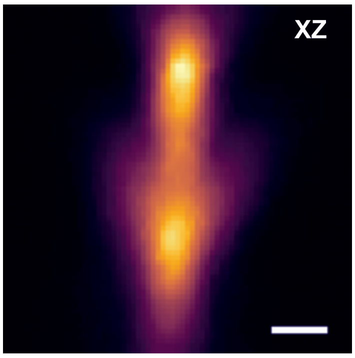

Fig. 3.1 PSF of 100nm TetraSpeck bead acquired with wrong fiber connector type. Scalebar 500nm.

- type N - narrow key width
- type R - reduced key width

The dimensions for both key and connector depending on the type are listed in table 3.1 and only show relative small differences in size. Exactly these difference connector and key type lead to a non collimated beam when mismatching. By changing the fiber of the Skyra to an FC -type R the excitation was collimated again and the axial PSF turned back to the expected shape as shown later in section 3.3.

Table 3.1 Width of key and connector depending on type. Data from [AFW19].

Connector Type	Key width [mm]	Connector width [mm]
FC - Type R	2.02	2.02
FC - Type N	2.14	2.10-2.14

Excitation artefacts induced by 561nm DPSS line of Skyra

The multi line laser system Skyra is equipped with the most common laser wavelengths in fluorescent imaging. Three wavelengths 405nm, 488nm and 640nm are based on diode laser system, the 561nm laser however is a diode pumped solid state laser (DPSS). All laser lines can be triggered with analog as well as digital signals. Analog triggering controls the output laser power, digital triggering the ON-OFF switching of the laser lines during the line scans. For all laser lines the analog-digital triggering works well, except the 561nm laser line. In the images acquired with the 561nm laser line a blank area at the left image border was visible (see figure 3.2). The blank space is located at the side of image where each line scan starts. With increasing excitation power the blank area decreased as can be seen in figure 3.2. To quantify the decrease the distance of image border to fluorescence area was measured, indicated by the double headed arrow and plotted against the excitation power. The distance of no excitation by the laser dropped from around 7.4 µm to 2.4 µm. As the curve implies the decrease of unilluminated area saturates at laser powers above 100 µW. The minimal achieved distance can be converted to an OFF-time via

$$\frac{\text{distance}}{\text{pixelsize}} \cdot \text{dwelltime} = \frac{2.4\mu m}{0.043\mu m} \cdot 2.4\mu s = 133\mu s. \tag{3.1}$$

The rise time for the built in diode pumped laser (DPL) is in the range of 60µs according to the manufacturer manual. The off-time and therefore unilluminated area could not be further decreased. To eliminate the existing problem I simply applied two countermeasures:

1. permanent crop of field of view, excluding the unilluminated image area
2. insert optical density (OD) filter to excitation path

The first step is a logical consequence and can be implemented in the software settings. As the unilluminated area under optimised conditions corresponds to only $\sim$3% of the total image area it can be neglected.

The second implementation is a benefit to the performance of all laser lines. The power voltage response curves shown in figure 3.3 accounts for all wavelength. Fluorescent samples whether living cells or fixed samples in general are prone to photobleaching or photo induced damage. The lower the excitation light dose the better, given sufficient signal to noise ratio. Excitation power levels for the RCM turned out to lie in the range of several 100 µW, mostly between 30-100 µW.

To achieve these low values of excitation power very low voltage levels have to be applied, which brings high instability of power levels along. Additionally the response curve is quite flat in this area, enhancing the uncertainty of the set power level. Figure 3.3 C shows a zoom in into the boxed region of B. Attention should be paid to the differently displayed magnitude of power. In order to stay in the lower region of excitation power few changes of few mV have to be handled. This is usually no challenge for modern electronics, but critical close to the turn on threshold. Introducing therefore an optical density filter (OD) shifts the required voltages far away from the threshold and increases excitation power of several orders of magnitude. An OD filter has been placed inside the RCM unit directly behind the collimator, mounted on a dual-position slider (Thorlabs) switchable with a custom written GUI in LabView. The OD filter is absorptive and has an optical density of 1, allowing therefore an attenuation of the excitation power of 10-fold.

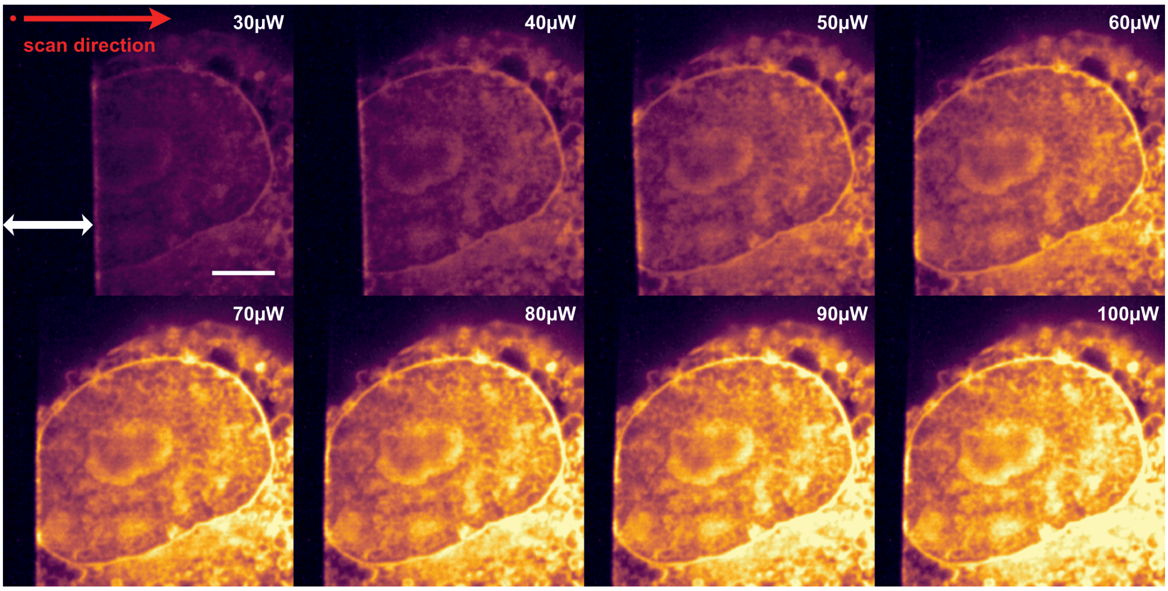

Fig. 3.2 Fluorescent sample acquired with 561 nm excitation. Visible illumination artefacts at the left border of the images are reduced with increasing laserpower ranging from 30 µm to 100 µm. Linescan direction is indicated by red arrow and starts in the top left corner in each image. Scan mode is unidirectional. Double white arrow indicates the off-distance of the 561nm DPSS line at the beginning of each line scan. Scalebar 5µm.

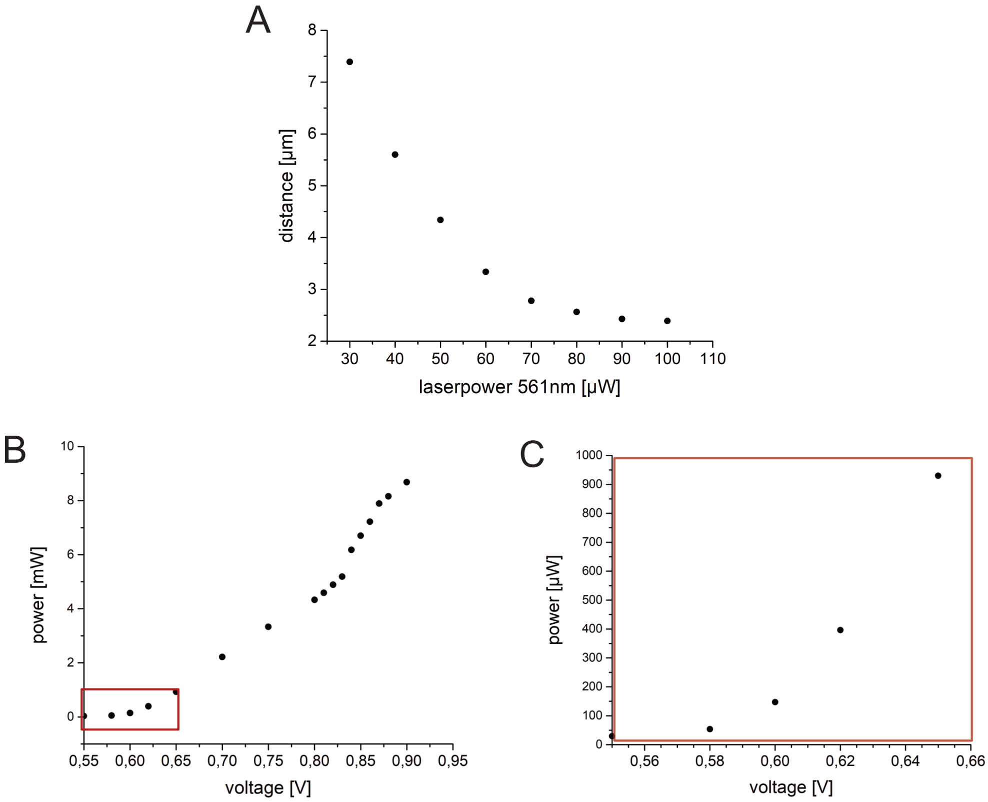

Fig. 3.3 **A** turn-on delay distance from image border to excitation turn-on as a function of excitation power of the 561nm Laser line. **B** Measured power-voltage response curve of Skyra 561nm line. Red-boxed region is displayed in **C** as zoom-in. Note the changed magnitude of power unit.

Cross-excitation of 488 nm laser line

Fluorescent proteins and synthetic dyes in general have quite broad absorption and emission spectra (see figure 3.4 panel E). When staining multiple targets with different fluorescent markers overlapping spectra are mostly unavoidable. The right filter choice in the detection path is inevitable. Data bases have been provided online, where spectral properties of fluorophores, filters and light sources can be combined and visualized. Powerful tools are

> **fpbase.org** - open access powerful database with various additional information and interactive visualisation, created and designed by Talley Lambert (Harvard Medical School).
>
> **Spectra Viewer** - open access online filter and fluorophore database with visualisation, provided by Chroma®
>
> **SearchLight™** - open access online filter and fluorophore database with visualisation, powered by Semrock®

Filtering of emission light might be necessary, if the laser excitation wavelength is not only absorbed by the fluorescent dye A of interest but to a certain amount as well by an additional dye B. Although inefficiently excited the dye B might have a strong emission and overlap the structure of interest labelled with dye A. The most convenient way to insert filters in order to block this interfering emission in the detection path is in sections with parallel ray geometry, as this avoids alteration of the detection path and imaging dust lying on the filter surface. In the confocal detection light path the only possible position is already occupied by a quad band rejection filter to block back reflected laser light from being forwarded to the camera chip. In order to minimize cross excitation the only way to place a filter is in the excitation path, in the filter turret directly below the objective. The filter therefore has to be a shortpass, to transmit the excitation wavelength of the desired channel to the sample and block longer wavelengths from absorption spectra of channels with higher wavelengths. The cross excitation is mostly visible in the combination of 488 nm and 561 nm channel as can be seen in figure 3.4. Here the mitochondria of a 3T3 fibroblast cell have been stained live with MitoTracker™ Green, after fixation the actin skeleton has additionally been stained with phalloidin Alexa Fluor 555. Panel A shows the actin skeleton acquired with the 561nm laser line, panel B the mitochondria staining imaged with 488nm. The cross excitation of the actin staining is clearly visible. To avoid the crosstalk the shortpass filter SP546 is inserted during the acquisition of the 488 nm channel as can be seen in panel C. Here only the mitochondria are visible as the shortpass filter blocks emission of the Alexa Fluor 555 dye. Panel D visualizes the crosstalk, indicated by a color code according to the displayed

error bar.
Avoiding crosstalk is definitely desired, but one has to keep the minor drawback in mind. In panel E all involved spectra are displayed, both absorption and emission spectra of a commonly used dye combination (Alexa Fluor 488 and 555), the 488nm laserline and the transmission spectra of the shortpass filter SP546. Imaging with the shortpass filter does not only block the emission of the Alexa Fluor 555 dye, but also cuts the emission of the Alexa Fluor 488 dye. To quantify the loss of intensity one has to integrate over the entire emission spectra of Alexa Fluor 488 and the cut spectrum (emission spectra convolved with the shortpass transmission). Using the shortpass filter when imaging reduces the detected emission by around 33% in comparison to acquiring the entire emission. Excitation intensities might therefore have to be increased to obtain sufficient signal, entailing increased photobleaching and phototoxicity. Furthermore inserting the filter cube adds a minimal delay when acquiring multichannel image sequences. The delay can be neglected in most case, with highly dynamic processes this drawback will definitely increase the already present time shift between mentioned channels to a certain amount.

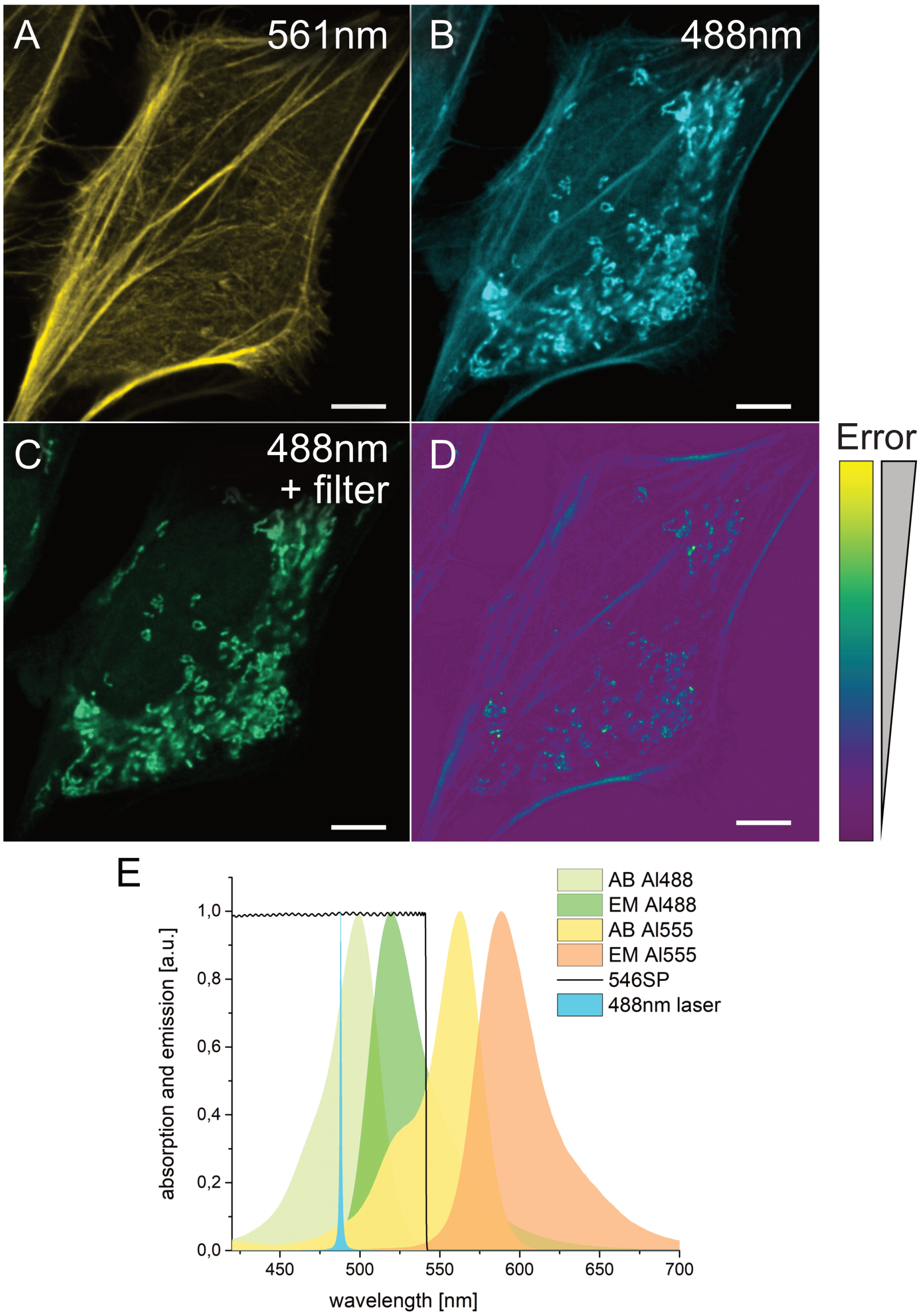

Fig. 3.4 Cross talk of 488nm and 561nm channel in the RCM system visualized by staining actin with phalloidin Alexa Fluor 555 and Mitochondria with MitoTracker™ Green. **A** Phalloidin Alexa Fluor 555 imaged with 561 nm laser line. **B** MitoTracker™ Green imaged with 488 nm laser line, actin filaments strongly visible. **C** Shortpass 546 introduced to detection path when imaging in the 488 nm channel blocks crosstalk from Alexa Fluor 555. **D** Error map visualizing the crosstalk between 488 nm and 561 nm channel separately shown in B and C. Error correlating to the displayed color-bar. Scale bars 5 µm. **E** Overview of involved spectral contributions. Absorption and emission spectra of Alexa Fluor 488 and 555, the transmission spectrum of the shortpass filter SP546 and the 488 nm laserline.

Power calibration

Power calibration has been performed as described below.

1. find voltage for high limit of output power
2. measure free beam power at high voltage limit
3. fiber coupling with maximizing the output power at the fiber end
4. find voltage threshold for turn-on of laser lines
5. run voltage ramp and measure corresponding output power levels above objective

Calibration can be integrated in NIS elements software and output power is displayed then in mW.

3.3 Resolution Enhancement

Based on the image scanning principle the RCM counts as a super resolution imaging technique. According to the supplier the system gains a 1.4 fold lateral resolution improvement as compared to widefield imaging. Measurement of sub diffraction fluorescent beads at 488 nm excitation results in ~170 nm FWHM. In the following sections the resolution enhancement is verified by measuring the PSF as function of the used excitation and emission wavelengths. Measurements have been performed using sub diffraction beads and a biological structure in a stained cell that exhibits structural features with a size smaller than the diffraction limit.

Resolution Enhancement Rescanning vs Confocal Mode

The resolution enhancement is analysed by direct comparison of the Rescanning and Confocal imaging mode of the system. Point spread functions were acquired with 100 nm yellow-green fluorescent beads from *Polyscience* embedded in moviol using an APO TIRF 100x/1.49 oil immersion objective. The scanning mode was set to *rescanning* and a z-stack with 100 nm steps was recorded. The same bead was also acquired in scanning mode *confocal* directly after the acquisition in rescanning mode.

For analysis of the lateral extensions the frame with best focussed intensity pattern was taken and a gaussian function fitted to the intensity distribution. For axial analysis the z-stack was converted to orthogonal view and analysed as described before. Point-spread-functions in lateral (XY) and representative axial (XZ) view of the rescanning mode are shown in figure 3.5 A and B, corresponding line profiles are displayed to the right. The

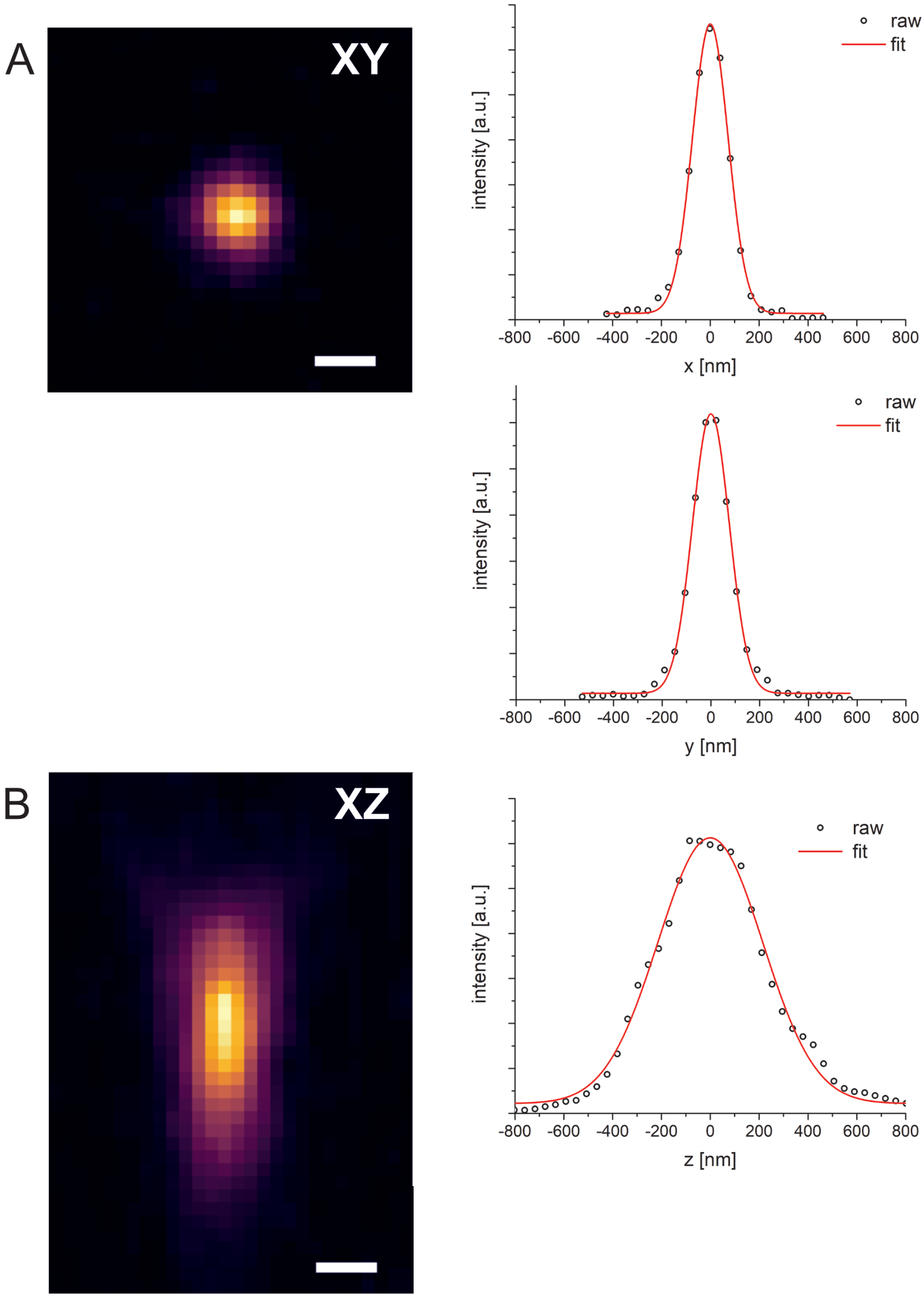

Fig. 3.5 Point-Spread-functions of 100 nm bead acquired in RCM mode with 488 nm excitation wavelength. **A** Lateral PSF with raw data and gaussian fit. **B** axial PSF with raw data and gaussian fit. Scale bars 200 nm.

direct comparison of the rescanning and normal confocal mode is only shown in lateral view (XY) in figure 3.6 A. The better confined intensity distribution in the rescanning mode can be observed directly. It should be mentioned that the pixel size differs by a factor of 2, a logical consequence of introducing an opto mechanical magnification factor of 2 in the rescanning mode. The rescanning mode has a pixel size of 43 nm, the confocal mode 86 nm. The direct comparison of both imaging modes is visualized by normalize lateral and axial line profiles in figure 3.6 B. Although the confinement might seem marginal, it might have substantial relevance for resolving certain structures. In table 3.2 FWHM values are listed for both scanning modes including the improvement ratio. The measured values indicate almost similar resolution of ~170nm (@488nm excitation) in lateral dimensions and are in accordance to the technical specifications. Concerning the axial resolution the manual of confocal.nl states 750nm FWHM @520nm emission maximum, measured probably with a 100x/1.45 oil objective. Measurements of axial resolution in our system results in FWHM of 506nm (rescanning mode) and therefore in an almost 1.4 fold better confined PSF than the manufacturer specifications. As the same beads are used for calibration, the main difference is the used objective. As lateral resolution scales with $1/NA^2$, the slightly higher NA of 1.49 of our 100x Apo TIRF objective has a solid contribution to the axial resolution improvement. Within our system the improvement of axial resolution from confocal to rescanning mode is only 10%, while being about 3x lower than the corresponding lateral resolution.

Table 3.2 Resolution Comparison RCM-Confocal-mode

Axis	RCM mode	Confocal mode	improvement
	FWHM [nm]		
x	172 ± 3	240 ± 4	1.4
y	178 ± 3	244 ± 4	1.4
z	506 ± 11	560 ± 18	1.1

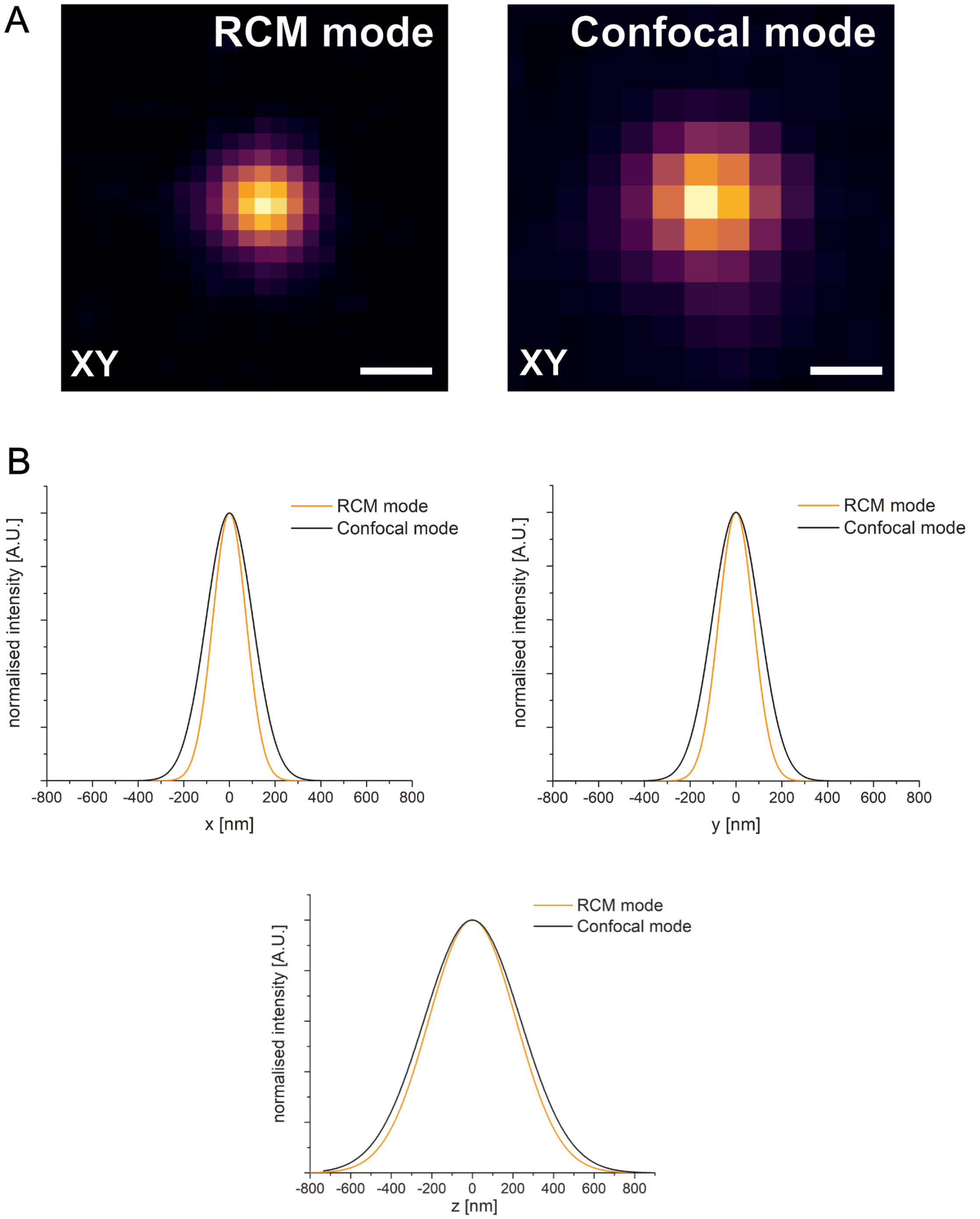

Fig. 3.6 **A** Improvement of PSF in RCM mode (left) and confocal mode (right). Scale bar 200 nm. **B** comparison of fitted normalised line profiles in lateral (x,y) and axial direction.

Resolution depending on excitation wavelength

As resolution depends on the emitted wavelength resolution enhancement was tested by acquisition of the PSF using 488 nm, 561 nm and 640 nm excitation wavelength. The 100 nm tetraspeck bead is fluorescent in all mentioned wavelengths but hardly in the UV range. To avoid any possible influence of axial drift during the acquisition the order of acquisition was set to wavelength channel per z-step, meaning all three wavelengths were acquired sequentially before moving to the next focal plane. In order to simulate real acquisition settings, the shortpass filter was used for imaging the 488 nm channel. Lateral line profiles with gaussian fits for all three channels are plotted in figure 3.7. In table 3.3 the estimated values for lateral and axial FWHMs gained by gaussian fits are listed with their fit error. The lateral FWHM is calculated of the mean of x and y FWHM. The lateral FWHM for 488 nm excitation is in good accordance with data in section 3.3. With increasing excitation wavelength the FWHM shows a clear linear increase but is at any time below the FWHM values of the confocal listed in table 3.2.

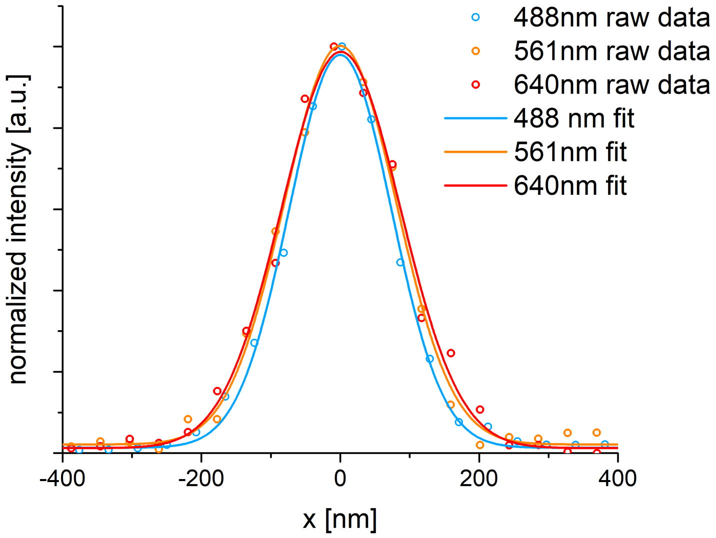

Fig. 3.7 Lateral line profiles of 100 nm Tetraspeck bead excited with 488 nm, 561 nm and 640 nm in RCM mode. Normalized raw data and gaussian fit.

Concerning the values of axial FWHM there seems to be a discrepancy according to mentioned table before. The values might indicate a far better confinement of the PSF in axial direction than the data acquired before. The difference originates of the fluorescent sphere. Tetraspecks are easily saturated in the center of the enveloping sphere especially with point scanning illumination. It was carefully checked that bead images were not reaching intensity saturation since this would artificially broaden the PSF.

Table 3.3 FWHM lateral and axial dependency on excitation wavelength. Errors represent standard error from fit.

Excitation wavelength [nm]	FWHM lateral [nm]	FWHM axial [nm]
488	173 ± 3	420 ± 4
561	190 ± 4	445 ± 5
640	201 ± 5	526 ± 9

Axial shift depending on excitation wavelength

When performing bead based experiments non overlapping axial PSFs for multichannel experiments were observed. Although a high performance objective with outstanding correction for chromatic aberrations was used (APO TIRF, 100x, 1.49) the same fluorescent bead was imaged in focal planes several 100 nm apart depending on the emission spectra. Figure 3.8 shows in the top panel the axial (XZ) view of the PSF in all three channels (488 nm, 561 nm, 640 nm). A distinct axial shift with increasing emission wavelength is clearly visible. The bottom panel displays the axial lineprofiles of each PSF with gaussian fits to the raw data. The estimated center of the gaussian fit and therefore the amount of axial shift is listed in table 3.4 with the 640nm channel as reference. The center of the PSF is shifted accordingly -178 nm for 561 nm excitation and -352 m for 488 nm excitation. To avoid influence of axial drift of the imaged focal plane, channels were acquired sequentially before the next z-interval step. For imaging the 488 nm without cross excitation of orange fluorophores, the shortpass filter has been inserted. The shift is not introduced due to the filter, as it is occurring as well in the 561nm channel without any filter. It is unlikely that the APO TIRF objective causes this amount of chromatic aberration. The components of the RCM unit consist mainly of Thorlabs parts, as Thorlabs only offers achromatic lenses it might be reasonable to assume the shift originating from the detection path of the RCM unit.

Table 3.4 Axial shift of PSFs depending on excitation wavelength. Errors represent standard error from fit. Error for 640 nm excitation relative to center of fit @640 nm.

Excitation wavelength [nm]	axial shift [nm]
640	0±3
561	178±2
488	352±2

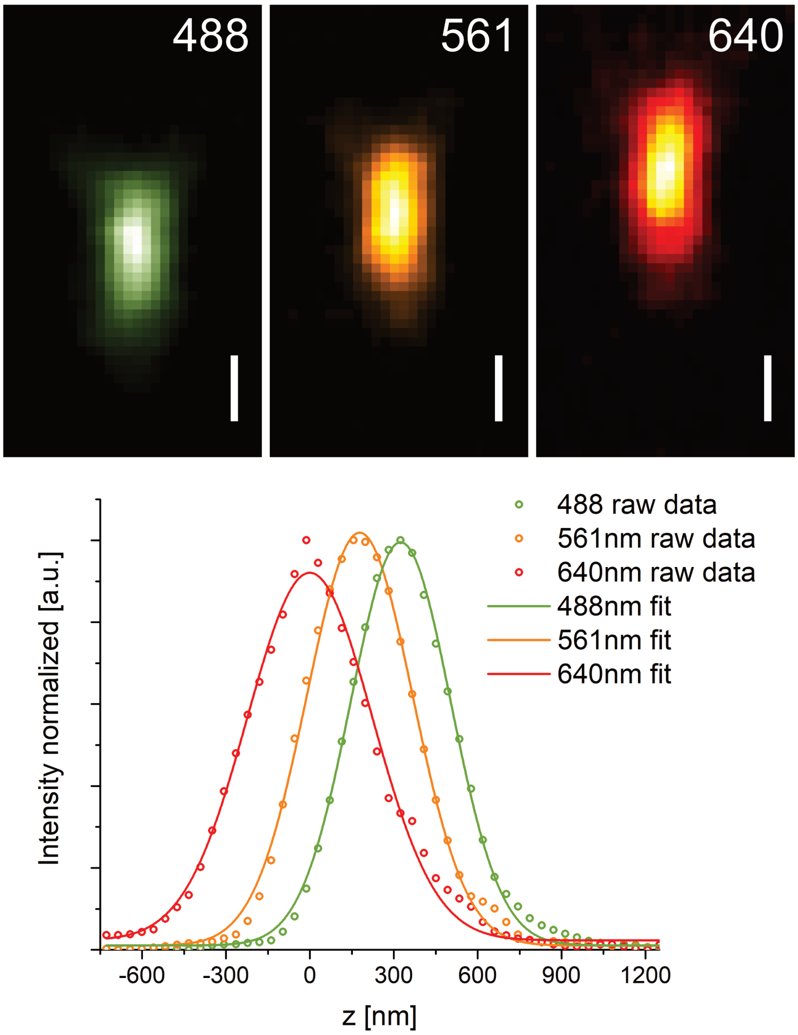

Fig. 3.8 Top XZ views of the same 100 nm Tetraspeck bead acquired in the wavelengths 488 nm, 561 nm and 640 nm. Scale bar 300 nm. **Bottom** Axial shift of estimated center of the gaussian fit to the XZ lineprofile for each excitation wavelength.

Focal Offset in control software *NIS Elements*

The focal offset can be directly set in the ND acquisition tab for the wavelength channels (called in NIS-Elements *lambda*). A reference channel should be chosen and then the corresponding offset in µm for each wavelength channel entered. According to table 3.4 the entries were set and a sequential z-stack of 100 nm Tetraspecks was acquired. Z-step intervals were set to 100 nm and the shortpass filter was used when acquiring the 488 nm channel to prevent bleed through of fluorescent emission of excited *orange* fluorophores. In the top panel of figure 3.9 the orthogonal view (representative here only XZ) for a 100 nm tetraspeck bead PSF is displayed acquired with 488 nm (shortpass filter), 561 nm and 640 nm excitation wavelength using the focal offset correction values estimated in the section before. The bottom panel contains the axial line profile plots with raw data (circles) and gaussian fits to the data. A slight displacement of the resulting curves is remaining, a quantitative analysis reveals the offset values of the PSF center to the reference PSF (@640 nm) which are listed in table 3.5. Axial PSFs in the channels 488 nm and 640 nm are perfectly overlapping. The displacement of 50 nm in the 561nm channel in reference to 488 nm seems to be correlated to the objective z-step intervals. With a minimal z-step size of 30 nm the offset correction of the 561 nm channel with $\approx$ 170 nm results in integer multiples of the step size, therefore the set value can not be applied by the software. With a deviation of 10% between the axial PSF FWHM the error in focal offset can be neglected for this channel.

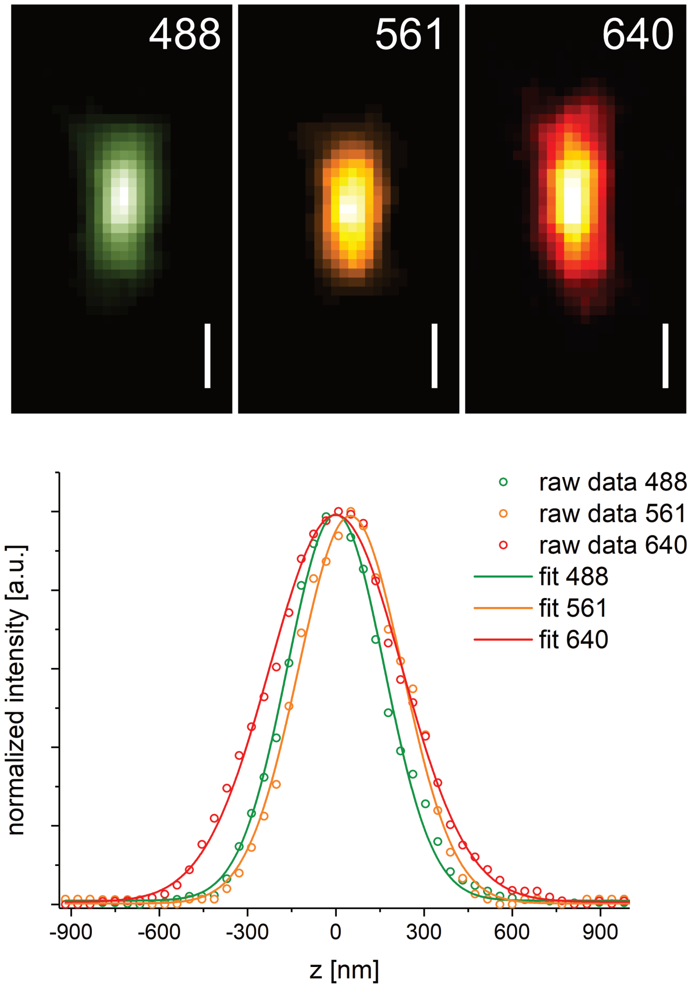

Fig. 3.9 Top XZ views of PSFs acquired with 488 nm, 561 nm and 640 nm. Axial offset has been set in NIS Elements and correction is directly visible in the image. Scale bar 300 nm. **Bottom** Axial line profiles of a 100 nm fluorescent Tetraspeck, acquired as a z-stack with the excitation wavelengths 488 nm, 561 nm and 640 nm in sequential order. Raw data is shown as circles with gaussian fits as solid lines. Intensities are normalized and shifted to the 488 nm channel as reference.

Table 3.5 Deviation of axial PSF to reference of 488 nm PSF after correction by applying focal offset in acquisition software NIS Elements. Errors represent standard error from fit.

Excitation wavelength [nm]	Δz to reference PSF-center [nm]
488	0±2
561	50±3
640	0±2

Resolution, Sampling and Contrast

Resolution is not the only key-player to resolve fine structures. An example is shown in figure 3.10 where two beads in close proximity are imaged first in rescanning mode followed by the confocal mode. From a first look the rescanning image clearly reveals a structure consisting of two individual peaks, whereas the confocal image only shows an asymmetric intensity distribution (3.10 **A**). The line profiles along the elongated axis as depicted in inlet **B** are read out and shown in an overlayed non normalized manner (left) and an normalized way (right). In the confocal mode the peak intensity is far higher as the larger pixel size leads inevitably to higher accumulation of signal. Despite acquiring lower signal the better sampling rate in the RCM mode yields a better contrast and therefore enables distinguishing the bead structure in the example. It should be mentioned that the distance of the peaks evaluated with individual peak fits in **C** does not even lie close to the resolving capability of the RCM itself. The distance of both peaks calculated as $261.9 \pm 2.0\,\mathrm{nm}$ should definitely be resolvable with a standard confocal microscope. In both imaging modes, the Nyquist criterion for pixel size is met. The structure to be resolved (262 nm) would have to be recorded with a sampling rate of 131 nm. In the case of the RCM mode with a pixel size of 43 nm the structure is oversampled 3 times, in the case of the Confocal mode with 86nm pixel size only 1.5 times. Sampling and contrast are definitely essential as well as can be nicely seen here.

The comparison of the intensities contained in the point-spread functions results in approximately 70% higher values in the case of the confocal imaging mode. The doubled pixelsize in confocal imaging mode increases the collection efficiency. In case of the rescanning imaging mode the shifted excitation and emission PSF are convolved, resulting in a better confined PSF at the cost of an intrinsically lower amplitude. Although acquiring less signal the better confined PSF and higher sampling rate (in form of the pixelsize) enhance the contrast and therefore the resolution in the rescanning mode.

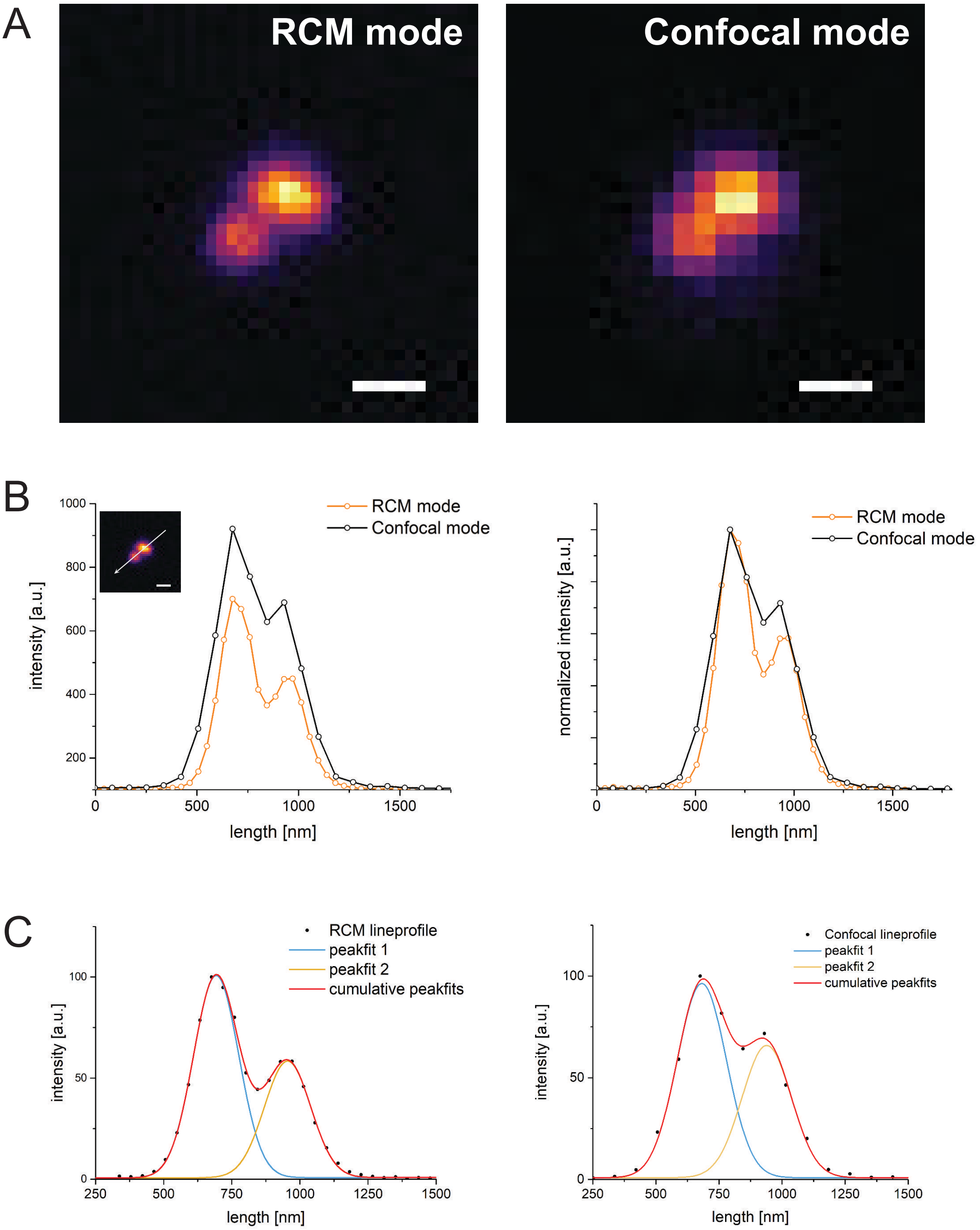

Fig. 3.10 Comparison of resolving power of clustered beads acquired in RCM mode and Confocal mode. **A.** Lateral view of clustered beads in RCM (left) and Confocal mode (right). Note the different pixel size in both acquisition modes. Scale bar 200 nm. **B.** Line profiles along line as depicted in the inlet. Non normalized line profiles show far lower intensity accumulation in the RCM profile compared to the confocal length profile. (left) Normalized line profiles of both acquisition modes. (right) **C.** Peakfits to line profiles revealing the distance of imaged spots for RCM *left* and confocal mode *right*.

3.4 Imaging capabilites RCM

After evaluating the imaging performance of the RCM using sub-diffraction beads, the performance of biological structures will be tested and analysed in the following section. On the one hand, this includes the resolution of structures in the range of the RCM resolution limit as well as the acquisition of multicolor channels. Furthermore, an evaluation of the photo damage is carried out by means of a time-lapse video of a dynamic structure. In the last section the sensitivity of the system on single molecule surfaces is investigated.

3.4.1 Single Color Imaging

A suitable target structure for demonstrating the imaging capability of the RCM system is the cytoskeleton structure build of actin. The purpose of the actin network is to provide stability for the cell shape, adhesion to surfaces and enable migration modes. Strong *stress* fibers extend across the cell whilst a fine meshwork is lying in between. This so called **f-actin** requires appropriate staining and high resolving capability to reveal its fine structures. Figure 3.11 shows the actin meshwork of a mouse embrionic fibroblast cell, stained with phalloidin Dylight 650. Panel **A** displays a focal plane close to the basal membrane, with a homogeneously distributed meshwork. The indicated ROI is displayed as a zoom version (i) and with an unsharp mask applied (radius 2px, mask weight 0.6) (ii). The sectioning capability of the RCM is illustrated in the micrograph in panel **B**, where frames of the acquired z-stack in 200 nm steps are arranged in a montage. The dense meshwork is not only limited to the area close to the basal membrane but is distributed more or less homogeneously within the cell and can be resolved throughout the entire z-stack. In contrast to conventional confocal microscopes, the size of the pinhole of the RCM unit cannot be adjusted, but is fixed at 50µm physical diameter. Using the 100x /1.49 APO TIRF lens, the pinhole diameter is approximately 1.8 Airy Units (AU). The separation performance is extremely efficient, as can be seen in the case of the dense actin network in each focal plane a good separation of the fine filaments takes place.

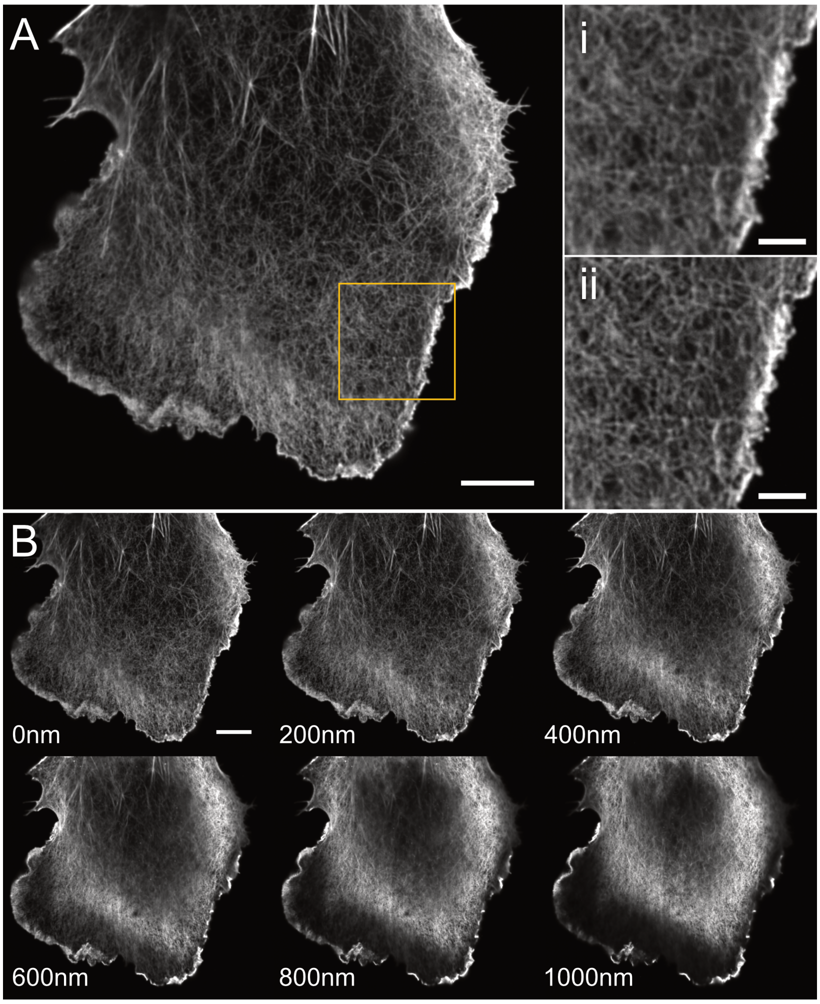

Fig. 3.11 Actin skeleton of a mouse embryonic fibroblast (MEF) cell, stained with phalloidin Dylight650. Panel **A** (left) shows the dense f-actin meshwork close to the basal membrane of the cell. Scale bar 10μm. Inlets is shown as zoomed in version in **i** and with unsharp mask applied in **ii**. Scale bar 3μm. Panel **B** is displaying a micrograph with z-frames 200nm apart. Scale bar 10μm.

Comparison of the resolution capability of rescanning and confocal imaging mode

In order to compare the enhancement of resolution in rescanning mode in contrast to the confocal mode, the actin structure of a COS7 cell has been imaged sequentially in both imaging modes. As resolution capability is increased at lower wavelengths, Alexa Fluor 488 was used for staining and allows resolving structures in the range of formerly confirmed 170 nm resolution. In figure 3.12 the acquired image as shown in the top panel represents the rescanning mode (RCM). The marked ROI is displayed for both imaging modes and a line profile indicates the read out intensity distribution shown in the bottom panel. Line profile intensities have been normalized to achieve better visualization of resolution differences. The RCM reveals far more filament strands in comparison to the confocal imaging mode. In the confocal mode close-by filaments are fused together, whereas the RCM line profile enables a clear separation of structures. The dye used provides sufficient photons to balance the reduced detection efficiency in the rescanning imaging mode.

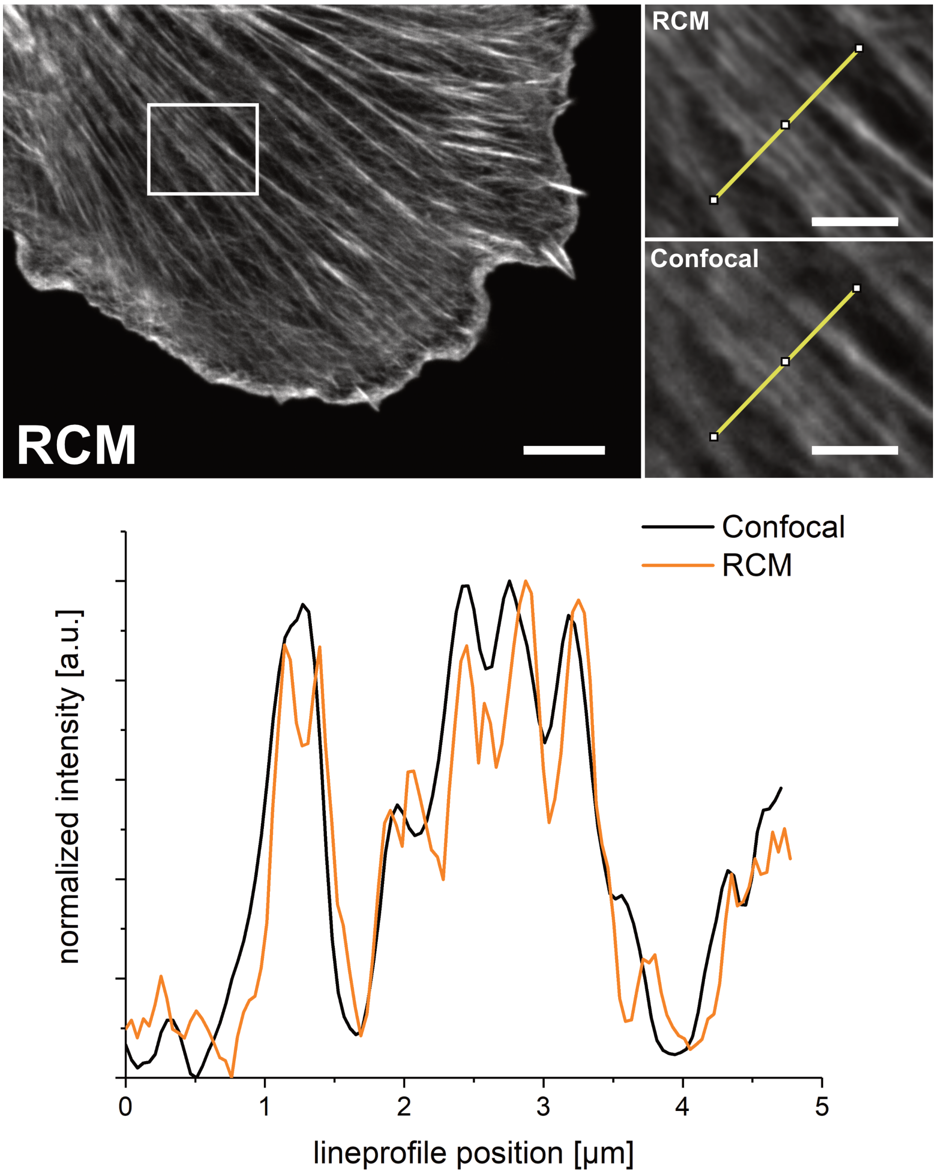

Fig. 3.12 Comparison of structural resolution between RCM and confocal mode. Image of actin skeleton of U2OS cells stained with phalloidin Alexa Fluor 488. **Top** The large image shows the entire cell imaged in RCM mode with marked inlet. Scale bar 5 µm. **Top right** Inlet is shown as magnified view in RCM and Confocal mode. Line profiles for further analysis are marked as yellow lines. Scale bar 2µm. **Bottom** Normalized line profiles of top images indicate the structural resolution enhancement of the Rescanning Mode versus the Confocal mode.

3.4.2 Multi Color Imaging

To demonstrate the capability of multi color imaging a stable HeLa cell line expressing mitochondria tagged with a green fluorescent protein was used. The fluorescent protein survives fixation with 4-% formaldehyde. After fixation a staining of the nucleus with Hoechst33342 has been carried out, as well as an immunostaining of the tubulin network using the fluorescent dye Alexa Fluor 647. The actin meshwork was stained with phalloidin Alexa Fluor 555. Figure 3.13 **A** shows the z-stack maximum intensity projection of a recording showing mitosis in the late telophase with all 4 stained channels. The tubulin network is color coded in red, actin in yellow, mitochondria in green and the nucleus in violet. Panel **B** contains the zoomed in ROI with mitochondria and tubulin, panel C the same region with tubulin and actin. The connection of the cells by tubulin in this phase of mitosis incorporates the so called escort complex, lying in the hollow ring like structure formed by tubulin and actin. the escort complex or short ESCRT (endosomal sorting complexes required for transport) plays an important role in loading vesicles with undesired membrane proteins [ST12]. The complex spatial structure of the ESCRT lies beyond the diffraction limit and requires super resolution imaging techniques. 3D STORM imaging revealed a spiral structure dependent on the time of cell separation. Goliand et al impressively presented their findings in [GALS$^+$18].

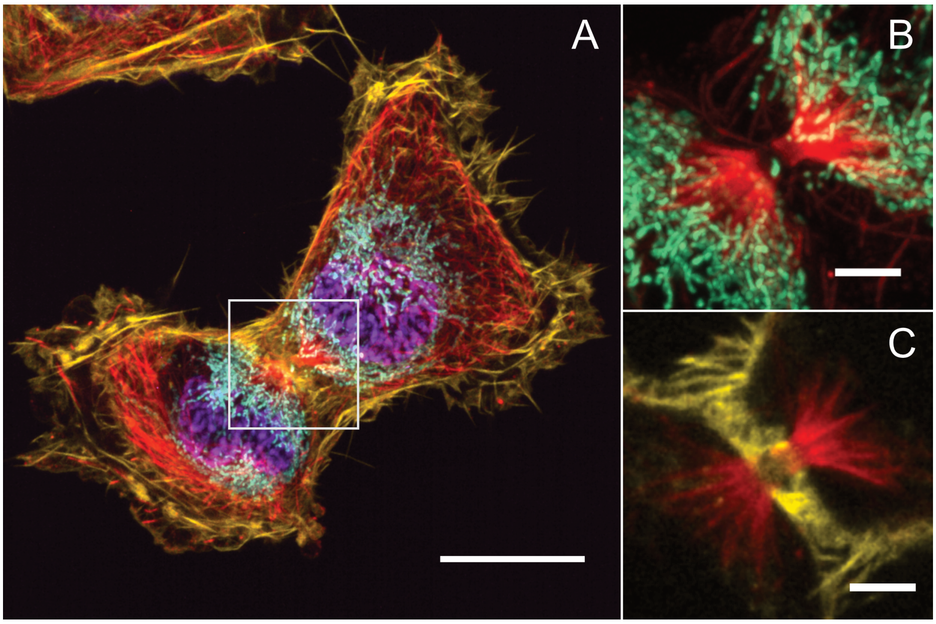

Fig. 3.13 3D multi color imaging of Mitosis displayed as maximum intensity projection. Hela cells expressing Mitochondria tagged with GFP, additional staining of nucleus with Hoechst (violet), actin with phalloidin Atto 565 (yellow) and tubulin via immunostaining with Alexa Fluor 647 (red). **A** Maximum intensity projection of all channels. Scale bar 15µm. **B** Maximum intensity projection of tubulin and mitochondria channel of inlet in A. Scale bar 3µm. **C** Single frame of actin and tubulin channel of inlet in A, showing ring-like structure around ESCRT complex. Scale bar 3µm.

3.4.3 Dynamic Live Cell imaging

As in any standard confocal microscope, the RCM also offers the possibility for time lapse recording. In contrast to a conventional laser scanning microscope, the camera-based image scanning system with a scientific CMOS has a significantly higher quantum efficiency than standard photo multiplying tubes. The used sCMOS Zyla 4.2P detects with 82 % quantum efficiency almost 4 times as many photons as commonly used GaAs(Cs) based PMTs like R942-02 from Hamamatsu [Ham10] with approximately 20% quantum efficiency. Therefore, the excitation laser power can be significantly reduced to obtain a similar signal to noise ratio.

In order to demonstrate the low phototoxicity to light sensitive organisms, a time lapse image series is taken with a HeLa cell line stably expressing the plus-end-binding protein EB1 tagged with the yellow fluorescent protein (YFP). End-binding proteins are able to recognize the ends of microtubules and specifically bind to the proliferating tips. By remaining at the fast growing end, the impression of a comet-like trace is created since a fluorescent protein is built into EB1. End-binding proteins belong to the group of microtuble-associating proteins

(MAP) and are involve in regulation of microtubli dynamics [GAE98].
A time lapse recording over 400 frames with 2 s time interval was recorded with activated focus stabilization. A low laser power of 8 µW achieved by a neutral density filter in the excitation beam path was used while recording. Figure 3.14 A shows the first 100 representative images, the dynamics is visualized by time-color-coded tracks. To quantify the photobleaching effect the mean intensity of the entire field of view was plotted against the time line as shown in panel **B** and the data was fitted with exponential decay. Although a clear bleaching tendency is visible, the calculated decay constant is quite high with a value of 2416 s. The derived half life time with 1681 s would result in sufficient signal detection after almost half an hour of permanent imaging. In order to quantify and compare the influence of light dose on mobility parameters, the EB1-YFP tracks were recorded and speed and accumulated distance for the first and last 100 frames evaluated. In panel **C** and **D** the estimated data is shown as box plots. As automatic detection of the EB1-YFP signal failed in Imaris analysis software due to elongated intensity strands, tracks were analysed manually in ImageJ. In total 50 tracks per dataset were acquired and statistics evaluated. All values are listed in table 3.6.

Table 3.6 Comparison of mobility parameters of EB1-YFP tracks between first and last 100 frames of a time lapse series containing 400 frames in total. Values listed as median with standard deviation.

[nm]	velocity [µm/min]	accumulated distance [µm]
first 100 frames	17.1 ± 2.8	6.6 ± 2.8
last 100 frames	19.1 ± 5.8	5.1 ± 2.8

The permanent recording and illumination of the cell seems to have only minimal influence on the internal dynamics of the growing microtubule ends. The median value of the velocity increases slightly from around 17 µm/min in the first 100 frames to 19 µm/min in the last 100 frames, but remains within the scope of the error. The accumulated distance of the growing microtubuli ends decreases in contrast from 6.6 µm to 5.1 µm, again in the scope of the error. In order to test for statistical significance of both dataset, data was tested for normality using Anderson-Darling and D'Agostino&Pearson omnibus test. In both analysed datasets (velocity and track length) the first 100 frame are normal distributed in contrast to the last 100 frames. Therefore no parametric test (like t-test) could be used for analysis of significance. In case of velocity the Kolmogorov-Smirnov results in significant differences (p=0.0013) of both evaluated velocity values. Regarding the track length a Mann-Whitney test has been used showing again significant differences (p=0.0383). As phototoxicity definitely will have

a certain impact on the vitality of a living cell, but no obvious damage such as blebbing is visible as a direct result of the excitation. The effect of the non-physiological imaging conditions may therefore have a much stronger effect on intracellular mechanisms and may result in non normal distributed dynamic values.
In summary, no significant change in tubulin dynamics can be observed, although the cell was exposed to permanent irradiation during the 10-minute timelapse acquisition. Furthermore, the experiment was performed at room temperature without the use of an incubation system nor a pH stabilizing buffer.

The RCM was chosen because of its low phototoxicity and improved resolution to study the influence of a click chemistry labelled taxol derivative (docetaxl) on tubulin dynamics [BKK$^+$19]. Furthermore, the RCM was used for live cell measurements where structural analysis of cell lines with ferroptose-inhibiting gene modifications was the goal. These experiments were additionally performed with a sample incubator to exclude cell death by non-physiological conditions (Attachment C, Manuscript 1, accepted).

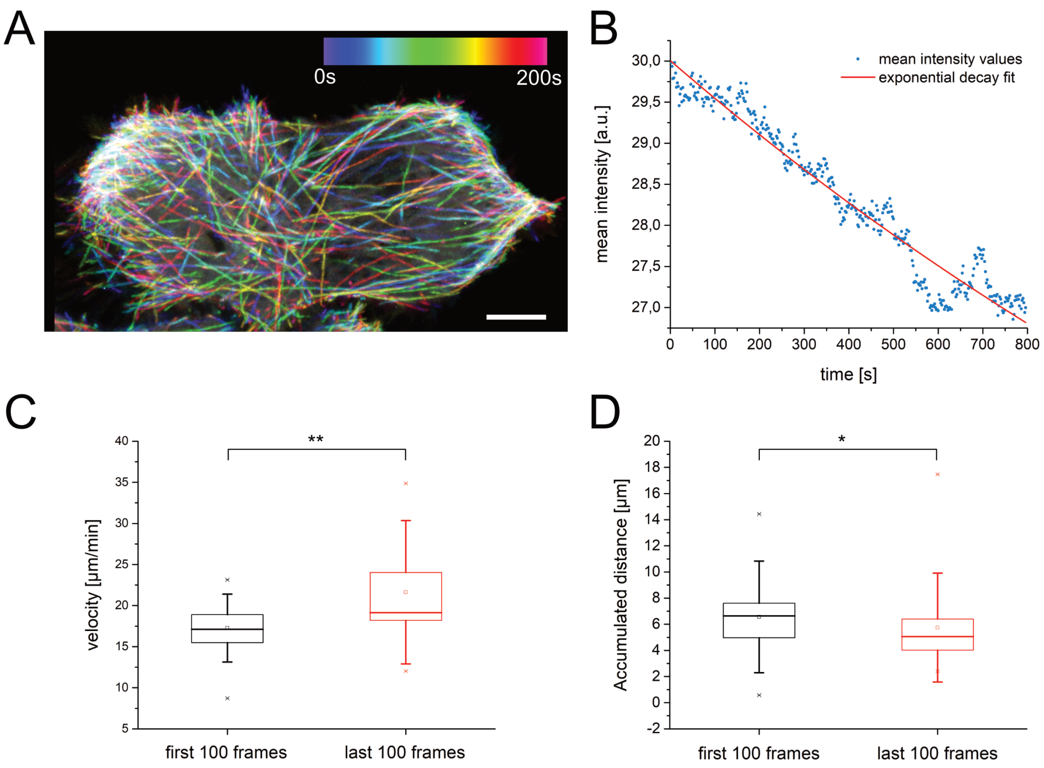

Fig. 3.14 Analysis of phototoxicity impact on dynamic properties. **A** Color coded EB1-YFP time traces of the first frames representative of a timelapse over 800s with 2s time interval. Scale bar 5 µm. **B** Mean intensity trace of full image over the entire timelapse series. Data is shown in blue dots, with exponential decay fit as solid red line. Quantitative comparison of dynamic parameters between first 100 and last 100 frames of the timelapse acquisition. **C** Boxgraph of estimated velocities and **D** accumulated distances of the analysed tracks. Solid horizontal line represents median, lower box end indicate 25%, higher box end 75% of data content and error bar marks 1.5 fold standard deviation.

3.4.4 Single Molecule Sensitivity

In addition to the features highlighted in the previous sections, the camera-based confocal detection system has another outstanding feature. Due to the high quantum efficiency detector of 82%, the RCM system is single molecule sensitive. Despite the fixed and comparatively low pixel dwell time of 2.4 µs, sufficient photons are collected to detect single molecules. A prerequisite for this is a higher excitation laser power and the use of the confocal imaging mode as the detected intensity is around 70% higher than in rescanning mode (see section 3.3). Although the pixel dwell time can be set much higher in a conventional confocal laser scanning microscope, a high excitation laser power would still be necessary. The resulting slow scanning speed therefore leads to rapid bleaching of the dyes.

To demonstrate the sensitivity of the RCM, a single molecule surface was prepared with very bright and photo-stable SeTau-647 dyes. The dye molecules are coupled to BSA and homogeneously distributed over the surface. For the average degree of labelling 1 dye per BSA is to be expected, resulting from ensemble measurements of absorption spectra and further calculation of degree of labelling carried out by Dominic Helmerich. Images have been acquired with 1 mW and in the confocal scanning mode. A control signal was acquired in the 488 nm channel, to exclude that any fluorescent particles are imaged except the dye itself. Figure 3.15 shows the single molecule as raw data in panel **A** *left* and denoised data *right*. Denoising has been performed in NIS elements software using the advanced denoising feature with an iterative prediction algorithm (strength 5). Slight brightness and contrast adjustments achieve outstanding removal of background pixel noise, which allow a fluorophore intensity pattern to be entirely recovered. Panel **B** displays the marked ROI as zoom in version for the raw data (top) and a corresponding dark image displaying the read out noise generated by the camera without any incoming signal. FWHM has been analysed for both fluorophores and the data in table 3.7 is fully consistent with the expected resolution of the confocal scanning mode in the 640 nm channel with a FWHM value of 280 nm. The deviating value for the FWHM x (222 nm) of the left bead can be due to the low signal and the resulting inaccurate gaussian fit. On the other hand, the SeTau-647 dye exhibits intrinsic triplet blinking which can lead to intensity fluctuations between the line scans during recording. The single molecule intensities are at the lower edge of the detectable signal. Panel **C** shows the histogram of the raw data of intensity distribution in a dark image (representing readout noise and mean value as offset) as well as the single molecule signal. The accumulation of the signal at an intensity value of approximately 113 is slightly above the background noise of the camera. However, the intensity distributions of the individual spots clearly stand out from the background noise. From the mean value of the signal of the individual spots as well as the noise components caused by read-out noise and dark current noise, a signal to noise ratio of 47 is calculated. Read-out noise is determined experimentally from the difference between two sequentially recorded dark images at a value of 2.956 $e^{-} rms/pixel$; the dark current noise component is determined by the manufacturer's specifications at 0.115 $e^{-}/pixel/s$.

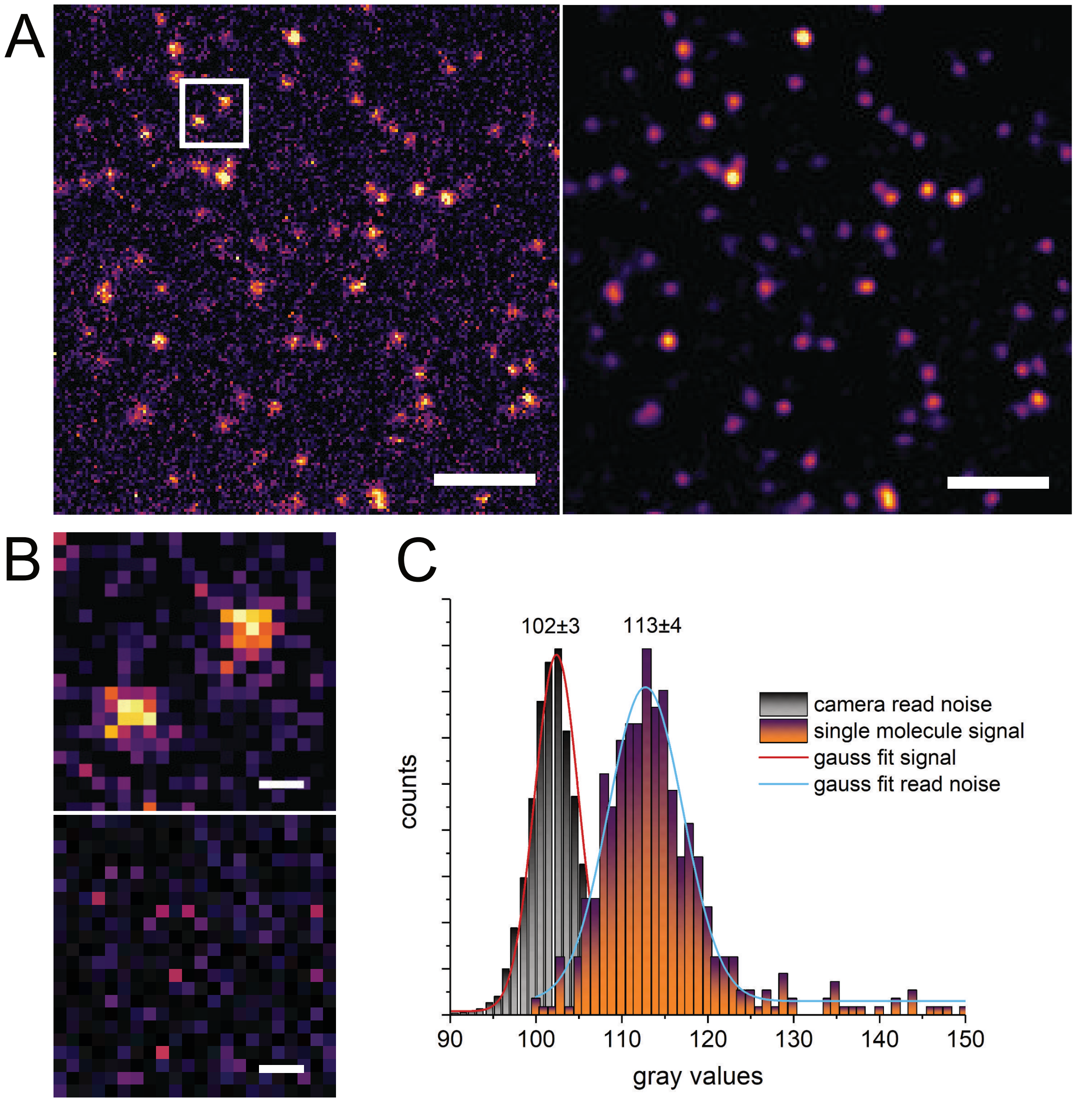

Fig. 3.15 Single molecule surface with SeTau-647 dyes imaged with the confocal scanning mode of the RCM-unit. **A** Raw data (left) and denoised data (right) of detected single molecule intensity distributions. Scale bar 3 µm. **B** *top* Enlarged view of the marked region in A with two isolated SeTau molecules, used for FWHM estimation. Scale bar 300 nm. *bottom* Dark image of the same spot displaying read noise generated by the camera. **C** Histogram and gaussian fits of the raw data intensities of measured camera read noise and measured single molecule signal. Mean value with standard deviation are displayed for each distribution.

Table 3.7 Lateral dimensions of single SeTau-647 dyes shown in figure 3.15 B.

	FWHM x [nm]	FWHM y [nm]
bottom left spot	291 ± 18	222 ± 31
top right spot	293 ± 18	293 ± 30

A conversion of the intensity count based data to true photon counts reveals a more intuitive understanding of the sensitivity of the RCM system. Furthermore a theoretical estimation of the single molecule detection probability is made. The following values and assumptions are necessary for an estimation of the expected detectable photons per pixel:

SeTau Dye

quantum efficiency (conjugated): $\approx 58\%$

extinction coefficient: $2.11 \times 10^5\,\mathrm{mol}^{-1}\,\mathrm{cm}^{-2}$

Excitation

wavelength: 638nm

excitation power: 2mW

FWHM confocal mode @640nm: $\approx$ 280nm

Detection

numerical aperture: 1.49

refractive index: 1.52

dwell time: 2.5µs

quantum efficiency Zyla @690nm: $\approx$70%

The first step is to estimate the power density in the scanning spot at set 2mW excitation power. The scanning spot is a gaussian spot with an FWHM of 280nm. The power density P$_d$ is calculated as

$$P_d = \frac{excitation\ power}{illumination\ area} = \frac{2mW}{\pi \cdot (280nm)^2} = 8.1 \times 10^9\,\mathrm{J\,m^{-2}\,s^{-1}}. \tag{3.2}$$

Using the photon energy for a wavelength λ of 638nm

$$E_{\nu,638} = \frac{hc}{\lambda} = 3.11 \times 10^{-19}\,\mathrm{J} \tag{3.3}$$

the photon flux Φ through the spot area per second can be estimated as following:

$$\Phi_{flux} = \frac{P_d}{E_{\nu,638}} = 2.6 \times 10^{28}\,\mathrm{m}^{-2}\,\mathrm{s}^{-1}. \tag{3.4}$$

The photon output of a single SeTau dye is determined by its quantum yield QY and the absorption cross section σ_{abs}. The latter can be derived from the extinction coefficient and the Avogadro constant

$$\sigma_{abs} = \frac{extinction\ coefficient}{N_{Avogadro}} = 3.5 \times 10^{-35}\,\mathring{A}^2 \tag{3.5}$$

and is expressed in Angström. The emitted photons are estimated as

$$\Phi_{emitted} = \Phi_{flux} \cdot \sigma_{abs} \cdot QY = 5.3 \times 10^{9}\,\mathrm{photons/s}. \tag{3.6}$$

The collection cone of the objective is mainly limited by the numerical aperture NA with half opening angle α and the refractive index n. The collection efficiency C_{obj} can now be calculated using the canonical spatial angle Θ of the cone as a proportion of the entire spatial angle:

$$C_{obj} = \frac{2\pi(1-\cos\alpha)}{4\cdot\pi} \approx 40\%. \tag{3.7}$$

Collection efficiency towards the camera is further reduced by 5 achromatic lenses ($\approx 95\%$ transmission), 2 full reflective mirrors ($\approx 96\%$ reflection), a dichroic mirror ($\approx 95\%$ transmission), two mirrors of galvo-scanners ($\approx 96\%$ transmission) and an emission filter ($\approx 90\%$ transmission), in total a collection efficiency of $\approx 23\%$.
The overall photon number remaining for detection is reduced to

$$N_{detectable} = 1.2 \times 10^{9}\,\mathrm{photons/s}. \tag{3.8}$$

The quantum efficiency of the camera as well as the integration time, in this case the pixel-dwell time are finally determining the number of collected photons

$$N_{detected} = QE \cdot t_{dwell} \cdot N_{detectable} \approx 2400\,\mathrm{photons}. \tag{3.9}$$

These photons are in a simplified assumption distributed equally over a pixel array of 4x4 pixel covered by the PSF resulting in

$$N_{pixel,PSF} = \frac{N_{detected}}{4x4pixel} = 150 \tag{3.10}$$

expected photons per pixel of the covered PSF.

In order to verify the assumptions and estimations made, the data shown in Figure 3.15 has been analysed. First, the offset of 103 counts of the camera was subtracted from the raw data. The conversion factor of intensity values to electrons at 540MHz readout rate and low-noise settings is 0.29 e/AD count. The raw data were divided pixel by pixel by the conversion factor. The conversion of photoelectrons into photons is now done by dividing the pixel values by the quantum efficiency of the camera, in this case 70%. In figure 3.16 the emission patterns of two individual SeTau molecules is shown, with photon counts for each pixel in the 4x4 area as taken for estimation before. The sum of photons contained in each area is with values of 2442 and 2461 photons in a comparable range as calculated in equation 3.9. In panel B the photon distribution of 57 separate emission areas has been plotted, with a (136±45) photons per single pixel. The distribution follows a normal distribution, which is confirmed by the fitted Gaussian curve. The estimated value of 150 photons as in equation 3.10 is close and validates the made assumptions. Estimation of photons per 4x4 pixel area yields 2194± 307 photons as mean (SD).

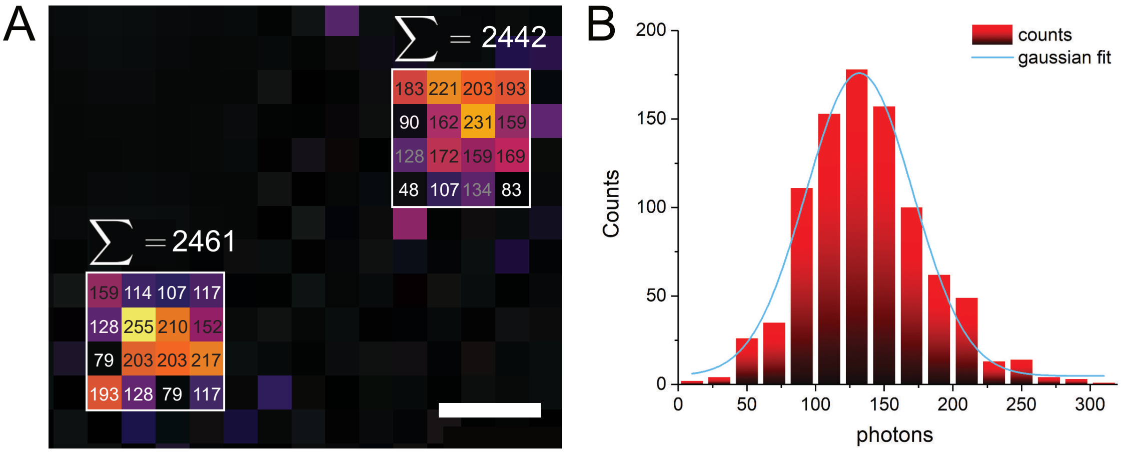

Fig. 3.16 Analysis of the photon budget in PSF of single SeTau molecules. **A** Conversion of intensity values to photons illustrated for two individual molecules in an area of 4x4 pixels. The values correlate to photons per pixel, with summed photons for the top spot of 2442 and for the bottom spot of 2461 photons. Scale bar 200 nm. **B** Photon distribution for 4x4 pixel area of 57 analysed single molecules with 136±45 photons per pixel in average.

3.5 Microscope with fast buffer exchange system

For carrying out a holistic experiment, which includes dynamic measurements on living cells as well as applying single molecule localisation microscopy on fixed cells, a contactless interaction with the sample on the microscopy stage is necessary in order to keep the field of interest of the sample. Therefore, a microfluidic pump was integrated into the existing system, a control software was designed, sample chambers were evaluated and the interaction with different samples was tested.

3.5.1 Microfluidic setup

The MitosDuoXS is a microfluidic pump system from *Dolomite Microfluidics*. The pump is designed for enabling laminar flow with large flowrates, a key requirement for interaction with living cells as in our application. Flow rates can be set within a range from 0.1 µl/min to 10 ml/min depending on the used syringe size. The syringes are replaceable by the user, as well as the valve system. The pump is equipped with two syringes enabling continuous or double refilling pumping mode. The valves have a port system ranging from 2-6 ports which can be set according to the attached reservoirs.

The configuration of the pump has two syringes with a 2-port valve each. It is equipped with 1ml volume syringes each, as this volume is the upper limit of standard labtek wells and custom made sample holders. Tubes are made of chemically high resistant polytetrafluorethylen (Teflon) and have an inner diameter of 0.8 mm. The dead volume of the supply line was calculated for a tube length of 30 cm to 150 µl. This dead volume has to be taken into account when preparing buffers and setting pump volumes.

Table 3.8 Configuration and accessories of the microfluidic pump MitosDuoXS

Part	Specification	Part No.
pump	MitosDuoXS - Basic	3200057
syringe	1ml	3000252
valve	2-port	3000244
tubing	0.8 mm diameter (PTFE)	3200068

To decouple the pumping system from the microscope setup, a construction from the ceiling has been installed, allowing to have the pump hovering as close as possible to the sample stage and avoid any possible vibration disturbance.

3.5.2 Control Interface for MitosDuo XS

The microfluidic pump system is delivered with a simple control application, for manually intake and pumping of individual syringes. For the planned experiments far more complex and flexible pump protocols are required. Therefore a graphical user interface (GUI) was programmed in the python environment in the context of this thesis as shown in figure 3.17. Panel **A** shows the main part of the application with control buttons for individual pumping modes. All pumping modes are started by clicking desired button. The control button *parameter* opens the window shown in panel **B**, where the number of pump cycles as well as the individual syringe volumes can be set and then updated for further pumping procedures. The last panel **C** gives the user feedback of pump settings as well as current actions. The displayed log provides following information:

- *COM3 is open* - serial port COM3 is open for communication with the pump
- *flushed COM port* - all communication messages are erased
- *initialised valves/syringes* - Reset of syringes and valves to their starting position
- *Status ...* - status report after initialisation of syringes and valves. Digit combination according to the manual: Adress of the syringes (1. - 009/ 2. - 019), valve and syringe are idle (1 1), valve and syringe are in starting position (0 0 0)
- *Initialisierung abgeschlossen* - Initialisation finished, pump is ready for action
- *Pump cycles...Syringe 1... Syringe 2...* - Set parameter values

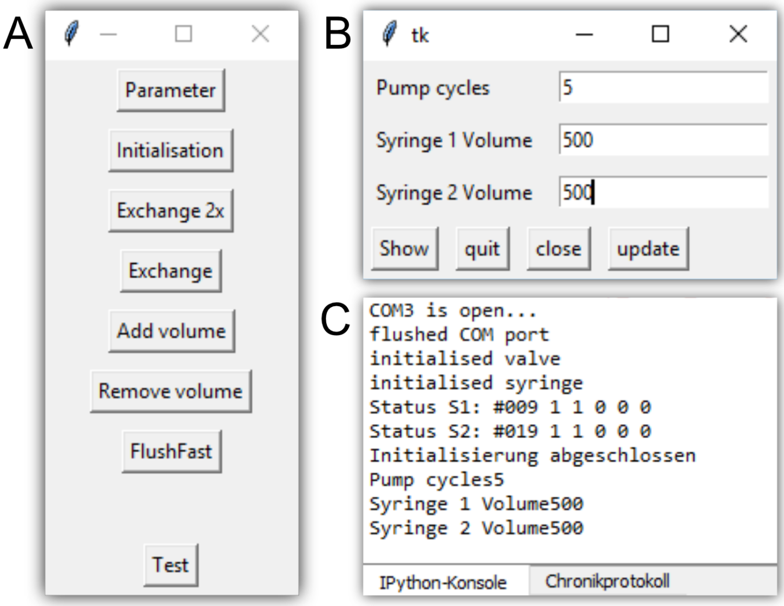

Pump cycles 5
Syringe 1 Volume 500
Syringe 2 Volume 500

```
COM3 is open...
flushed COM port
initialised valve
initialised syringe
Status S1: #009 1 1 0 0 0
Status S2: #019 1 1 0 0 0
Initialisierung abgeschlossen
Pump cycles5
Syringe 1 Volume500
Syringe 2 Volume500
```

Fig. 3.17 Graphical User Interface (GUI) written in python for controlling the MitosDuoXS Pump. **A** Main GUI with settings for pump parameters, initialisation and several pumping modes. **B** Pump parameters including cycle number and pumping volumes for both syringes. **C** Console log with status display for both syringes.

As initial experiments showed, a number of different pumping protocols are used often and a certain flexibility during experiments is required. Therefore all necessary pumping protocols are present in the main application window and still allowing adaptive changes required by the experiment. The flowrate of 4 ml/min (≈ 70µl/s) has been experimentally determined as optimal for live and fixed cell experiments and is set as a fix value and not changeable in the GUI interface. A skilled user still can choose different values in the underlying architecture. The pumping modes displayed in the main GUI in figure 3.17 **A** have the following functions in detail:

Parameter - Setting of pump cycles and syringe volumes in µl.

Initialisation - Initialisation of syringe and valves, necessary if pump does not react correctly.

Exchange 2x - Exchanging the medium of the sample chamber with minimal *dry time* of the sample. Preset of 2 pump cycles with set volumes in parameter input, pump cycle in parameter is overwritten.

Exchange - Exchanging the medium of the sample chamber with minimal *dry time* of the sample. Number of pump cycles with set volumes according to parameter input.

Add volume - Addition of volume. Syringe 1 adds set volume to sample, syringe 2 is idle

Remove volume - Removal of volume. Syringe 2 removes set volume from sample to waste, syringe 1 is idle

Flush Fast - Fast exchange of sample volume and synchronous flushing of set volume with maximum flow rate

Test - Testing the serial communication

All the given options enable several procedures to interact with the sample, either in live or in fixed conditions. Fixation of a live cell sample, adding post stainings, exchanging buffer for performance of *d*STORM imaging or adding any kind of reactive agent can be done with the given pumping procedures.

The *Exchange 2x* preset turned out to be heavily used, as 2 times exchanging buffer is required to completely remove also the buffer remaining in the dead volume of the tubing between syringe and sample. A single exchange pump cycle is always going to add the remaining dead volume together with the new buffer to the sample. With certain buffer conditions this small amount might have critical effects on following procedures of the experiment.

The *Fast Flush* option provides an easy pumping protocol for cleaning syringes, valves and tubing. Concerning the flushing and preparation for idle period of time certain care has to be taken.

1. flush entire pump loop several times with ethanol
2. flush entire pump loop several times with destilled water
3. store pump loop in destilled water, otherwise leackage is ocurring and corrosion effects will kick in

3.5.3 Sample chambers

In general every sample chamber compatible for seeding cells could be used as long as there is any possibility to connect the tubings to the chamber. The necessary volume for filling the chamber definitely rules out several options. The choice of syringe size is determining the maximum exchangeable volume of the chamber. For expensive buffer contents like antibodies a smaller volume is also an advantage. Usage of several different chambers has been evaluated and advantages and disadvantages are listed hereafter.

Ibidi channel slides

When starting experiments with the MitosDuoXS the first choice for sample chambers were channelslides from Ibidi as the lyer connections of the slides could be easily connected with the tubes of the pump. The used channelslides have a restricted diameter of 400µm x 3800µm (HxW). The volume of the channel depends on the channel length. For single channel slides the channel has a volume of 100µl, the 6-channel slide contains only 30µl of volume. The restricted dimensions are highly critical for setting a suitable flow rate in order to not flush attached cells out of the channel. Low flow rates are necessary to avoid the turbulent flow regime. At an experimentally determined flowrate as low as 15µl/min living cells remain attached. Any gaseous bubble entering the channel is a potential risk to rip off living as well as fixed cells. Setting up a bubble free connection loop and also retain it during pump protocols is quite challenging. Gas evolving media like reducing buffer in immunofluorescent stainings should be definitely avoided and therefore reduces applicability for certain experiments. The low weight of the channel slides must be taken into account, as the tubing is quite stiff and tends to exert a force to the slide.

Multiwell sample carrier

Multiwell sample carrier like 8-chambered labteks from *NUNC, Sarstedt, Cellvis* are widely used in cell culture, as they allow several experiments and controls in the same carrier. The minimal volume to be filled in each well is reasonably low with 200-300µl. As no commercial lid for attaching tubes to the wells was available, custom made lids were designed. For each brand a lid was manufactured by the departments workshop with a transparent lid. Two holes for inlet and outlet were drilled through the lid, located in the opposite corner of the corresponding well below. Tubes are pushed through the access holes, the inlet tube positioned halfway above the cover slip, the outlet tubing touching the glass surface. As the access holes are positioned extremely close to the corner, the inlet flow runs smoothly down the well wall, avoiding creating droplets. The tubing end was cut slightly inclined, avoiding any under-pressure in the outlet tube.

Handling these type of sample chambers is very convenient, there are no limitations given concerning flow rate or gas evolution in medium. One major drawback might be the sacrifice of 7 unused wells when experimenting with living cell samples in one specific well, assumed cells were seeded there and no incubation system is used.

Custom made coverslip sample holder

In order to further improve the sample carrier, a custom made stainless steel cover slip holder was designed. Cover slips with 18 mm diameter can be transferred to the inner tube of the sample holder, fixed with a screwed in plastic mount with 5 mm wall thickness, serving as temperature isolation. A tight fitting lid has again drill holes for the tubing located close to the walls of the mounting inlet. A third bore hole has been inserted to allow the release of gas. The sample mount holder is heavy weighted, providing increased stability and low drift during long term acquisitions. Critical point concerning handling might be the transfer step of the cover slips to the mount.

Table 3.9 Overview sample holder with pros and cons

	channel slide	multiwell carrier	custom made coverslip mount
handling	✓✓	✓✓✓	✓✓
stability	✓	✓✓	✓✓✓
volume saving	✓	✗	✗
flowrate restriction	✓	✗	✗
buffer restrictions	✓	✗	✗

In table 3.9 all advantages and disadvantages of mentioned sample holders are listed. Usage depends definitely on the type of experiment. Most live cell experiments have been carried out in the custom made cover slip mount, as cells have been transiently transfected and use of cover slips seemed more appropriate in terms of material consumption.

General preparation and handling

The most important steps concerning handling of pumping modes and preparation of tubes and pump as well as long term storage are listed below.

- before usage, use "flush fast mode" to clean the pump first with ethanol and then with PBS.
- for live fixation fixation or any live cell experiments buffer should already be in the tubing, keep outlet of tube dry, otherwise droplets of medium might interfere already with cells upon contact with tube end
- set volume in sample chamber to a certain value (like 500 µl), this is important when setting the exchange volume later for pumping

- check pump cycles, important for buffers that need incubation!
- always flush between incubation steps (use exchange mode with higher number of cycles)
- after finishing experiments flush in fast mode with ethanol and as last cycle distilled water. Keeping ethanol in the syringes leads to leakage and PBS leads to corrosion!

3.5.4 Microfluidic interaction with sample

On-the-fly fixation

One of the basic experiments is the fixation of a given sample while keeping the target of interest in the field of view. This allows to apply further imaging procedures all linked to the same cell. Especially follow-up experiments subsequent to dynamic live cell observations would be enabled as well as additional intracellular stainings and single molecule localization imaging. The following experiment demonstrates the live observation of the fixation process, henceforth called '*On-the-Fly-Fixation*'. A goal target for this purpose is the rapidly growing microtubule ends visualized by attaching end binding proteins (EB3) tagged with the fluorescent protein dTomato. The dynamic process is recorded with a time lapse series during which the chamber medium was exchanged with prewarmed fixation medium (4-% formaldehyde in cytoskeleton buffer). As sample transient transfected COS7 cells (protocol 2.2.2) expressing the end binding protein EB3-dTomato are used.
Figure 3.18 shows a montage of an excerpt of this time lapse series, displaying every second frame. The exchange of medium is visible in time frame T= 28 s as the activated perfect-focus-system lost the reference plane due to disturbance induced by the addition of the medium. The expression of EB3 stopped in less then 10 s and fluorescence intensity decreased to background level. In figure 3.19 the mean intensity trace of the entire time lapse is shown. The time lapse was recorded over 145 frames with 2 s time intervals. At frame 107 the fixation medium was flushed into the sample chamber, the light-red colored area marks the time frames with fixation medium. Being a highly sensitive measure for viability of the cell as [WLK$^+$15] show by long term irradiation induced damage, the immediate impact of the fixation process on the expression of the end-binding protein is quite astonishing. The exact trigger of the decrease of intensity however remains unclear. Either the tubulin binding site is immediately damaged or not accessible anymore or the cytosolic EB3-dTomato lost the ability to bind. It has been shown as in [RCL$^+$17], [FST08] that the fluorescent protein survives fixation quite well, therefore a pure destruction of the fluorescent protein could be ruled out.

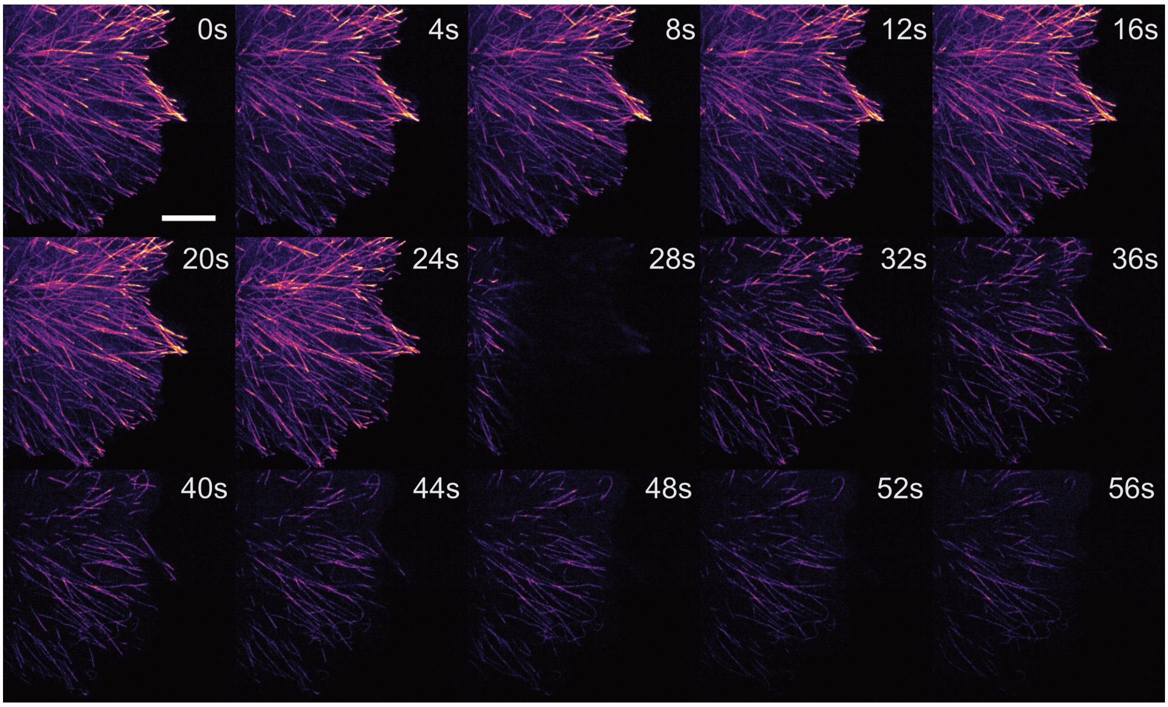

Fig. 3.18 Excerpt of time lapse of COS7 cells expressing end-binding protein EB3 tagged with fluorescent protein dTomato. Fixation medium was flushed in during acquisition visible at time point T=28s. Fixation happens in the following frames and fluorescence intensity vanishes immediately. Frame interval is displayed at 4s, recorded with 2s intervals. Scale bar 10µm.

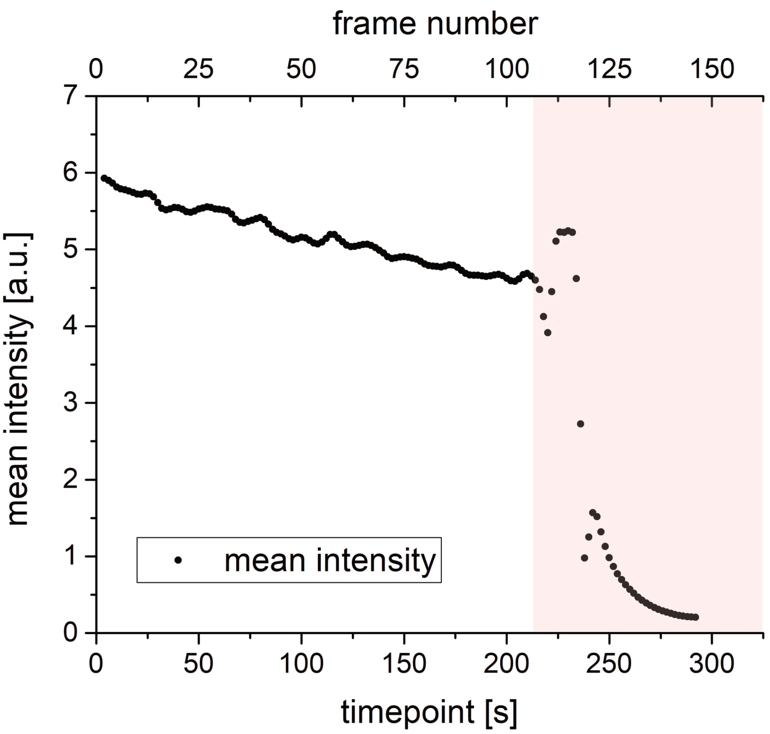

Fig. 3.19 Mean intensity trace of the entire time lapse of COS7 cells expressing EB3-dTomato. The time lapse consists of 145 frames (top axis), with 2s time interval (bottom axis). The highlighted region marks the phase of induced fixation.

On-the-fly staining

Another fundamental experiment besides live fixation is the addition of buffers to a live cell experiment in order to observe and visualize dynamic effects. In general this possibility of interaction with the sample would allow to directly monitor for example internalisation of added compounds like labelled transferrin, visualize effects of inhibitors like microtubule dipolymerization and more. To demonstrate and visualize the addition of buffer to a running live cell experiment a CellMask staining is added during the acquisition of a time lapse series. To emphasise the live cell imaging conditions a COS7 cell line expressing before mentioned EB3-dTomato was imaged in a time lapse manner in the 561nm channel. Additionally the 488nm channel was acquired sequentially. During the acquisition cell mask green staining (in prewarmed cell culture medium) was pumped into the chamber. Figure 3.20 shows a montage with several frames of the entire experiment. In panel **A** the first frame of each channel (561nm: EB3-dTomato, 488nm: cell mask green) is displayed. Distinct signals of the end binding protein is visible while no signal is detected in the green channel. Panel **B** shows a micrograph of the first 160s of the ROI in A. Every fourth frame is kept to achieve better impression of the procedure. The resulting frame interval is 16s, as two channels were acquired sequentially. The cell mask staining has been added according to the recommended dilution of 1 to 1000, mixed in prewarmed cell growth medium and added after 20s. In the micrograph the staining of the plasma membrane increases steadily over time. However the dynamic of the end binding protein EB3 seems to be heavily affected as the signal decreases strongly until a complete loss of dynamics is reached. The plasma membrane is within 160s fully stained as can be seen in panel **C**, the distinct EB3 signal on the other hand has completely vanished. The tubulin strands remain visible, probably end binding proteins are still attached to their binding sites. The cell did not show any sign of photo-induced or staining-induced damage like blebbing or detaching from the cover slip. Again the end binding protein shows strong sensitivity to changes of the cell environment.

The demonstrated visualisation of on-the-fly staining can be transferred to a variety of experiments where direct observation of active agents is necessary to reveal better understanding of possible interactions with the target of interest.

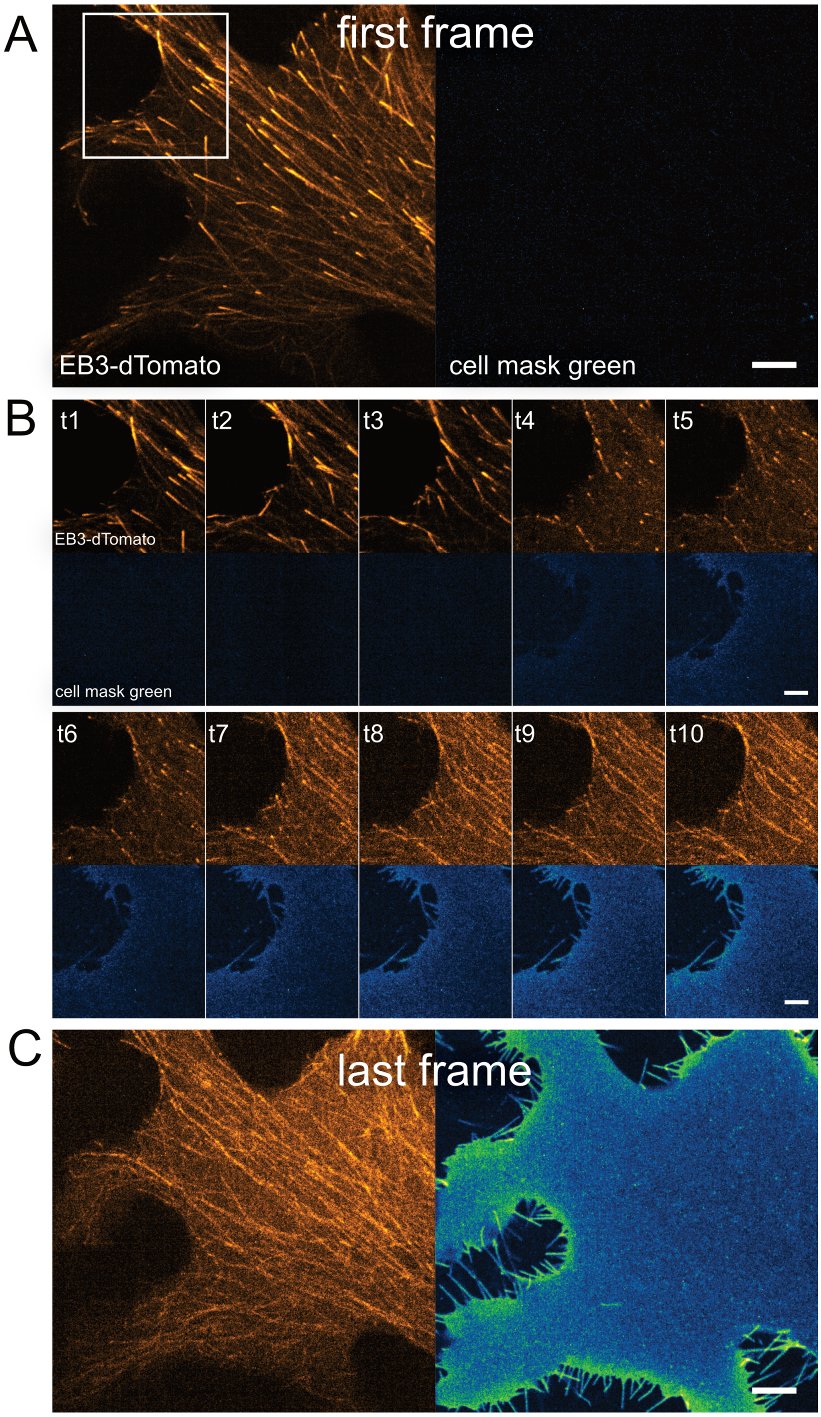

Fig. 3.20 Time lapse video of COS7 cell expressing EB3-dTomato while adding cell mask green staining. **A** First frame of the time lapse showing both channels. EB3-dTomato signals are clearly recognisable but no signal in the 488nm excitation channel is visible. Scale bar 10µm. **B** Montage of the first 160s during addition of the cell mask green staining. Images are taken from ROI in A, time interval 16s. Top row shows the decreasing EB3-dTomato signal while the bottom row shows the increasing staining of the plasma membrane in the green channel. Scale bar 5µm. **C** Last frame of the acquired time lapse showing complete depletion of the dynamic EB3-dTomato signal, whereas the plasma membrane is fully stained. Scale bar 10µm.

3.6 Single molecule detection path

3.6.1 Installation of adaptive optics detection

A standard detection path for 2-dimensional Single Molecule Localisation Microscopy (SMLM) would not require complex optical paths. A suitable camera could be attached directly to the sideport of the microscope and the camera chip should be perfectly located at the image plane after the tube lens.

Any extension of the detection path requires optical knowledge and expertise in alignment. As setting up the detection path in order to including the deformable mirror did not turn out to be straight forward as expected, several critical steps of alignment should be addressed hereafter. Andrey Aristov from Institute Pasteur (Paris) is to be thanked at this point for helpful information regarding the alignment. The deformable mirror has to be placed in a fourier plane of the detection path. In order to gain access to this plane, the original image plane is relayed with a 4f system. The deformable mirror is placed in the focal plane of the first lens of the system. The geometry of the detection path has to be adapted to the reflective type of additional optical element and is visualised exemplary in panel **A** of figure 3.21. Exactly this change of geometrical path adds additional difficulty as no railing system can be used for easy placement and adjustment of optical elements.

The relay system - architecture and alignment

The intended setup of the detection path was designed according to the publication [ALRZ18]. The relay system consisted of lenses L_1 and L_2 with 100 mm and 200 mm as focal lengths. The original choice of the first focal length being 100 mm was matched with the aperture area of the deformable mirror. Overfilling this area would lead to significant loss in intensity. The filling of the modulating area of the deformable mirror correlates with the strength of deformation required to achieve a desired PSF shaping.

Aristov reported that using the mentioned lens configuration require in general a larger amount of deformation of the mirror segments to achieve more complex PSF shaping. Hence this lens configuration leads in long term usage to irreversible alteration of the default voltage pattern of the individual segments that could be hardly corrected. As a combination of lenses with 200 mm and 400 mm focal length turned out to be still suitable in terms of fill factor of the mirror aperture I decided to change to that configuration. The additional magnification factor of 2x of the relay system is maintained.

For setting up the relay system a collimated and expanded laser beam is generated. A clean beam profile is very helpful therefore a DPSS laser is preferred, as stacked diode lasers create stripes in the beam profile. Collimation is checked with a shearing plate interferometer (Thorlabs - SI100). The collimated beam is coupled into the microscope and reflected towards the sample plane. A mirror reflects the beam back to the dichroic, the latter should be chosen in a way that transmission as well as reflection should be high for the given laser wavelength.

3.6.2 The alignment procedure

The first relay lens

The collimated beam is focused by the tube lens indicating the position of the image plane outside the microscope. When placing the shearing plate interferometer along the optical axis outside the microscope, the position of the first relay lens along the optical axis can be found when the beam is collimated again.

Preliminary fourier plane estimation

The tube lens is now bypassed in order to get a preliminary position of the backfocal plane of the first relay lens equivalent to the fourier plane and therefore position of the deformable mirror. The deformable mirror is preliminary replaced by a full mirror as the correct positioning is achieved in a different way.

The second relay lens

The position of the second relay lens can now easily be determined using the same procedure. As the tube lens is now bypassed, correct positioning of the second relay lens in a 4f configuration along the reflected optical axis should result again in a collimated output beam, verified using the mentioned shearing plate interferometer.

Positioning of the camera

The illumination path is now switched back to normal EPI illumination and a bead sample is put into focus. The camera can be moved along the optical axis until the beads are in focus, as well on the camera and in the ocular. The 4f system is now correctly set up.

Correct positioning of the deformable mirror

The position of the deformable mirror has to be refined, as the precise positioning in the fourier plane is indispensable. Due to the object side telecentricity the correct position can not be estimated using a collimated input illumination. The fourier plane can be directly observed by inserting a so called *Bertrand* lens between second relay lens and camera. A Bertrand lens is used for alignment as the backfocal planes and their conjugated focal planes can be observed. The position is not absolutely critical. The fourier plane can now be found by moving a distinct target along the optical axis in between the relay system. When the target is in focus the fourier plane is found. The surface of the deformable mirror has to be placed at exactly this position. The crucial part is now to reposition the system "second relay lens - camera" while keeping the distance, as the 4f system has to be maintained.

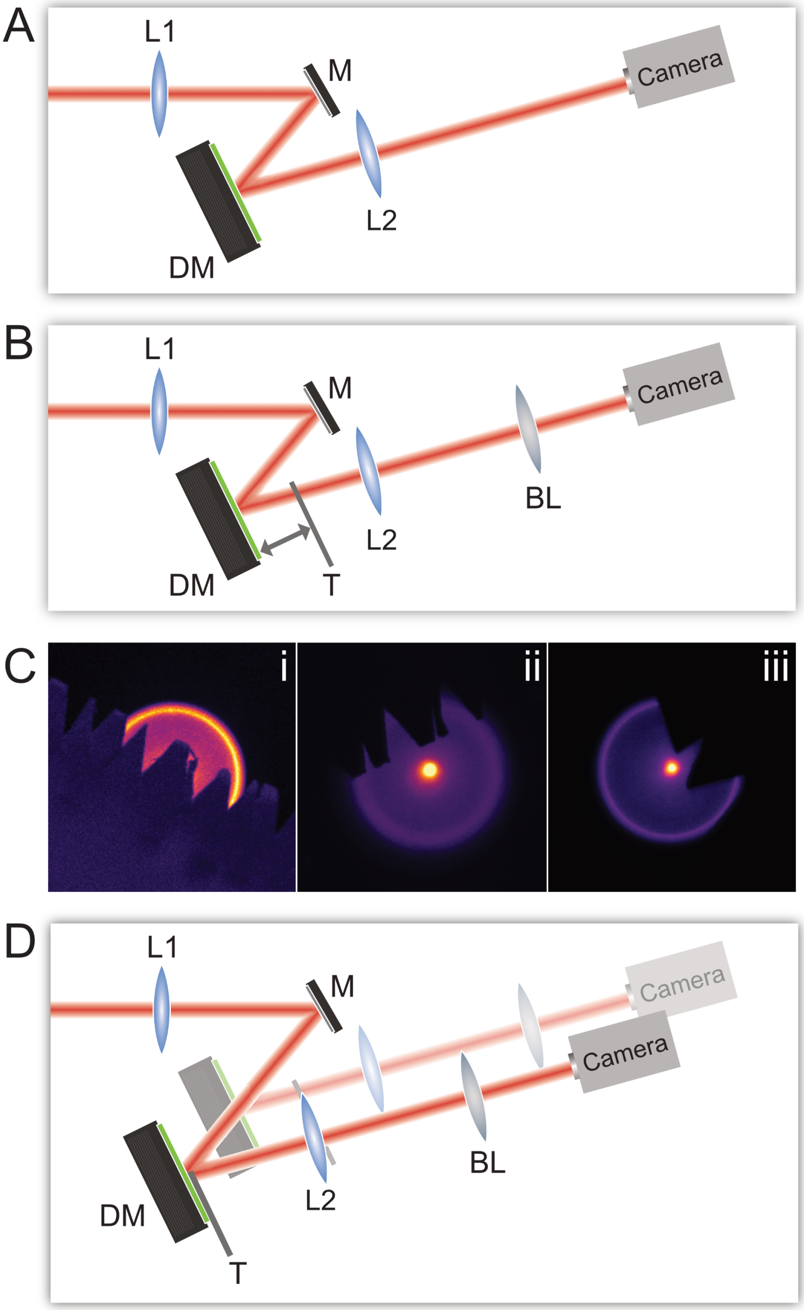

Fig. 3.21 Schematic of beam path and alignment procedure of deformable mirror. **A** The emission light (red ray) is relayed by lenses L1 and L2, and reflexted by a full mirror (M) and the deformable mirror (DM) onto the camera. **B** For precise alignment a bertrand lens (BL) is inserted and a target T is positioned along the detection path to imaged in focus. The position of the target now marks the fourier plane of the relay system. **C** Observation of the fourier plane. **i** Sharp image of fringed target T. **ii** Incorrect positioning of the DM as pupil edge is not imaged sharply. **iii** Correct position of the DM with target T and pupil in focus. **D** Necessary refinement of DM position and relay lens L2-camera system.

3.6.3 Single molecule localisation performance in 2D and 3D

_d_STORM in 2 dimensions

The performance of the detection system with deformable mirror is tested and analyzed by 2D-*d*STORM. An actin staining with phalloidin Alexa Fluor 647 according to protocol 2.2.2 is used as sample. The measurement parameters are selected as follows:

- 2x2 binning of pixels, resulting pixelsize 108nm
- 20ms integration time
- HILO illumination
- 170mW excitation output power of 640nm laser
- Perfect-Focus-System activated
- 50.000 frames total length
- flat field correction pattern applied to deformable mirror

The recorded data were converted into tiff files and processed with the localization software SMAP. A free fit was chosen as fitting algorithm and the localized data was filtered for appropriate PSF FWHM afterwards. The inherent drift during the entire acquisition was corrected by fourier cross correlation, the processing was performed with data segments of 1000 images, i.e. 50000 frames in total were split in 50 reconstructed *d*STORM images. The single molecule data post-processed in this way were loaded for rendering in Thunderstorm and displayed as average shifted histogram with a pixel size of 9 nm in figure 3.22. The used pixel size for rendering resulted in optimal visualisation of small structural features. The rendered data are colored in an inverted mlp-inferno LUT, as the intensity distribution is very inhomogeneous over the whole FOV (panel **A**, *left*) due to the different densities of the structures and therefore a balanced representation is very difficult. The marked inlet is taken from an area with very homogeneous structure and intensity and colored for comparison with gray LUT (top) and inverse (bottom) mpl-inferno LUT.
The quantification of localization precision was performed with an in-house custom made python-based evaluation package provided by Sören Doose. Nearest-neighbour tracking of a localized molecule is performed in consecutive images within a certain radius. Since the emitter density in the image was quite high, the tracking radius was set to 20nm to avoid misallocation. The distribution of the distances between localized emitter positions in consecutive images was analyzed for a total of 5 million localizations. Panel **B** shows

distribution of localisation positions for x (left) and y (right) directions of raw data with additional gaussian fit. The sigma of the resulting gaussian fit divided by square root of 2 results in the localisation precision of approximately 6 nm for both axis. For optimal PSF shape and intensity detection a flat-field correction has been applied to the deformable mirror. The pattern shown in panel **C** has been estimated experimentally.

The performance of the detection path including the deformable mirror with an achieved localisation precision of 6nm approaches the theoretical expectations and enables high quality single molecule measurements.

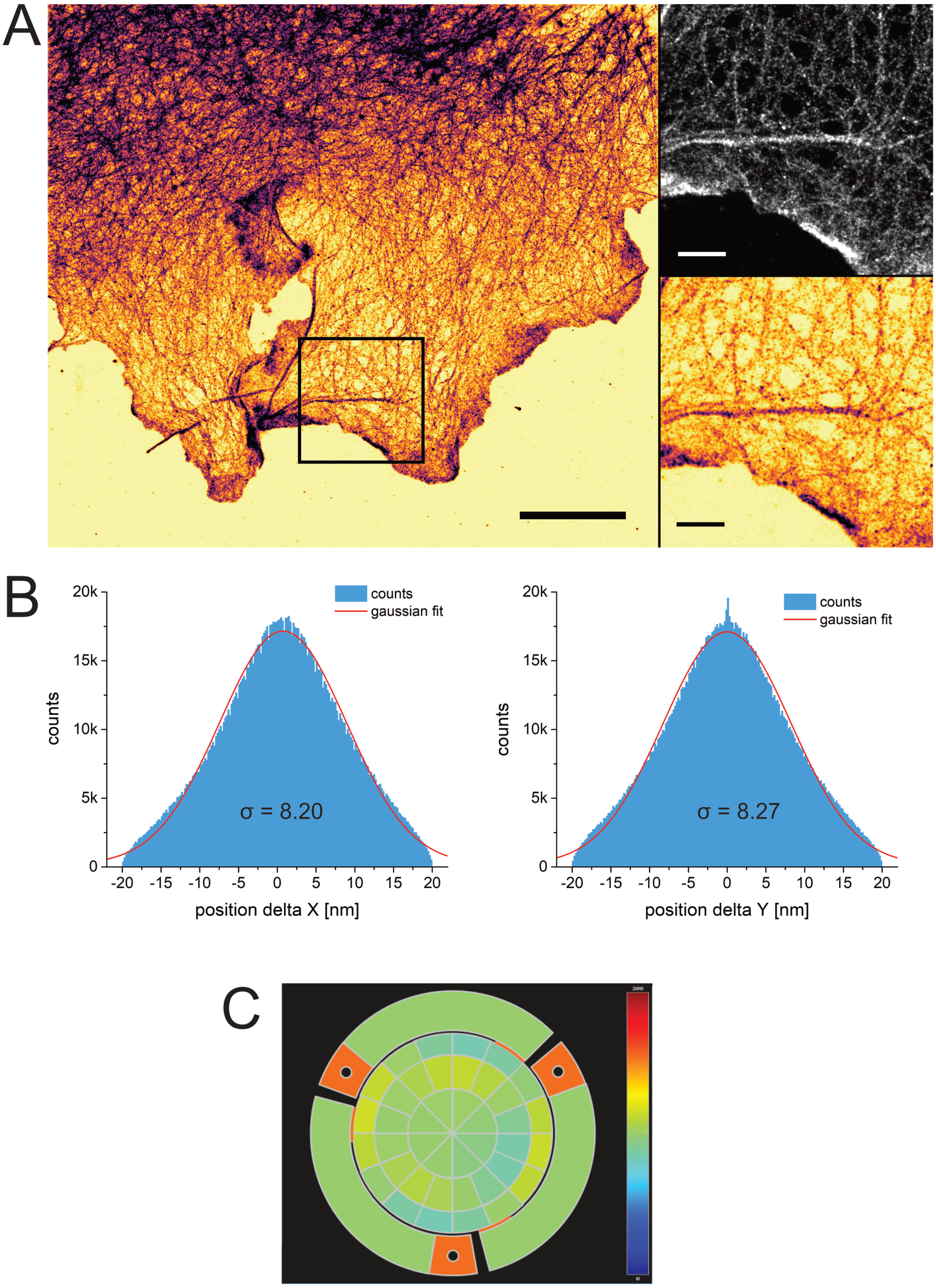

Fig. 3.22 2D-*d*STORM of COS7 cell with actin skeleton staining. **A** *left*: Full imaged field of view visualized with inverted mlp-inferno color LUT. Scale bar 5 µm. *Right:* Inlet shown in original (top) and inverted (bottom) inferno LUT. Scale bars of inlet 1 µm. **B** Localisation precision estimated via nearest-neighbour tracking for x-dimension (left) and y-dimension (right). Gaussian fit to histogram data result in sigma values of 8.20 nm and 8.27 nm corresponding to localisation precisions of approximately 6nm. **C** Flat field correction pattern applied to the deformable mirror for 2D measurements.

*d*STORM in 3 dimensions using astigmatism

In order to decode the z position of the PSF a detection path according to chapter 1.6.3 was installed. Starting from the flat field correction pattern already applied in the previous section 3.6.3 an astigmatism was introduced by modulating the deformable mirror segments. Using sub diffraction bead sample according to protocol 2.2.2 the shape and strength of astigmatism has been experimentally determined. In figure 3.23 A, the lateral view of the astigmatic PSF is shown for 3 focal planes being separated 500 nm apart from each other. The pattern applied to the deformable mirror can be seen in panel B, with color coded voltages for individual segments. The wavefront corresponding to the astigmatism has been calculated using the ZOLA ImageJ plugin and is visualized as color coded 2D image in panel C (top) and 3D model (bottom).

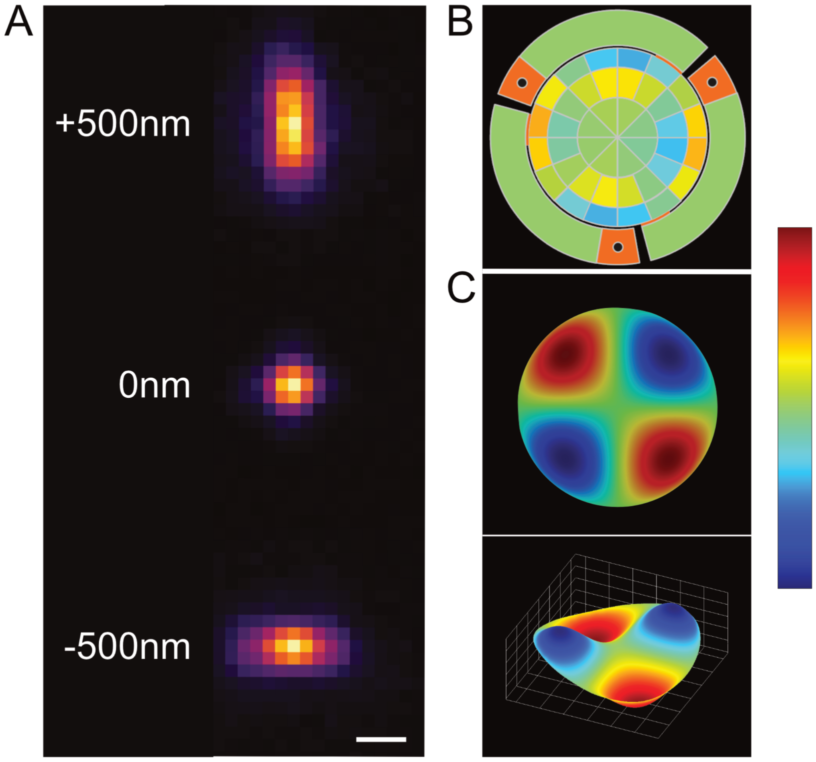

Fig. 3.23 Astigmatic PSF introduced via the deformable mirror. **A** Astigmatism of sub diffraction sized fluorescent bead shown over an axial range of 1000 nm. Scale bar 500 nm. **B** Segment pattern of deformable mirror to create the PSF shown in panel A. Colorbar represents applied voltage from 0 V(blue) to 200 V (red) **C** *top* 2D color coded wavefront estimated from PSF shape in A. *bottom* 3D visualization of wavefront. Colorbar represents amount of deviation from plane wavefront (center color).

The quantitative evaluation of the astigmatic PSF has been performed by the 3D calibration tool of SMAP software. Multiple z-stacks with 25nm z-step size have been acquired in order to average a large number of beads. The resulting calibration curve is shown in figure 3.24 with fitted PSF FWHM in x and y as red dots plotted according to their z position. Solid lines represent spline (blue) and gaussian fit (black) to the data. Axial PSF position differences have been corrected in z using cross correlation. With given astigmatic PSF an axial range of 1200 nm can be decoded.

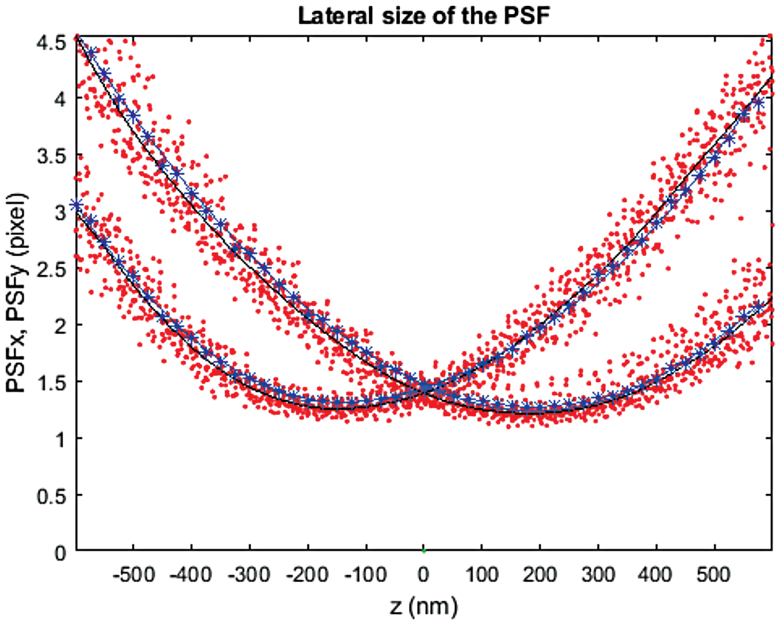

Fig. 3.24 Calibration curve for astigmatism introduced by deformable mirror. Lateral PSF width correlates with axial position of the emitter. Several beads are used for fitting and averaged by SMAP [LMH$^+$18] calibration tool. Red dots represent individual bead data, blue crosses averaged PSFs, solid lines spline (blue) and gaussian (black) fits to data points.

To check the performance of the previously described system with regard to single molecule imaging a staining according to protocol 2.2.2 has been prepared. Calibration curves have been acquired directly before the measurement. The acquisition parameters are as following:

objective 100x/1.49 oil

illumination 170mW, HILO mode

acquisition 20ms integration time, 150.000 frames, activated PFS

Raw data was processed with SMAP using the 3D calibration curves obtained before. Despite all precautions to avoid drift during measurement, including shutting down the air conditioner and avoiding frequent opening and closing of the door to avoid air circulation and vibration, a thorough drift correction of the localized data must be performed. Therefore the internal drift correction of SMAP for the calculation of the lateral drift split the data set into 150 single segments, the axial drift correction in 50nm steps and at 40 points in time. The data corrected in this way were additionally processed with appropriate filters (localization precision, intensity, background) and a track emission was used to merge time-related localizations. The data processed in this way can be seen in figure 3.25 panel A. The color coding represents the z-coordinate ranging from -600 (red) to 600nm (blue) as depicted in the color bar to the right edge of the image. The 3 dimensional alignment of the tubulin filaments is clearly visible. The majority of the tubulin filaments run in the direction of the cell nucleus, which is located outside the upper left edge of the image, in increasing height, but some run close to the basal membrane and thus underneath the cell nucleus. The marked regions are representative of the resolution performance achieved with the used detection system. In the framed boxes, both the lateral views and the orthogonal (axial) sections are shown along dotted lines with 50nm readout width. In box **i** two filaments indicated by the white arrows on the left side are merging not only in lateral but also in axial dimensions. The examples in boxes **ii** and **ii** shows that filaments can be separated which are about 100nm separated axially directly above each other. As the immunostaining contains of a relatively long linker consisting of two IgG antibodies the linkage error is quite large. In rare cases a hollow cross-section of the tubulin filaments can be found. In the examples **iv** and **v** this can be clearly seen in the axial views.

The evaluation of the localization precision is a very valuable piece of information because it correlates directly with the detected intensities of the individual localizations. This allows direct conclusions to be drawn as to whether the aperture of the deformable mirror is over-illuminated or well illuminated and reflects all photons in the direction of the camera. For the evaluation, only the drift correction described above is applied to the data. For the analysis with the Python package Surepy a laterally and axially separate processing is performed because the tracking radii should not be isotropic. For the tracking of the localizations relative to the center of gravity for the lateral distribution a tracking radius of 30 nm was chosen, for the axial distribution 70nm. The localization precision is calculated from the gaussian fit to the distributions using the sigma values divided by $\sqrt{2}$. The localization precision results for X with 8 nm, Y 7 nm and Z 24 nm. Overall the precision is almost isotropic in lateral dimensions and 1-2 nm worse than flat-field corrected 2D-*d*STORM imaging as described in 3.6.3. The localisation precision axial direction is intrinsically lower due to the distribution of photons in the distorted PSF shape. With a calculated value of 24 nm one lies in the expected range of a 3 times worse localization precision in axial direction.

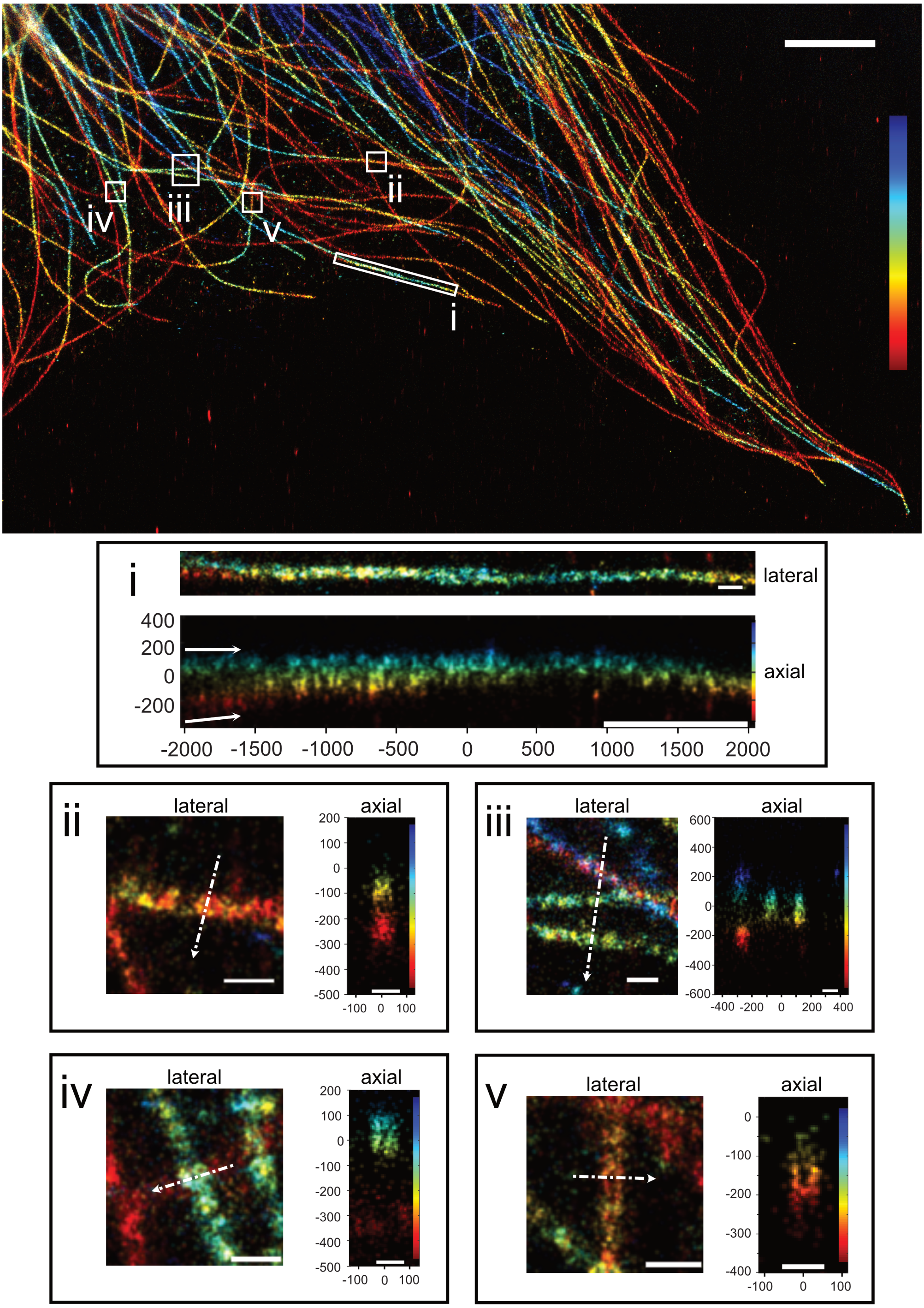

Fig. 3.25 Super resolved 3D-*d*STORM image of tubulin using astigmatism. The color code represents the axial position in a range of 1.2 µm. Inlets display lateral view and axial view along dashed arrows. Scale bar top 3 µm, scale bar inlets 300 nm.

3.7 Correlative imaging RCM and *d*STORM

In the following section, both imaging techniques are used to capture the same field of view and align it structurally, to evaluate the correlation of both images and to work out the direct comparison of the techniques.

3.7.1 Correlative imaging in 2 dimensions

First correlative imaging experiments were performed in 2 dimensions. The microscope setup was equipped with the RCM detection and a separate 2D detection path with an Andor IXON EMCCD camera (iXON 897).

An ideal sample for initial correlation and comparison of structural resolution is the microtubule network. COS7 cell were stained according to protocol 2.2.2. Switching buffer was added to the sample and imaging performed as following:

1. a single slice widefield image was acquired
2. a z-stack in RCM was acquired
3. 60000 frames in HILO configuration and activated PFS system were acquired

The single molecule analysis was carried out using the SMAP software citeLi.2018. Localisations were fitted with free PSF model and later filtered with suitable values for PSF FWHM. Drift correction was applied using fourier-cross-correlation for sub stack frame lengths of 1000 frames. The resulting localisation table was exported and converted to a format readable by Thunderstorm for data reconstruction. The image was rendered with a final pixel size of 6.8 nm. Localisation precision was calculated with the python package Surepy using 30 nm tracking radius. The localisation precision yields for x and y dimensions a value of 8 nm.

All images had to be registered, even the wide field image as it was acquired at full chip field of view, whereas the field of view for single molecule imaging was cropped for optimal laser power density and switching behaviour of the dyes. The registration was performed in MATLAB with the internal registration estimator. This estimator has several modalities for registration, in this case an intensity based registration performs best. As the images were acquired on two different optical paths and the different detectors, the multimodal intensity based registration is chosen. Different transformation types can be selected, similarity or affine transformation give best results. As fix image the reconstructed *d*STORM image should always be set, as it contains the highest resolution and alignment of lower resolution images minimizes the error of registration. Registration of widefield and RCM image to the super resolved *d*STORM image is carried out and images exported for further processing.

To quantify and visualize the structural correlation especially in RCM and *d*STORM the registered images were analysed using the SQUIRREL plugin [CAJ$^+$18].

In figure 3.26 the entire *d*STORM image is shown in the top left panel with a framed ROI (i) for zoomed in versions in the top right panels. The same area is shown for *d*STORM and RCM image, a cross-sectional profile has been read out along the indicated yellow line. The widefield image is not shown as the imaging mode has no further gain. The overlay in inlet i of the registered RCM and *d*STORM image is shown in the bottom left panel. For better visualization of the correlation the color LUTs have been set to magenta (RCM) and cyan (*d*STORM). The panel to the right is displaying the error map created by SQUIRREL, color coding regions of dissimilarity according to the added color bar with increasing error from bottom to top. For single filaments the similarity is quite high, as soon as filaments start to run in closer distances the error of correlation increases significantly. The validation metric of SQUIRREL contains a Resolution Scaled Error (RSE) and a Resolution Scaled Pearson (RSP) coefficient. As described in detail in [CAJ$^+$18], the RSE describes the intensity distances of the correlated images. This results in a high sensitivity to brightness and contrast differences of the images. The RSP measurement with values between -1 and 1 is based on the normalized correlation of the intensity distances to the mean value of the respective images. With an RSE value of 11.4, the deviation of the non-normalized intensity distances of both images is relatively small (in comparison the RSE of widefield-*d*STORM : 5735). This may be due to the improved resolution of the RCM and the z-sectioning of the confocal system. The RSP value is 0.914 (wide field - *d*STORM: 0.034) and gives a relatively high similarity at normalized intensity distances. Error in empty areas between filaments results from imaging modalities as the RCM imaging is based on intensity detection sensitive to background whereas *d*STORM is reconstructed from single molecule PSFs only.

Line profiles according to figure 3.26 inlets i for all imaging modalities are fitted with a gaussian function and the FWHM is listed in table 3.10. The resolution improvement of *d*STORM is almost one order of magnitude, the RCM reveals a 60% better confined FWHM compared to the widefield. It has to be mentioned that comparisons between the imaging modalities are critical. As axial resolution of all techniques is ranging from around 40 nm to 500 nm setting the exact same focal plane remains challenging.

Table 3.10 Comparison between Widefield, RCM and *d*STORM imaging concerning the FWHM of the same tubulin filament.

Imaging modality	FWHM [nm]
Widefield	389 ± 26
RCM	237± 6
dSTORM	45± 1

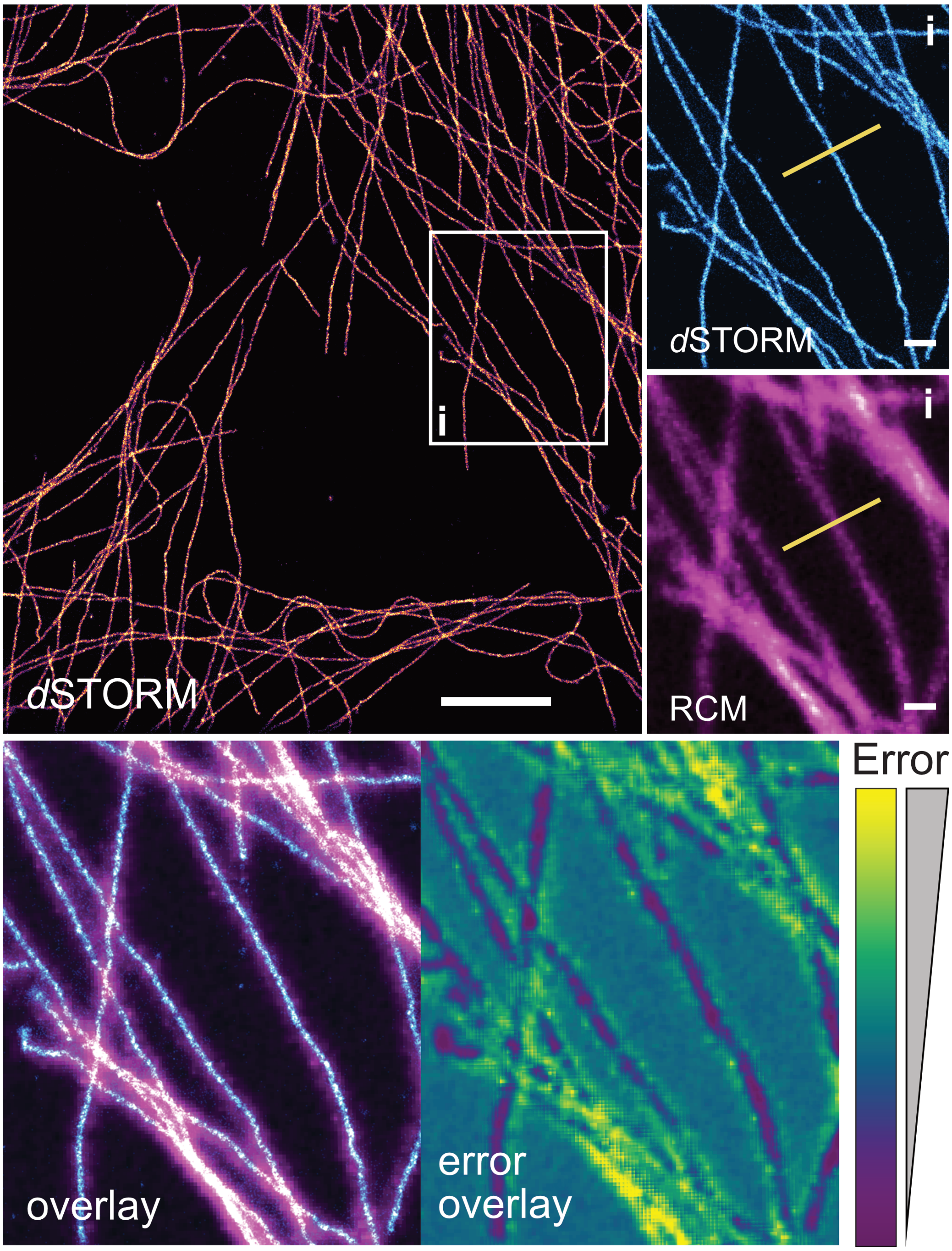

Fig. 3.26 Correlative imaging in 2 dimensions of tubulin filaments acquired with RCM and *d*STORM. **Top left** 2D *d*STORM image as representative for correlative imaging. ROI marked for zoomed views. Scale bar 3 µm. **Top right** Zoomed region displaying registered RCM and *d*STORM area. At indicated yellow bars line profiles were taken for further analysis. FWHM of the tubulin filament are calculated by gaussian fits. Values are for *d*STORM 45± 1 nm, for RCM 237±6 nm and for wide field 389 ± 26 nm. Scale bars for inlets 500nm. **Bottom** Overlay of registered RCM and *d*STORM images is shown in magenta (RCM) and cyan (*d*STORM) LUTs. Estimated error in resolution of both registered images estimated with imageJ plugin SQUIRREL is displayed in the right image. Magnitude of correlative structural error between the images is quantified and color coded in the bar to the right edge.

3.7.2 Correlative imaging in 3D

In the following section, an example of the 3D correlation of both imaging techniques will be evaluated. The 3D-*d*STORM image shown in figure 3.25 was additionally captured with the RCM in the form of a z-stack with z intervals of 200 nm. The images are processed using the super-resolution correlator [Rei18]. By registering the localization data on the RCM images projected in 2D a Pearson correlation index of 0.77 is achieved, which indicates a high correlation of structures in both imaging techniques although resolution differs almost 10 fold. The approach is justified as the axial resolution of the RCM with around 500 nm has to be seen in the context of the axial range of 1200 nm covered by an astigmatic PSF.
A qualitative evaluation of the correlation with the Fiji tool SQUIRREL is not possible in this case, as it is only designed for 2D data sets. The assembly in figure 3.27 (top) shows the z-color coded images over an axial span of 1200 nm. The RCM was mounted in the same way as the RCM. In the lower row the axial resolution of both techniques is compared by two filaments running on top of each other. In the side view of the 3D-*d*STORM image the filaments can be clearly separated from each other, whereas in the RCM image the filaments fuse together. The axial distance of approx. 160 nm is clearly below the resolution limit of the RCM. The 3D image by means of RCM on the other hand is also possible in all 4 excitation channels and thus allows an easy assignment of the target structure in volumetric orientation. The calibration for 3 dimensional single molecule localisation imaging has to be checked for each measurement and the measurement therefore implies an increased expenditure of time. Nevertheless, the calibration can be optimized via the control software of the deformable mirror as opposed to the extremely sensitive adjustment of a lens system.

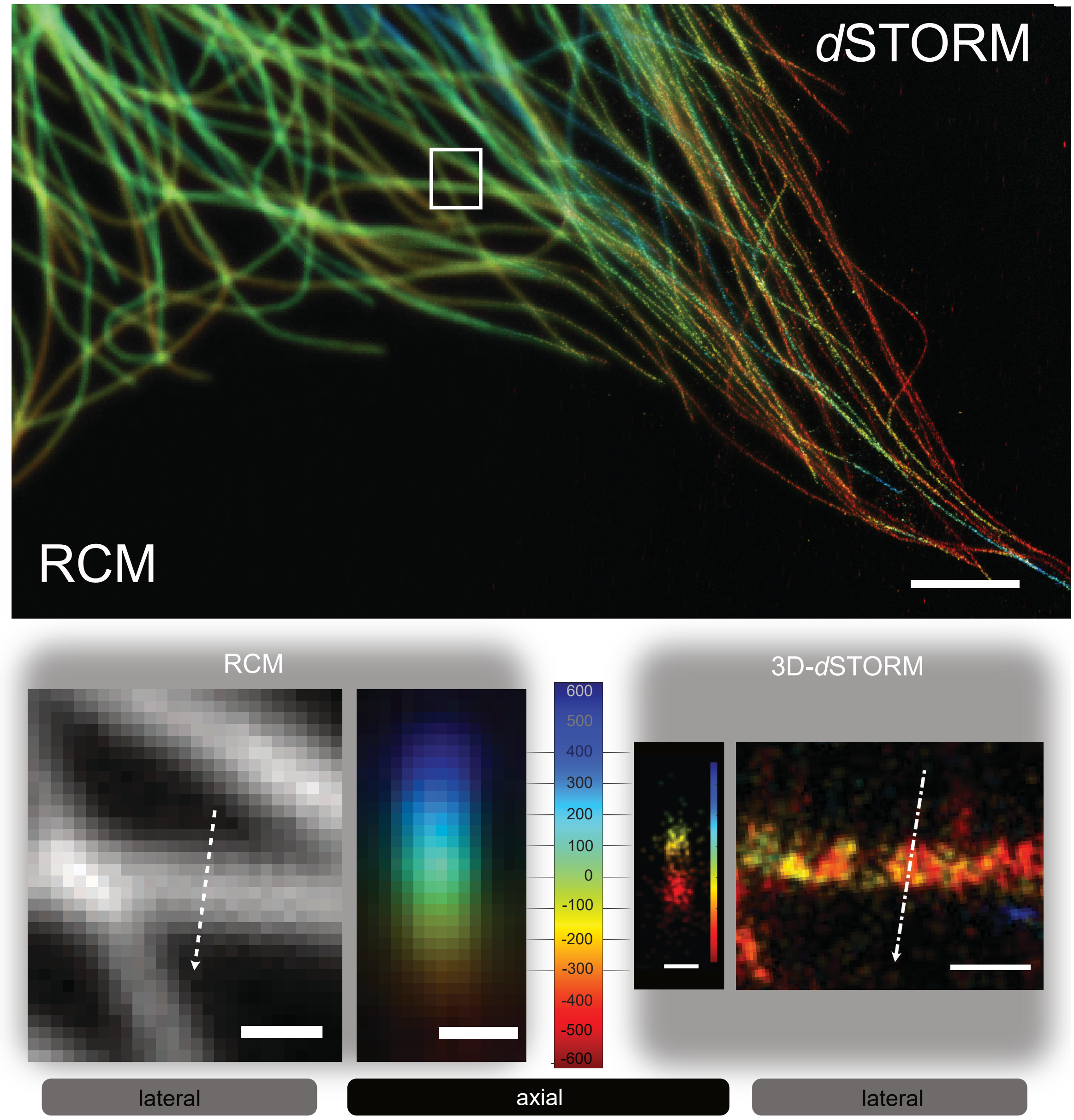

Fig. 3.27 Correlative 3D imaging with RCM and *d*STORM. **Top**. Depth color coding of RCM z-stack projection and 3D-*d*STORM single molecule localisation of microtubules. Scale bar 3 µm. **Bottom**. Comparison of axial resolution using structure in boxed region. Lateral views of both techniques are shown at each side. Dashed arrows indicate the location of the correlated axial view depicted in the center images. Double filaments resolvable in 3D-*d*STORM are fused and blurred in the 3D-RCM stack. The color bar in the center has an axial range of 1200 nm, the *d*STORM image has its own color coding due to the different resolution. However, the z-values correlate directly. Lateral scale bars 300 nm, axial scale bars 300 nm (RCM) and 100 nm (*d*STORM).

3.7.3 Correlative live-to-fixed cell superresolution imaging

To combine dynamic live cell imaging with on-the-fly-fixation, followed by immunostaining and correlative RCM-*d*STORM imaging turned out to be challenging. The procedure included time lapse imaging of HeLa EB1-YFP signals, fixation according to protocol 2.2.2 and immunostaining of α-tubulin. After addition of the switching buffer, a z-stack was recorded by RCM, followed by 150.000 frames acquisition for single molecule reconstruction. In figure 3.28 the results are summarized. Panel **A** displays the EB3-YFP track in color code over the entire length of 210s time lapse acquisition. In panel **B** the RCM z-stack is shown as color coded image according to the color bar displayed in the image top right. The marked inlet is shown in **C** as single plane RCM image (left) and *d*STORM reconstruction (right). Analysis of single molecule raw data has been performed with SMAP and includes drift correction and localization filtering. Surepy was used to evaluate the localization precision resulting in 6 nm. The marked region is shown in the bottom row for RCM (i), *d*STORM (ii), merged overlay (iii) of RCM in cyan and *d*STORM in magenta. Similarity of correlated images is visualized by SQUIRREL error map in the last panel (iv) with RSE value of 7955 and RSP value of 0.708. The super-resolution images clearly show that the tubulin filaments are not continuously marked, whereas the RCM images show almost complete filaments. These labelling artefacts are probably caused by blocking the tubulin epitopes of end binding proteins. For example, the β-tubulin cannot be labelled at all with a (positively tested) β-antibody, the $alpha$-tubulin obviously only incompletely in contrast to images shown in figure 3.25 where the same antibody and staining protocol has been used. The incomplete labelling can be found throughout the entire treated sample, but for these cells it is no longer possible to say how advanced the expression of the EB1 protein was in the live cell state before. Many cells express the protein to a degree that the comet-like signal is well detectable, but many cells show an overexpression which only results in tubulin filaments labelled with EB1-YFP. The interference due to the expressed protein with succeeding labelling as well as the visualisation with correlative techniques might give the set up system an additional value.

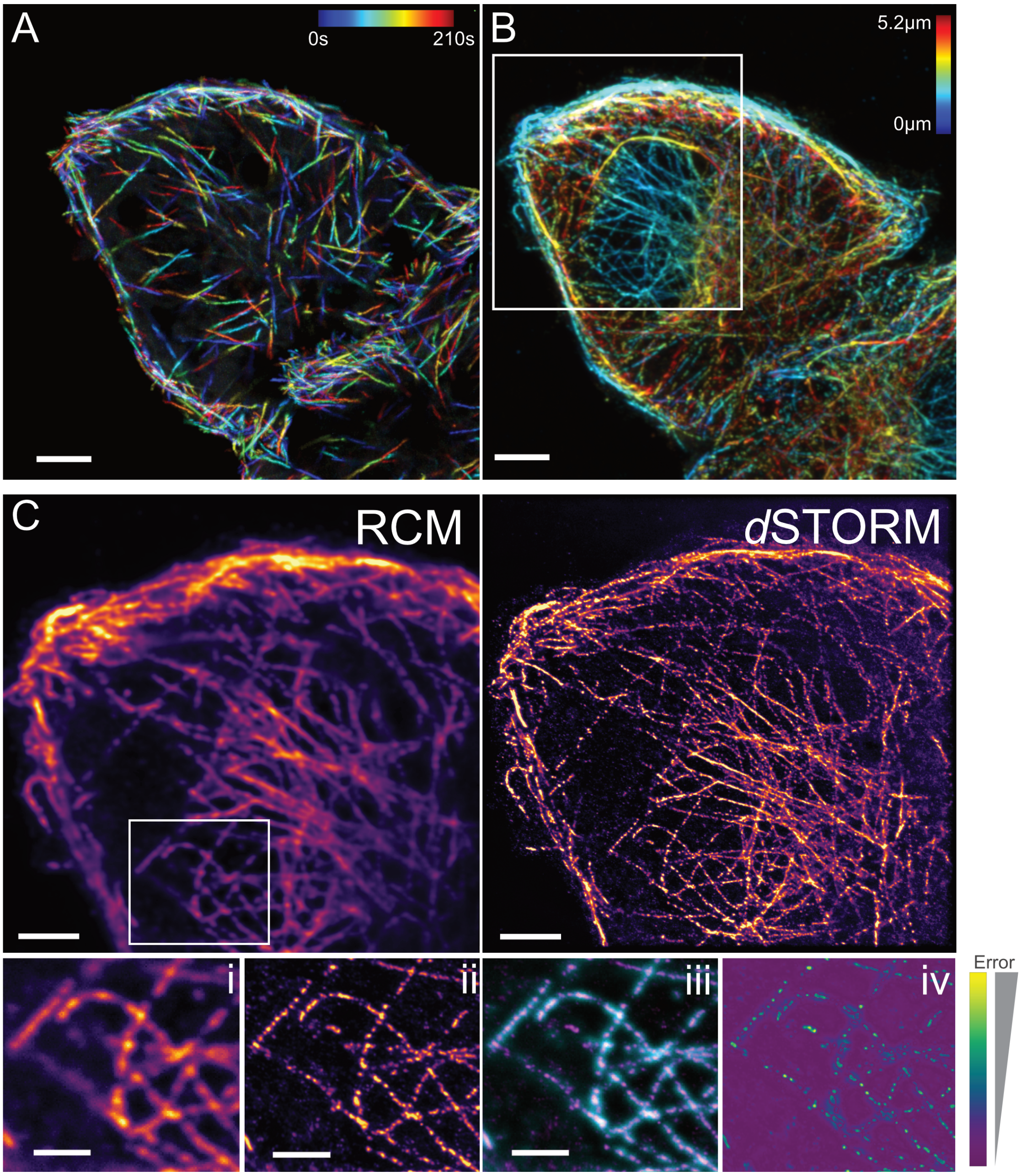

Fig. 3.28 HeLa cells with stable expression of end binding protein EB1-YFP, fixed on the fly and added immunostaining of α-tubulin with Alexa Fluor 647. **A** color coded time traces of EB1-YFP signal imaged with the RCM over 210s followed by on-the-fly fixation and immunostaining of α-tubulin. Scale bar 5µm **B** Color coded z-projection of α-tubulin imaged with the RCM. Scale bar 5µm. Inlet marked for **C**. Single RCM frame where 2D-*d*STORM-imaging has been performed. Scale bar 5µm. Inlet is shown for RCM (**i**, contrast increased) and 2D-*d*STORM-image (**ii**). In panel **iii** the overlay of the RCM channel (cyan) and the *d*STORM channel (magenta) is displayed as well as the overlay error in **iv** analyzed by SQUIRREL with indicated structural error bar next to the panel. Scale bars 3µm.

Chapter 4

Conclusion and Outlook

With ever more complex scientific investigations, the demands on imaging techniques in terms of resolution, speed and life cell compatibility are also increasing. The pool of different imaging technologies has grown rapidly in recent years and offers commercial as well as freely accessible blueprints for various devices and structures. Nevertheless, none of the techniques combine the three parameters resolution, speed and living cell compatibility at maximum possible extent. A great overview has been given by Hari Shroff in nature methods *Perspectives* [WS18], where super resolution techniques based on structured illumination are compared in several aspects. The wide spread in ranking of the individual techniques concerning lateral and axial resolution, imaging speed, depth and required excitation laser power indicates the difficulty of choice for certain demand of investigations. With the interplay of complementary imaging techniques, many technical limitations can be circumvented and new experimental possibilities created.

The rescanning confocal microscope (RCM) as commercial image scanning based system combines the section capability of the confocal microscope with improved resolution and reduced photo bleaching. The scanning unit has been successfully integrated into an existing system and extensively tested and characterized for resolution, speed and phototoxicity. The lateral resolution improvement of 170 nm at 488 nm excitation wavelength was achieved as specified. Axially, a clear improvement of the resolution could be determined contrary to the manufacturer's specifications. Furthermore, the resolution was determined wavelength dependent and a comparison between rescanning and confocal scanning mode was made. The clear influence of the chromatic aberration of the detection system with a displacement of up to 300nm regard the axial position was quantified and corrected by software.
The resolution improvement was demonstrated on fluorescent beads as well as on fluorescently stained cellular structures by comparing the two scanning modes. The resolution

improvement by the optomechanical magnification and the associated pixel reassignment is enhanced by the double sampling rate regarding the pixel size. The live cell applicability was analysed using the dynamic EB1 signal. The stably expressed protein reacts very sensitively to external influences such as laser irradiation. By means of a long time lapse recording with continuous recording, the photo bleached protein could be quantified and the influence of the laser excitation on the dynamics of the fluorescent proteins could be determined. The calculated decay time of about 1700 s on half of the signal as well as the nearly unchanged speed of the EB1 signals indicates an extremely low influence of the illumination and a very low phototoxicity. Decisive factors for this are the high quantum efficiency of the camera, which allows significant reduction of the excitation power with sufficient signal to noise ratio. The laser power was calibrated and the detection path was equipped with a neutral density filter, enabling extremely low and at the same time stable laser power.

The high quantum efficiency of the camera also allows single molecule sensitive detection. Using the confocal scanning mode, single SeTau dye molecules could be detected with an average of about 60 photons in the PSF pixels. Compared to a conventional PMT-based confocal microscope, the RCM offers a completely new application possibility. In expansion microscopy, for example, where 10-fold mechanical magnification of cellular structures is now possible, the spatial separation of fluorescent dyes tends to become so far that individual molecules can be detected separately. In this case, the low quantum efficiency of a PMT detector reaches the detection limit.

The laser system used is a prototype of the Skyra multiline laser. The special feature and therefore also the selection criterion of this laser was its compact and maintenance-free design. This eliminates the need for readjustment of optical components and guarantees reliable performance. The integration of all devices and components into the control software NIS Elements and the configured user interface allows 4 channel imaging, 3D resolution and display as well as time lapse and multi point experiments in various combinations.

The single molecule detection system was extended during the doctoral thesis and equipped with an adaptive optic device as being published by Aristov and Lelandais recently in 2018 [ALRZ18]. The deformable mirror allows modulation of the wavefront and thus adaptive shaping or correction of the point spread function. The installed system was analyzed and quantified for performance during 2D *d*STORM measurements. The achieved localization precision of approx. 6-7 nm and lateral resolution quality are excellent. Furthermore, a pattern for astigmatic deformation of the PSF was determined experimentally, which allows decoding of the z-dimension in single molecule based imaging. The performance has been evaluated in 3D-*d*STORM imaging of microtubuli staining with superb feature detection like hollow filaments. Localisation precision in 3D is in lateral dimensions comparable to the 2D performance, in axial direction in the expected range of 3 fold lower precision values. The sophisticated saddle-point PSF shape as demonstrated in the before mentioned publication has been successfully generated. Due to the lack of required laser power for inducing homogeneous photo switching over an axial range of more than 2 µm no single molecule imaging has been performed using this saddle-point PSF shape. As a member of the Research Training Group 2157 focusing on tissue models for infection studies, an adaptive system of this type offers great potential for single molecule localization microscopy. Since tissue scattering and associated aberrations strongly deform PSF, single molecule analysis will always be flawed if not impossible. An adaptive correction depending on the tissue condition is inevitable as demonstrated by *Mlodzianoski* imaging up to 200 µm thick brain sections [MCHB$^+$18]. An automated correction can be implemented by means of a wavefront sensor, whereby the flat field correction can be used instantaneously for 2D measurements. The necessary deformation for astigmatism or more complex PSF can then be modulated onto this pattern. A master student has already been supervised to start implementation of a Shack-Hartmann wavefront sensor into the current detection path.

Correlative imaging between RCM and *d*STORM was performed and quantified in both 2D and 3D. On the one hand, methodological basics were tested such as alignment of the images to be correlated by different software and quantification of structural similarity. The two imaging techniques have been compared by imaging the same structure within the same field of view. The almost 10 fold higher resolution of *d*STORM can be impressively visualized, in 2D as well as in 3D. Nevertheless only a couple of synthetic fluorophores are suitable for optimal photo switching.The combination of a multi-channel confocal system with a single molecule super resolution technique proves to be a powerful tool for placing the structures to be investigated in a meaningful context. A correlative approach has been presented by *Crossman* using confocal and single molecule techniques, but performed on two separate devices and correlated afterwards. Measurements with the presented setup allow a direct correlation of the same field of view, which brings considerable advantages regarding subsequent processing.

The correlation of both imaging techniques was quantified using identical structures and thus the distinctive features were also clarified. In 2D, the ImageJ plugin SQUIRREL can be used to generate a structural resolution error map. In 3D the correlation with the super-resolution correlator [Rei18] developed by Sebastian Reinhardt at the department of biotechnology has been performed. The two techniques differ in resolution by almost an order of magnitude. Often SMLM resolution is not necessary and furthermore requires in most cases optimization of sample preparation steps like fixation protocol and highly specificity of the labeling itself.

For initial characterisation and high quality imaging the RCM provides an easy to use and very reliable tool. In case the highest spatial resolution is required for a specific problem, the correlative system offers a perfect complementary technique with single molecule localisation microscopy.

A microfluidic pump system was installed to extend the application possibilities of the imaging techniques. For the control of the pump system a graphical user interface was programmed and equipped with different commands for various pump protocols. Basic experiments were tested on both living and fixed cells. These included live fixation followed by various staining protocols, live cell staining and buffer exchange. Different commercially available sample chambers were evaluated as well as a custom made solution optimized for the application. With this system decisive dynamics can be frozen at key time points and allow to extract further spatial resolution for quantification by applying super resolution techniques.

First approaches have been made to generate more **advanced PSFs** using the deformable mirror and extend the axial range. The saddle point PSF shape has been achieved with suitable deformable mirror settings. Single molecule imaging his highly challenging using this PSF concerning following points:

lateral extent of PSF the wide distribution of emitter intensity requires very low densities of single molecule signals to avoid any overlapping PSFs. In addition, background signal from adjacent levels seems to strongly influence the detectability of complex PSF. Optimal sample preparation to reduce unspecific staining seems to be essential. A suitable switching rate of the dyes is also necessary, which in turn has sufficient laser power as a consequence.

axial range of the PSF The large axial range of more than 2µm places further demands on the excitation illumination. While in 2D or astigmatism the power density can be achieved by a HILO configuration, an EPI illumination is necessary for this axial range. With a given laser power, the illuminated area must be greatly reduced in order to obtain sufficient power density and thus induce high switching rates. The existing 170mW of the red (640 nm) laser are clearly too low for this.

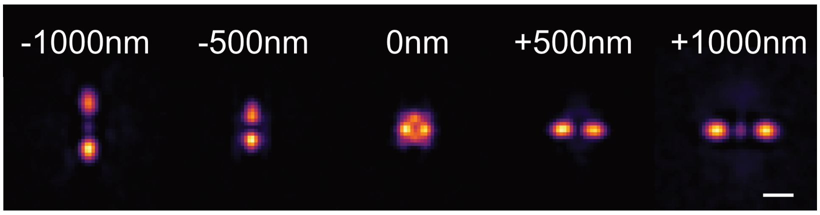

Fig. 4.1 Saddle-point Point-Spread-Function at different axial focal planes 500 nm apart. The entire decodable axial range covers around 2µm. Scale bar 1 µm.

Upgrading the system with a high power laser of at least 500 mW is required to get sufficient power density and photo switching. The attempt to overlay two 170 mW diode laser via cross polarization resulted in interference stripes in the illumination area. A single high power laser is definitely the better choice.

The implementation of a Shack-Hartman wavefront sensor in feedback loop to the deformable mirror has been started in the end of this thesis and will be continued by a master student. The first goal using the active correction of the wave front should be single molecule imaging in deep tissue or brain slice samples. The performance of the silicon immersion oil objective has to be evaluated as the refractive index is matched better to inhomogeneous samples like tissue. The numerical aperture is slightly lower than the immersion oil objective, but the amount of deformation might should turn out far lower. Moreover 3D single molecule imaging has to be implemented, with as much automated correction as possible. Sample preparation of tissue slices is highly critical, therefore optimizing tissues for 3D calibration procedures might be extremely time consuming. The current system is the first adaptive optics system of the departments single molecule microscope portfolio and has not even reached its full potential. With a growing application of tissue models to mimic more realistic environments these technique could prove to be highly valuable in future research projects.

References

[Abb81] E. Abbe. Vii.-on the estimation of aperture in the microscope. *Journal of the Royal Microscopical Society*, 1(3):388–423, 1881.

[AFW19] AFW Technologies. Pm patchcord, 18.02.2019.

[ALRZ18] Andrey Aristov, Benoit Lelandais, Elena Rensen, and Christophe Zimmer. Zola-3d allows flexible 3d localization microscopy over an adjustable axial range. *Nature communications*, 9(1):2409, 2018.

[And19] Andor. ixon emccd camera series - andor - oxford instruments: Scientific cameras, 2019.

[AS13] Milton Abramowitz and Irene A. Stegun, editors. *Handbook of mathematical functions: With formulas, graphs, and mathematical tables*. Dover books on mathematics. Dover Publ, New York, NY, 9. dover print.; [nachdr. der ausg. von 1972] edition, 2013.

[BKK$^+$19] Gerti Beliu, Andreas J. Kurz, Alexander C. Kuhlemann, Lisa Behringer-Pliess, Mara Meub, Natalia Wolf, Jürgen Seibel, Zhen-Dan Shi, Martin Schnermann, Jonathan B. Grimm, Luke D. Lavis, Sören Doose, and Markus Sauer. Bioorthogonal labeling with tetrazine-dyes for super-resolution microscopy. *Communications Biology*, 2(1):261, 2019.

[BLB$^+$13] Mikael P. Backlund, Matthew D. Lew, Adam S. Backer, Steffen J. Sahl, Ginni Grover, Anurag Agrawal, Rafael Piestun, and W. E. Moerner. The double-helix point spread function enables precise and accurate measurement of 3d single-molecule localization and orientation. In Jörg Enderlein, Ingo Gregor, Zygmunt K. Gryczynski, Rainer Erdmann, and Felix Koberling, editors, *Single Molecule Spectroscopy and Superresolution Imaging VI*, SPIE Proceedings, page 85900L. SPIE, 2013.

[BMW18] BMW AG 2018. Adaptives xenon-kurvenlicht, 2018.

[Boo14] Martin J. Booth. Adaptive optical microscopy: the ongoing quest for a perfect image. *Light: Science & Applications*, 3(4):e165–e165, 2014.

[BPS$^+$06] Eric Betzig, George H. Patterson, Rachid Sougrat, O. Wolf Lindwasser, Scott Olenych, Juan S. Bonifacino, Michael W. Davidson, Jennifer Lippincott-Schwartz, and Harald F. Hess. Imaging intracellular fluorescent proteins at nanometer resolution. *Science (New York, N.Y.)*, 313(5793):1642–1645, 2006.

[Bra00] Ronald Newbold Bracewell. *The Fourier transform and its applications*. McGraw-Hill series in electrical and computer engineering. McGraw Hill, Boston, Mass., 3. ed., internat. ed. edition, 2000.

[BW54] A. B. Bhatia and E. Wolf. On the circle polynomials of zernike and related orthogonal sets. *Mathematical Proceedings of the Cambridge Philosophical Society*, 50(1):40–48, 1954.

[CAJ+18] Siân Culley, David Albrecht, Caron Jacobs, Pedro Matos Pereira, Christophe Leterrier, Jason Mercer, and Ricardo Henriques. Quantitative mapping and minimization of super-resolution optical imaging artifacts. *Nature methods*, 15(4):263–266, 2018.

[CLW+14] Bi-Chang Chen, Wesley R. Legant, Kai Wang, Lin Shao, Daniel E. Milkie, Michael W. Davidson, Chris Janetopoulos, Xufeng S. Wu, John A. 3rd Hammer, Zhe Liu, Brian P. English, Yuko Mimori-Kiyosue, Daniel P. Romero, Alex T. Ritter, Jennifer Lippincott-Schwartz, Lillian Fritz-Laylin, R. Dyche Mullins, Diana M. Mitchell, Joshua N. Bembenek, Anne-Cecile Reymann, Ralph Bohme, Stephan W. Grill, Jennifer T. Wang, Geraldine Seydoux, U. Serdar Tulu, Daniel P. Kiehart, and Eric Betzig. Lattice light-sheet microscopy: imaging molecules to embryos at high spatiotemporal resolution. *Science (New York, N.Y.)*, 346(6208):1257998, 2014.

[Con19] Confocal.nl. Rescanning confocal microscope unit (1.1): Improve your imaging experience, 2019.

[CTB15] Fei Chen, Paul W. Tillberg, and Edward S. Boyden. Optical imaging. expansion microscopy. *Science (New York, N.Y.)*, 347(6221):543–548, 2015.

[CWS16] Longchao Chen, Yuling Wang, and Wei Song. Super–resolution confocal microscopy through pixel reassignment. In Stefan G. Stanciu, editor, *Microscopy and Analysis*. InTech, 2016.

[DBB+13] De Luca, Giulia M R, Ronald M. P. Breedijk, Rick A. J. Brandt, Christiaan H. C. Zeelenberg, Babette E. de Jong, Wendy Timmermans, Leila Nahidi Azar, Ron A. Hoebe, Sjoerd Stallinga, and Erik M. M. Manders. Re-scan confocal microscopy: scanning twice for better resolution. *Biomedical optics express*, 4(11):2644–2656, 2013.

[Edm19] Edmund Optics Inc. The advantages of telecentricity | edmund optics, 2019.

[Ell52] M. W. Ellison. Why do stars twinkle? *Irish Astronomical Journal*, 2:5, 1952.

[FH03] M. H. Freeman and C. C. Hull. *Optics*. Butterworth-Heinemann, Edinburgh, 11th ed. edition, 2003.

[FST08] Marta Fernández-Suárez and Alice Y. Ting. Fluorescent probes for super-resolution imaging in living cells. *Nature reviews. Molecular cell biology*, 9(12):929–943, 2008.

[FSv16] Christian Franke, Markus Sauer, and Sebastian van de Linde. Photometry unlocks 3d information from 2d localization microscopy data. *Nature methods*, 2016.

[GACR18] Rafael G. González-Acuña and Héctor A. Chaparro-Romo. General formula for bi-aspheric singlet lens design free of spherical aberration. *Applied optics*, 57(31):9341–9345, 2018.

[GAE98] Gerard Drewes, Andreas Ebneth, and Eva-Maria Mandelkow. Maps, marks and microtubule dynamics. *Trends in biochemical sciences*, 23(8):307–311, 1998.

[GALS$^+$18] Inna Goliand, Shai Adar-Levor, Inbar Segal, Dikla Nachmias, Tali Dadosh, Michael M. Kozlov, and Natalie Elia. Resolving escrt-iii spirals at the intercellular bridge of dividing cells using 3d storm. *Cell reports*, 24(7):1756–1764, 2018.

[Gar15] Rob Garner. About the hubble space telescope, 2015.

[GAU$^+$19] Ruixuan Gao, Shoh M. Asano, Srigokul Upadhyayula, Igor Pisarev, Daniel E. Milkie, Tsung-Li Liu, Ved Singh, Austin Graves, Grace H. Huynh, Yongxin Zhao, John Bogovic, Jennifer Colonell, Carolyn M. Ott, Christopher Zugates, Susan Tappan, Alfredo Rodriguez, Kishore R. Mosaliganti, Shu-Hsien Sheu, H. Amalia Pasolli, Song Pang, C. Shan Xu, Sean G. Megason, Harald Hess, Jennifer Lippincott-Schwartz, Adam Hantman, Gerald M. Rubin, Tom Kirchhausen, Stephan Saalfeld, Yoshinori Aso, Edward S. Boyden, and Eric Betzig. Cortical column and whole-brain imaging with molecular contrast and nanoscale resolution. *Science (New York, N.Y.)*, 363(6424), 2019.

[GE19] Ingo Gregor and Jörg Enderlein. Image scanning microscopy. *Current opinion in chemical biology*, 51:74–83, 2019.

[Geo35] George Bidell Airy. On the diffraction of an object-glass with circular apertur. *Transactions of the Cambridge Philosophical Society*, 5:283, 1835.

[GSC$^+$08] Mats G. L. Gustafsson, Lin Shao, Peter M. Carlton, C. J. Rachel Wang, Inna N. Golubovskaya, W. Zacheus Cande, David A. Agard, and John W. Sedat. Three-dimensional resolution doubling in wide-field fluorescence microscopy by structured illumination. *Biophysical Journal*, 94(12):4957–4970, 2008.

[Gus00] M. G. L. Gustafsson. Surpassing the lateral resolution limit by a factor of two using structured illumination microscopy. short communication. *Journal of microscopy*, 198(2):82–87, 2000.

[Ham10] Hamamatsu. Photomultiplier tube r943-02: Gaas (cs) photocathode, wide spectral response: Head-on type for photon counting, low dark counts, excellent p.h.d, 2010.

[Ham19] Hamamatsu Photonics K. Orca-fusion digital cmos camera c14440-20up, 2019.

[Hec99] Eugene Hecht. *Optik*. Oldenbourg, München, 2., durchges. aufl. edition, 1999.

[HM17] Ekbert Hering and Rolf Martin, editors. *Optik für Ingenieure und Naturwissenschaftler: Grundlagen und Anwendungen : mit zahlreichen Bildern, Tabellen, Beispielen*. Fachbuchverlag Leipzig im Carl Hanser Verlag, München, 2017.

[Huf15] Joseph Huff. The airyscan detector from zeiss: confocal imaging with improved signal-to-noise ratio and super-resolution. *Nature methods*, 12:1205 EP –, 2015.

[HvS$^+$08] Mike Heilemann, Sebastian van de Linde, Mark Schüttpelz, Robert Kasper, Britta Seefeldt, Anindita Mukherjee, Philip Tinnefeld, and Markus Sauer. Subdiffraction-resolution fluorescence imaging with conventional fluorescent probes. *Angewandte Chemie (International ed. in English)*, 47(33):6172–6176, 2008.

[HW94] S. W. Hell and J. Wichmann. Breaking the diffraction resolution limit by stimulated emission: stimulated-emission-depletion fluorescence microscopy. *Optics letters*, 19(11):780–782, 1994.

[Jam13] James C. Wyant. Point spread and modulation transfer functions of zernike wavefronts, 2013.

[JFL19] Angélique Jimenez, Karoline Friedl, and Christophe Leterrier. About samples, giving examples: Optimized single molecule localization microscopy. *Methods (San Diego, Calif.)*, 2019.

[JSS$^+$10] Ralf Jungmann, Christian Steinhauer, Max Scheible, Anton Kuzyk, Philip Tinnefeld, and Friedrich C. Simmel. Single-molecule kinetics and super-resolution microscopy by fluorescence imaging of transient binding on dna origami. *Nano letters*, 10(11):4756–4761, 2010.

[JVZ14] Shu Jia, Joshua C. Vaughan, and Xiaowei Zhuang. Isotropic three-dimensional super-resolution imaging with a self-bending point spread function. *Nature Photonics*, 8(4):302–306, 2014.

[KKN11] Erwin Kreyszig, Herbert Kreyszig, and Edward J. Normington. *Advanced engineering mathematics*. John Wiley & Sons Ltd, 10. ed., internat. student vers edition, 2011.

[Kla01] Klaus Weisshart. The basic principle of airyscanning. Technology Note, 2014-07-01.

[Kub13] Ulrich Kubitscheck. *Fluorescence Microscopy: From Principles to Biological Applications*. Wiley-Blackwell, s.l., 1. aufl. edition, 2013.

[Lak06] Joseph R. Lakowicz. *Principles of fluorescence spectroscopy*. Springer, New York, 3rd ed. edition, 2006.

[Lei] Leica. Sp8 lightning: Konfokalmikroskop.

[LLBM11] Matthew D. Lew, Steven F. Lee, Majid Badieirostami, and W. E. Moerner. Corkscrew point spread function for far-field three-dimensional nanoscale localization of pointlike objects. *Optics Letters*, 36(2):202, 2011.

[LM63] W. Lukosz and M. Marchand. Optischen abbildung unter überschreitung der beugungsbedingten auflösungsgrenze. *Optica Acta: International Journal of Optics*, 10(3):241–255, 1963.

[LMH$^+$18] Yiming Li, Markus Mund, Philipp Hoess, Joran Deschamps, Ulf Matti, Bianca Nijmeijer, Vilma Jimenez Sabinina, Jan Ellenberg, Ingmar Schoen, and Jonas Ries. Real-time 3d single-molecule localization using experimental point spread functions. *Nature methods*, 15(5):367–369, 2018.

[LUM$^+$18] Tsung-Li Liu, Srigokul Upadhyayula, Daniel E. Milkie, Ved Singh, Kai Wang, Ian A. Swinburne, Kishore R. Mosaliganti, Zach M. Collins, Tom W. Hiscock, Jamien Shea, Abraham Q. Kohrman, Taylor N. Medwig, Daphne Dambournet, Ryan Forster, Brian Cunniff, Yuan Ruan, Hanako Yashiro, Steffen Scholpp, Elliot M. Meyerowitz, Dirk Hockemeyer, David G. Drubin, Benjamin L. Martin, David Q. Matus, Minoru Koyama, Sean G. Megason, Tom Kirchhausen, and Eric Betzig. Observing the cell in its native state: Imaging subcellular dynamics in multicellular organisms. *Science (New York, N.Y.)*, 360(6386), 2018.

[Mar61] Marvin Minksy. Microscopy apparatus: Ser. no 695107, 1961.

[MCHB$^+$18] Michael J. Mlodzianoski, Paul J. Cheng-Hathaway, Shane M. Bemiller, Tyler J. McCray, Sheng Liu, David A. Miller, Bruce T. Lamb, Gary E. Landreth, and Fang Huang. Active psf shaping and adaptive optics enable volumetric localization microscopy through brain sections. *Nature methods*, 15(8):583–586, 2018.

[MCSF10] Kim I. Mortensen, L. Stirling Churchman, James A. Spudich, and Henrik Flyvbjerg. Optimized localization-analysis for single-molecule tracking and super-resolution microscopy. *Nature methods*, 7(5):377–381, 2010.

[ME10] Claus B. Müller and Jörg Enderlein. Image scanning microscopy. *Physical review letters*, 104(19):198101, 2010.

[MM13] Daniel Malacara and Zacarías Malacara. *Handbook of optical design*. CRC Press, Boca Raton, Fla., third edition edition, 2013.

[MMH15] J. E. McGregor, C. A. Mitchell, and N. A. Hartell. Post-processing strategies in image scanning microscopy. *Methods (San Diego, Calif.)*, 88:28–36, 2015.

[MMS08] Ricardo Marqués, Ferran Martín, and Mario Sorolla. *Metamaterials with negative parameter: Theory, design, and microwave applications*. Wiley series in microwave and optical engineering. Wiley-Interscience, Hoboken, N.J, 2008.

[Nik18] Nikon. N-sim s: Structured illumination super-resolution-mikroscope system, 2018.

[Nik19] Nikon. A1 hd25 / a1r hd25: Confocal microscope system, 2019.

[Nol76] Robert J. Noll. Zernike polynomials and atmospheric turbulence*. *Journal of the Optical Society of America*, 66(3):207, 1976.

[OKB$^+$14] Martin Ovesný, Pavel Křížek, Josef Borkovec, Zdeněk Svindrych, and Guy M. Hagen. Thunderstorm: a comprehensive imagej plug-in for palm and storm data analysis and super-resolution imaging. *Bioinformatics (Oxford, England)*, 30(16):2389–2390, 2014.

[PWH$^+$14] Sven Proppert, Steve Wolter, Thorge Holm, Teresa Klein, Sebastian van de Linde, and Markus Sauer. Cubic b-spline calibration for 3d super-resolution measurements using astigmatic imaging. *Optics Express*, 22(9):10304, 2014.

[Rah11] M. Rahman. *Applications of Fourier Transforms to Generalized Functions*. WIT Press, 2011.

[Ray96] Rayleigh. Xv. on the theory of optical images, with special reference to the microscope. *The London, Edinburgh, and Dublin Philosophical Magazine and Journal of Science*, 42(255):167–195, 1896.

[RBZ06] Michael J. Rust, Mark Bates, and Xiaowei Zhuang. Sub-diffraction-limit imaging by stochastic optical reconstruction microscopy (storm). *Nature methods*, 3(10):793–796, 2006.

[RCL$^+$17] Erik A. Rodriguez, Robert E. Campbell, John Y. Lin, Michael Z. Lin, Atsushi Miyawaki, Amy E. Palmer, Xiaokun Shu, Jin Zhang, and Roger Y. Tsien. The growing and glowing toolbox of fluorescent and photoactive proteins. *Trends in biochemical sciences*, 42(2):111–129, 2017.

[Rei18] Sebastian Reinhard. Super-resolution-correlator, 2018.

[Ros90] Roshdi Rashed. A pioneer in anaclastics: Ibn sahl on burning mirrors and lenses. *Isis*, 81(3):464–491, 1990.

[RSWH13] Stephan Roth, Colin Sheppard, JR, Kai Wicker, and Rainer Heintzmann. Optical photon reassignment microscopy (opra). *Optical Nanoscopy*, 2(1):5, 2013.

[Sei57] Ludwig Seidel. *Ueber die Theorie der Fehler, mit welchen die durch optische Instrumente gesehenen Bilder behaftet sind, und über die mathematischen Bedingungen ihrer Aufhebung*. Cotta, München, 1857.

[SFH$^+$19] Lothar Schermelleh, Alexia Ferrand, Thomas Huser, Christian Eggeling, Markus Sauer, Oliver Biehlmaier, and Gregor P. C. Drummen. Super-resolution microscopy demystified. *Nature Cell Biology*, 21(1):72–84, 2019.

[SGDK07] V. F. Sofieva, A. S. Gurvich, F. Dalaudier, and V. Kan. Reconstruction of internal gravity wave and turbulence parameters in the stratosphere using gomos scintillation measurements. *Journal of Geophysical Research*, 112(D12):8627, 2007.

[SH06] Alexey Sharonov and Robin M. Hochstrasser. Wide-field subdiffraction imaging by accumulated binding of diffusing probes. *Proceedings of the National Academy of Sciences of the United States of America*, 103(50):18911–18916, 2006.

[Sha98] C. E. Shannon. Communication in the presence of noise. *Proceedings of the IEEE*, 86(2):447–457, 1998.

[She88] Colin Sheppard. Super-resolution in confocal imaging. *Optik - International Journal for Light and Electron Optics*, 80:53, 1988.

[SRHA99] J. Small, K. Rottner, P. Hahne, and K. I. Anderson. Visualising the actin cytoskeleton. *Microscopy research and technique*, 47(1):3–17, 1999.

[SSBM14] Yoav Shechtman, Steffen J. Sahl, Adam S. Backer, and W. E. Moerner. Optimal point spread function design for 3d imaging. *Physical review letters*, 113(13):133902, 2014.

[ST12] Oliver Schmidt and David Teis. The escrt machinery. *Current biology : CB*, 22(4):R116–20, 2012.

[ST13] Bahaa E. A. Saleh and Malvin Carl Teich. *Fundamentals of Photonics*. Wiley Series in Pure and Applied Optics. John Wiley & Sons, Chicester, 2nd edition edition, 2013.

[Stu13] S. Stuart. *Physics 1942 - 1962: Including Presentation Speeches and Laureates' Biographies*. Elsevier Science, Burlington, 2013.

[The14a] The Nobel Foundation. The nobel prize in chemistry 2014, 2014.

[The14b] Theresa Klein. Lokalisationsmikroskopie für die visualisierung zellulärer strukturen: Dissertation. *Opus Würzburg*, 2014.

[TLW02] Russell E. Thompson, Daniel R. Larson, and Watt W. Webb. Precise nanometer localization analysis for individual fluorescent probes. *Biophysical Journal*, 82(5):2775–2783, 2002.

[vB71] K. von Bieren. Lens design for optical fourier transform systems. *Applied optics*, 10(12):2739–2742, 1971.

[VCS+18] J. Vangindertael, R. Camacho, W. Sempels, H. Mizuno, P. Dedecker, and K. P. F. Janssen. An introduction to optical super-resolution microscopy for the adventurous biologist. *Methods and applications in fluorescence*, 6(2):022003, 2018.

[vLK+11a] Sebastian van de Linde, Anna Löschberger, Teresa Klein, Meike Heidbreder, Steve Wolter, Mike Heilemann, and Markus Sauer. Direct stochastic optical reconstruction microscopy with standard fluorescent probes. *Nature protocols*, 6(7):991–1009, 2011.

[vLK$^+$11b] Sebastian van de Linde, Anna Löschberger, Teresa Klein, Meike Heidbreder, Steve Wolter, Mike Heilemann, and Markus Sauer. Direct stochastic optical reconstruction microscopy with standard fluorescent probes. *Nature protocols*, 6(7):991–1009, 2011.

[von34] von F. Zernike. Beugungstheorie des schneidenver-fahrens und seiner verbesserten form, der phasenkontrastmethode. *Physica*, 1(7):689–704, 1934.

[vS14] Sebastian van de Linde and Markus Sauer. How to switch a fluorophore: from undesired blinking to controlled photoswitching. *Chemical Society reviews*, 43(4):1076–1087, 2014.

[Wat96] G. N. Watson. *A treatise on the theory of Bessel functions*. Cambridge mathematical library. Cambridge University Press, Cambridge, 2nd ed., cambridge mathematical library ed; repr edition, 1996.

[WB15] Donna R. Whelan and Toby D. M. Bell. Image artifacts in single molecule localization microscopy: why optimization of sample preparation protocols matters. *Scientific reports*, 5:7924 EP –, 2015.

[WLH$^+$12] Steve Wolter, Anna Löschberger, Thorge Holm, Sarah Aufmkolk, Marie-Christine Dabauvalle, Sebastian van de Linde, and Markus Sauer. rapidstorm: accurate, fast open-source software for localization microscopy. *Nature methods*, 9:1040 EP –, 2012.

[WLK$^+$15] Sina Wäldchen, Julian Lehmann, Teresa Klein, Sebastian van de Linde, and Markus Sauer. Light-induced cell damage in live-cell super-resolution microscopy. *Scientific reports*, 5:15348 EP –, 2015.

[WMS$^+$14] Kai Wang, Daniel E. Milkie, Ankur Saxena, Peter Engerer, Thomas Misgeld, Marianne E. Bronner, Jeff Mumm, and Eric Betzig. Rapid adaptive optical recovery of optimal resolution over large volumes. *Nature methods*, 11:625 EP –, 2014.

[Wol13] Emil Wolf. *Progress in Optics*. Progress in Optics. Elsevier Science, Burlington, 2013.

[WS18] Yicong Wu and Hari Shroff. Faster, sharper, and deeper: structured illumination microscopy for biological imaging. *Nature methods*, 15(12):1011–1019, 2018.

[WW12] E. T. Whittaker and G. N. Watson. *A course of modern analysis: An introduction to the general theory of infinite processes and of analytic functions ; with an account of the principal transcendental functions*. Watchmaker Publishing, [Seaside, OR], 2012.

[Zei19a] Zeiss. Lsm 800, 2019.

[Zei19b] Zeiss. Lsm 980: Airyscan 2, 2019.

[Zei19c] Zeiss. Zeiss elyra 7: Lattice sim, 2019.

A Acronyms and Abbreviations

Roman Symbols

λ	wavelength
$\mathscr{F}$	Fourier transform
∇^2	Laplacian operator
ω_x, ω_y	Fourier frequencies
∂	partial differentiation operator
2D	2 dimensional
3D	3 dimensional
*d*STORM	direct stochastical optical reconstruction microscopy
APO	apochromatic correction
AU	Airy unit
BMW	bayerische Motoren Werke
c	speed of light in vaccum
CLSM	confocal laser scanning microscope
COM	communication port
DPL	Diode Pumped Laser
DPSS	diode pumped solid state
EB	end binding

EMCCD	electron multiplying charge coupled device
EPI	greek for *above*
f	focal length
FC-APC	fiber coupling angled physical contact
FOV	field of view
FWHM	full width half maximum
GaAs	gallium arsenide
GFP	Green Fluorescent Protein
GUI	graphical user interface
HILO	higly inclined laminated optical sheet
HP	high power
IR	infrared
ISM	image scanning microscopy
k	wavenumber
LUT	look up table
M	magnification
n	refractive index
ND	neutral density
NIDAQ	National Instrument data acquisition
NIS	Nikon Instrument software
OD	optical density
OPL	optical path length
OPRA	optical photon reassignment
OTF	optical transfer function

PAINT	points accumulation for imaging in nanoscale topography
PALM	photoactivated localization microscopy
PBS	phosphate buffered saline
PFS	perfect focus system
PMT	photo multiplying tube
PSF	Point-Spread-Function
PTFE	polytetrafluorethylen
RCM	rescanning confocal microscope
ROI	region of interest
sCMOS	scientific CMOS
SIM	structured illumination microscopy
SLM	Spatial Light Modulator
SMAP	single molecule analysation platform
SMD	sub miniature docking
SMLM	single molecule localisation microscopy
SQUIRREL	super-resolution quantitative image rating and reporting of error locations
SR	super resolution
STED	stimulated emission depletion
STORM	stochastic optical reconstruction microscopy
TIRF	total internal reflection
TRABI	temporal, radial-aperture-based intensity estimation
YFP	yellow fluorescent protein
ZOLA	zernike optimized localization algorithm

B

Setup

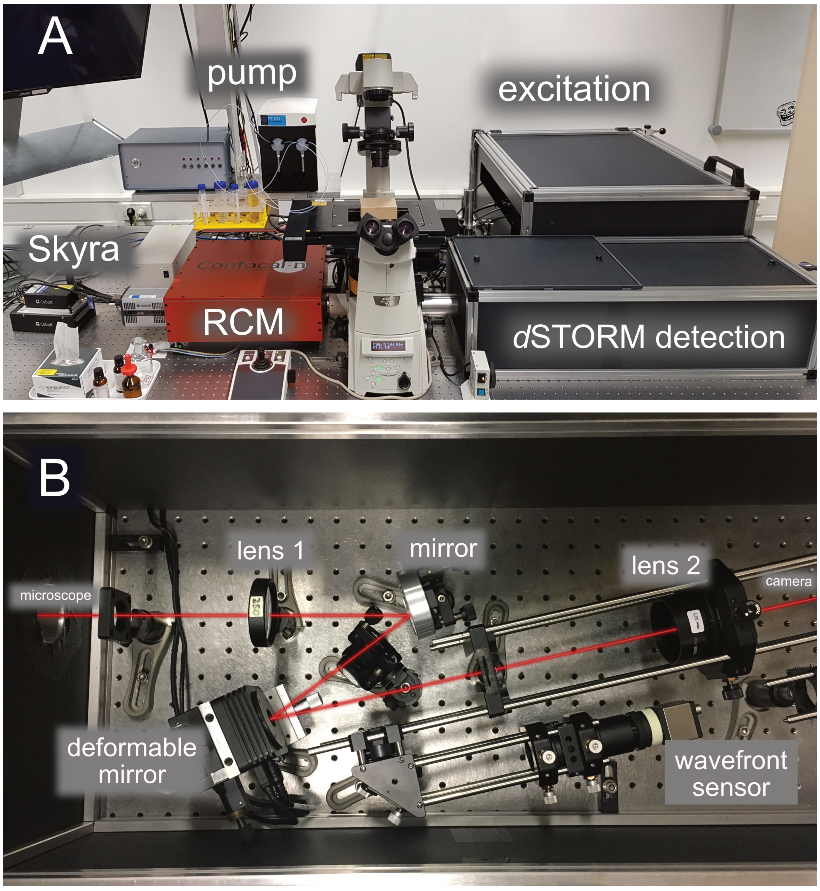

Fig. B.1 **A** Image of the microscope setup with individual components highlighted: RCM unit with laser Skyra, microfluidic pump, excitation laser box for single molecule experiments with *d*STORM detection path containing the deformable mirror. **B** *d*STORM detection path with individual elements: relay system with lens 1 and 2, deformable mirror and wavefront sensor.

C

Affidavit

Eidesstattliche Erklärungen nach §7 Abs. 2 Satz 3, 4, 5 der Promotionsordnung der Fakultät für Biologie

Eidesstattliche Erklärung

Hiermit erkläre ich an Eides statt, die Dissertation: „Korrelative hochauflösende Mikroskopie an lebenden und fixierten Zellen “, eigenständig, d. h. insbesondere selbständig und ohne Hilfe eines kommerziellen Promotionsberaters, angefertigt und keine anderen, als die von mir angegebenen Quellen und Hilfsmittel verwendet zu haben.

Ich erkläre außerdem, dass die Dissertation weder in gleicher noch in ähnlicher Form bereits in einem anderen Prüfungsverfahren vorgelegen hat.

Weiterhin erkläre ich, dass bei allen Abbildungen und Texten bei denen die Verwertungsrechte (Copyright) nicht bei mir liegen, diese von den Rechtsinhabern eingeholt wurden und die Textstellen bzw. Abbildungen entsprechend den rechtlichen Vorgaben gekennzeichnet sind sowie bei Abbbildungen, die dem Internet entnommen wurden, der entsprechende Hypertextlink angegeben wurde.

Affidavit

I hereby declare that my thesis entitled: „Correlative live and fixed cell superresolution microscopy” is the result of my own work. I did not receive any help or support from commercial consultants. All sources and/or materials applied are listed and specified in the thesis.

Furthermore I verify that the thesis has not been submitted as part of another examination process neither in identical nor in similar form.

Besides I declare that if I do not hold the copyright for figures and paragraphs, I obtained it from the rights holder and that paragraphs and figures have been marked according to law or for figures taken from the internet the hyperlink has been added accordingly.

Würzburg, Friday 4th October, 2019

....
Andreas Kurz

D

Publication record

Manuscript 1

Sebastian Doll, Florencio Porto Freitas, Ron Shah, Milene Costa da Silva, Irina Ingold, Andrea Goya Grocin, Elena Panzilius, Christina Scheel, André Mourão, Katalin Buday, Jonas Wanninger, Thibaut Vignane, Vaishnavi Mohana, Markus Rehberg, Aloys Schepers, Valerie O'Donnel, Maceler Aldrovandi, Andreas Kurz, Markus Sauer, Michael Sattler, Edward William Tate, Bettina Proneth, Werner Schmitz, Almut Schulze, Gregorz Popowicz, Derek Pratt, José Pedro Friedmann Angeli, Marcus Conrad (2019). FSP1 is a glutathione-independent ferroptosis suppressor. *Nature*, accepted

Manuscript 2

Gerti Beliu, Andreas J. Kurz, Alexander C. Kuhlemann, Lisa Behringer-Pliess, Mara Meub, Natalia Wolf, Jürgen Seibel, Zhen-Dan Shi, Martin Schnermann, Jonathan B. Grimm, Luke D. Lavis, Sören Doose & Markus Sauer (2019). Bioorthogonal labeling with tetrazine-dyes for super-resolution microscopy. *Communications Biology*, DOI: 10.1038/s42003-019-0518-z

Manuscript 3

Derakhshani, Shaghayegh; Kurz, Andreas; Japtok, Lukasz; Schumacher, Fabian; Pilgram, Lisa; Steinke, Maria; Kleuser, Burkhard; Sauer, Markus; Schneider-Schaulies, Sibylle; Avota, Elita (2109). Measles Virus Infection Fosters Dendritic Cell Motility in a 3D Environment to Enhance Transmission to Target Cells in the Respiratory Epithelium. *Frontiers in immunology*, DOI: 10.3389/fimmu.2019.01294

Manuscript 4

Walter, T.; Schlegel, J.; Burgert, A.; Kurz, A.; Seibel, J.; Sauer, M. (2017). Incorporation studies of clickable ceramides in Jurkat cell plasma membranes. *Chemical communications*. DOI: 10.1039/c7cc01220a

Acknowledgement

This work would certainly not have been possible without the support and assistance of many people, for which I would like to express my gratitude. First of all I would like to thank Markus Sauer for entrusting me with such a project, his enthusiasm, enabling a great scientific freedom in my work and his extremely amicable attitude. I thank you for this opportunity to grow beyond me, to always support me in my own ideas and implementations and your unshakable and inspiring passion for every scientific project in your working group. Furthermore, I would like to thank Roy Gross not only for taking over my second supervisor but also for your interest in my work, your cordial feedback on numerous occasions and the enjoyable conversations. I would like to thank Sören Doose for his always open door, productive and constructive discussions, his support in various analysis questions and his encouraging comments to my ongoing work.

At this point I would also like to thank Sepp (aka Sebastian van de Linde), Rotbart (aka Christian Franke) and the Schwarzer Blitz (aka Thorge Holm). Every doctoral student had a mentor, I was lucky to have three. I owe you much of my knowledge about optics, microscopy and the secrets of localization microscopy.

This work could definitely not have been completed without the support of the mechanics workshop and the electronics/IT department. I would like to thank Albert Gessner and Markus Behringer for their technical support. Albert, your rethinking and adaptation of components has so often made my life in the laboratory easier. Without the contribution of Willi and Oli with electronics and PC many experiment would have failed. As a non-biologist, I have always experienced great sympathy and support in cell culture from Petra Gessner and Lisa Behringer-Plies.

Right at the beginning of my work I came across two Swabians who, despite my Franconian roots, developed an awesome friendship with me. Thank you Gerti and Fabi for the great time we had, be it with ’Kalinka’, in ’Manhattan’, ’Sa Calobra’ or in the laboratory. You allowed time to fly by and connected great memories with it. Thank you for that, it was legendary!

I want to express my gratitude for various contributions and support to Theresa Klein, Sebastian Reinhardt, Felix Wäldchen, Dominic Helmerich, Patrick Eiring, Ralph Götz, Martin Kiesel (Nikon), Eric Manders (confocal.nl) and Dag von Gegerfelt (Cobolt).
The entire working group has always created an incredibly harmonious working atmosphere, for which I would like to thank everyone very much. Be proud of the Sauerlab!
A PhD thesis is accompanied by a lot of bureaucracy, I owe many thanks to our secretary Astrid Thal for constant support in many issues.
My office mates Fabi, Felix, Sina, Franzi and Christian also deserve a special thanks for the always refreshing and entertaining atmosphere.
I would like to thank my family for the everlasting support, my siblings and parents for their patience and love. I could always rely on your encouragement and familial bonds.
Finally, I want to thank you, Sherry, for your patience and love. Your big heart and your humour have always given me the energy to carry on and finish this work. You have probably made the greatest contribution to this work, for which I can hardly thank you.